Multiple Transducer Synthetic Aperture Sonar Interferometry for Emulating SAR Interferometry

Neil Lewitton

A dissertation submitted to the Department of Electrical Engineering,
University of Cape Town, in fulfilment of the requirements
for the degree of Master of Science in Engineering.

Cape Town, January 2007

Declaration

I know the meaning of plagiarism and declare that all the work in the document, save for that which is properly acknowledged, is my own.

Neil Lewitton
Cape Town
January 2007

Abstract

Multiple transducer single-pass synthetic aperture sonar interferometry in air is a technique that can emulate topographic mapping techniques that have not been implemented using radar or that are relatively expensive and difficult to obtain in practice for the radar engineer who wishes to test algorithms using suitable data. This dissertation describes the implementation of a 40 kHz synthetic aperture sonar for acquiring radar-like data. Investigations into beamformed synthetic aperture sonar images as well as multiple-baseline sonar interferograms resulting from imaging a variety of scenes are presented in this thesis. Research that has been completed by previous students is presented as background to the design of the current emulator system. Theory that is common to both radar interferometry and sonar interferometry is discussed. Design parameters are then discussed, followed by a description of the emulator system. Focussed images are combined to form interferograms of different baselines. The coherence was calculated and compared to theoretically predicted values. The result of this dissertation has been to demonstrate that emulation of SAR interferometry is achievable using the designed desktop system as implemented in this dissertation. Further research is now possible using the emulator system to take readings of scaled down phenomena observed in current and future implemented radar systems.

Acknowledgements

I would like to thank my supervisor Dr A.J. Wilkinson for his support and guidance during this dissertation that made final delivery of this dissertation possible.

Sam Ginsberg has been a source of much valuable help during the course of this dissertation and deserves many thanks for making time to help me.

Thanks need to be extended to Glen of the mechanical engineering workshop for help concerned with mounting my sensor platform onto the printer head.

I am grateful to the CSIR and NRF for providing financial support for this dissertation.

Thanks to Zunaid Parker for assisting me with input filter design, to Fayaaz Sataar for helping with deciding on practical matters related to building the motor platform and to Etienne Eccles for explaining signal processing concepts.

I would also like to thank my friend Abbi for always being ready to help me.

My mother deserves many, many thanks for her support during the period of my undertaking this dissertation project.

Contents

List of Figures

List of Tables

List of Symbols

$A()$	Range as a function of cross-range
B	RF bandwidth
B_{TX}	Transmitted Radar Bandwidth
c	Speed of light
D	Dispersion factor
L	Length of chirp pulse
R	Range
R_0	Range corresponding to closest approach or zero Doppler position
RF	Radio frequency
t	Time
v_{RF}	Transmitted signal at RF in time domain
v_{RX}	Received signal in time domain
v_{TX}	Transmitted signal in time domain
V()	Range as a function of cross-range
x	Cross-range position
ζ	System response that is inversely related to the square of radial range to an ideal point target
φ_{RF}	Radio frequency phase
τ	Time length of chirp pulse
Δf	Sweep range of chirp pulse
δR_{3dB}	3dB range resolution

Nomenclature

Cross range—direction perpendicular to range

Doppler frequency—A shift in the radio frequency of the return from a target or other object as a result of the object's radial motion relative to the radar.

Ground range—Slant range projected onto the ground, i.e. range as measured on the ground.

Layover—Effect where multiple points in a scene are mapped to the same point in an image.

Range—The distance from a radar antenna to a target.

Shadowing—Observable effect in region of imaged scene where no returns are possible since the line of sight of that region of the scene is blocked by terrain that does not allow the signal to pass through.

Slant range—Range as measured along the line of sight of the imaging radar

Spectral shift—Displacement (in Hz) between the Fourier spectral components of range profiles acquired from different incidence angles.

Synthetic Aperture Radar (SAR)—Coherent radar imaging technique that involves synthesising an aperture in order to obtain fine cross-range resolution

Swath—The area on the surface that is illuminated by a radar antenna.

Chapter 1

Introduction

1.1 Statement of Problem

Synthetic aperture radar (SAR) images are produced using a signal processing technique that uses data recorded by a radar transmitter and receiver pair. The transmitter and receiver move past a scene on the ground that reflects a transmitted radar signal back to the receiver antenna through the air. SAR interferometry involves using multiple SAR images that are obtained either by using multiple simultaneous recording receivers and only one transmitter (single pass) or by taking multiple SAR images of the scene repeatedly using the same transmitter/receiver antenna pair after a time gap (repeat-pass). The purpose of this dissertation is to produce suitable images using a 40 kHz air sonar system that can emulate characteristics of SAR images that are used in SAR interferometry.

1.2 Emulation of SAR Interferometry using sonar

Dr A.J. Wilkinson has supervised emulation of radar using sonar by undergraduates [24, 20]. Further work was done by emulating inverse synthetic aperture sonar (ISAS) [18] by the author of this dissertation by dragging reflective targets past a transmitter/receiver sonar transducer pair that had been used in [24, 20]. Inverse synthetic aperture sonar (ISAS) was further investigated in a paper [7] co-authored by the author of this dissertation. Software was subsequently written by the author of this dissertation together with P. Menting to form repeat-pass ISAS interferograms.

Single-pass SAR interferometry emulation using sonar requires simultaneous recording of sonar returns on multiple antennas. This is achievable by building a sonar system that can simultaneously transmit a signal as well as simultaneously record echoes on multiple receiver channels. Echoes can then be stored after sampling by a data acquisition card. Signal processing can then be performed on these echoes to form focussed ISAS images and air sonar interferograms.

1.3 Objectives

The objectives of this thesis are to achieve the following:

- Design a laboratory scale acoustic radar emulation system that is capable of moving transducers along a specified track while simultaneously recording echoes

- To investigate the properties of the radar emulation system
- Perform signal processing on the data and to form Synthetic Aperture Sonar (SAS) images and interferograms
- To take readings of scenes that demonstrate specific features of radar interferometry using emulation by sonar
- Draw conclusions and to make recommendations regarding the suitability of the system for its intended purpose

1.4 Plan of Development

Chapter 1 is the chapter that introduces the work done in this dissertation.

Chapter 2 discusses existing SAR interferometry configurations that have been implemented. Literature that describes the implementations of these systems is reviewed. Aspects of these designs that are relevant to emulation of radar in air using sonar are then examined. The SAR image formation process is then described, followed by an overview of SAR interferometry.

Chapter 3 looks at the hardware aspect of the project. Input, output and other design issues involved in reading data that are to be used for signal processing are considered.

Chapter 4 describes fixed-length array beamforming, followed by a description of the back-projection image processing algorithm implemented for processing the air sonar images. The limitations of emulating SAR back-projection processing using a fixed-length array beamforming technique is discussed.

Chapter 5 presents readings taken using the emulator.

Chapter 6 describes conclusions and makes recommendations for further research.

Chapter 2

Sonar-Specific Considerations for Emulating SAR Interferometry

This chapter presents theory related to implementing a functional SAR interferometry system. Information related to the background and theory of the SAR imaging process is followed by a discussion of SAR interferometry. The first aim is to describe the kind of data that is required for emulating SAR interferometry. The preliminary section that describes the theory behind SAR interferometry is presented as an introduction to the design of the SAR interferometry emulator, and is meant to present well-established facts from previous works.

Design parameters are then identified that illustrate how the SAR interferometry technique can be implemented using a laboratory scale sonar emulator. Calculations with corresponding graphs are presented. This is followed by a comparison between SAR interferometry and the beamforming interferometric technique that is proposed for the emulator.

2.1 Background to SAR

Synthetic aperture radar (SAR) is a radar imaging technique that has seen many applications in fields as diverse as modern military surveillance, terrain mapping and the monitoring of climate change. The benefit of SAR image formation comes from the fact that almost independent of distance from the scene that is being imaged, it is possible to use image processing techniques to synthesise a sufficiently large aperture that produces images with fine cross range resolution [10].

2.1.1 Overview of implemented SAR Systems

The method of taking data in SAR imaging involves flying a radar antenna transmitter/receiver pair over a scene in parallel tracks. Measurements of the phase and magnitude of a reflected signal are recorded after transmission of a radar pulse to the imaged scene. Measurements are normally taken using spaceborne antennas or antennas that are carried by a plane that flies over a scene. Factors under consideration when deciding whether to use an aircraft or a spaceborne satellite can be summarised as follows [12]

- Dimensions of area that is to be imaged
- Time needed to observe the scene to satisfaction of requirements

- Performance parameters of available equipment used for imaging
- Details pertaining to how soon results are obtained and expenses incurred in the process

Figure 2.1 shows a simplified representation of a typical SAR imaging geometry. A transmitter/receiver antenna pair is flown over a scene and successively transmits a signal that is reflected back to the receiving antenna for recording. SAR uses coherent radar, which means that both the magnitude of the received signal as well as its phase relative to the transmitted signal are recorded. It is the storage of the phase-history of a point target that allows the SAR focussing algorithm to compress a typical point target response in cross range. This is achieved by performing a cross-correlation of the received signal in the cross range direction with a template of the received response from a point target.

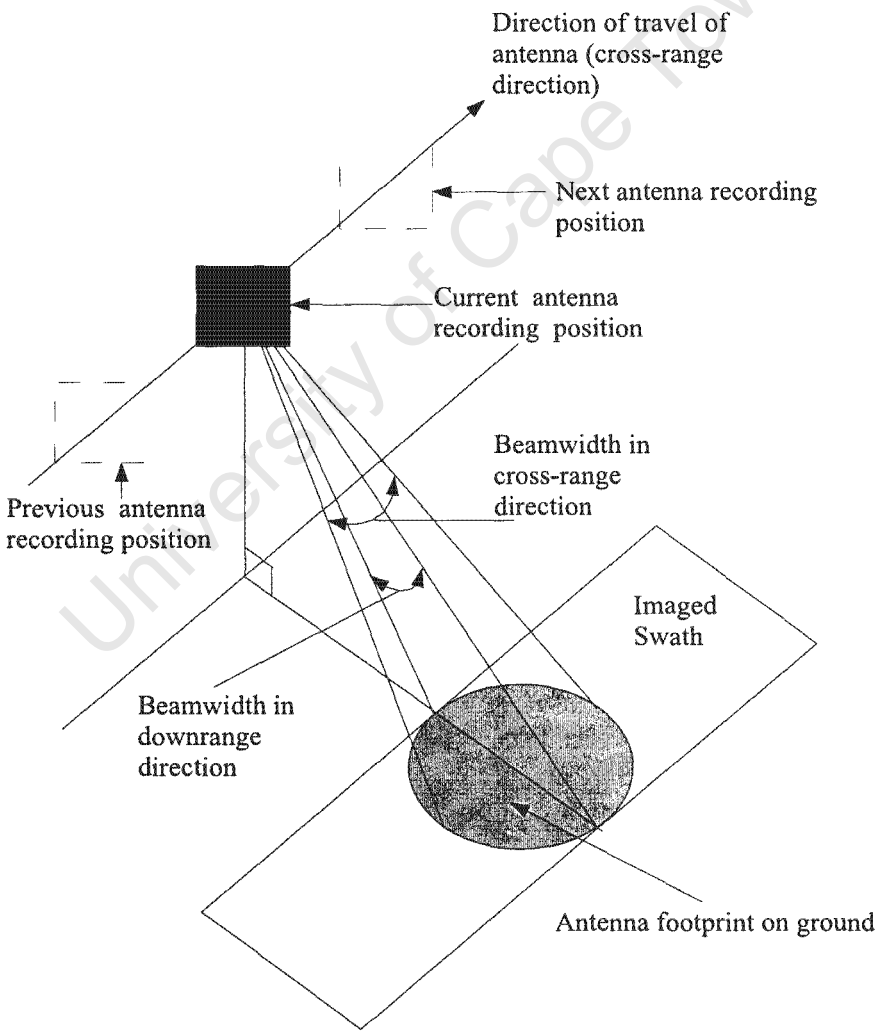

Figure 2.1: Illustration of SAR Imaging Geometry

Table 2.1 compares system parameters for existing SAR Systems as provided by [10]. As seen in Table 2.1, both dimensions of azimuth and elevation of the DRA Airborne SAR antenna are smaller than that of the ERS-1 antenna. The operating altitude of the Airborne SAR system is also significantly lower.

	ERS-1	DRA Airborne SAR
Wavelength (λ)	5.67 cm (C-band)	3.1cm (X-band)
Polarization	VV	HH
Bandwidth (B)	15.5 Mhz	100 Mhz
Transmitted pulsewidth (τ_p)	37.1 μs	5 μs
PRF	1680 Hz	adjustable - 1.1 kHz
Antennna size (azimuth $\times$ elevation)	10m $\times$ 1m	1.8m $\times$ 0.18m
Altitude	785 km	$<$ 14 km

Table 2.1: System Parameters for Satellite and Airborne SAR Systems [10]

2.1.2 Existing SAR Image Formation Technology

SAR images are produced using signal processing techniques that take into account both the magnitude and the phase history of the returned signals from each position along the flight track of the antenna. Early systems used optical processing for focussing raw data into SAR images. This technique optically correlates raw SAR data onto film to produce a focussed image, and according to [12] has advantages. Software (digital) processing techniques that produce SAR images from raw data have largely replaced these earlier implementations.

2.2 SAR design considerations applicable to emulation

The extended radar system model and subsequent theory that are described in this section are based on the description provided in [5].

2.2.1 Introduction to classical time-domain SAR Image Formation

The closest-approach position of the point target as the antenna flies by is known as the zero-Doppler position of the point target R_0. The goal of a typical classical time-domain SAR algorithm would be to focus a point target as a point on a two dimensional grid in its zero-Doppler/slant range position.

Time domain SAR image processing involves considering each pixel in the final image that is to be calculated one at a time. Each sample in each of the range-compressed down-range profiles that corresponds to this pixel is time-compensated and weighted by multiplying by a range-dependent factor. All time-compensated pixels are then added together to produce the value of the pixel under consideration. The time domain SAR focussing algorithm uses a sliding aperture in which aperture length is range dependent.

2.2.2 Extended Radar System Model

The extended radar system model describes signals in terms of time t. Consider the case of a signal $v_{TX}(t)$ with bandwidth B_{TX} that is transmitted to a point target at distance R

from a transceiver. If the receiving antenna has sufficient bandwidth greater than B_{TX}, the received signal $V_{RX}(t)$ will be recorded as a delayed, scaled version of $V_{TX}(t)$. This is represented by the formula

$$V_{RX}(t) = \zeta_1 V_{TX}(t-\tau) \tag{2.1}$$

where $\tau = \frac{2R}{c}$ is the time delay and ζ_1 is a constant factor that is directly proportional to $\frac{1}{R^2}$.

This linear radar system model can be extended to include the case of N point targets at ranges R_i that produce responses that add linearly in the model to form the time-dependent received signal

$$V_{RX}(t) = \sum_{i=1}^{N} \zeta_i v_{TX}(t-\tau_i) \tag{2.2}$$

$V_{RX}(t)$ can be further extended to include the case of a distributed target or scene where it is the result of the impulse response of the scene $\zeta(t)$ convolved with the transmitted signal $v_{TX}(t)$. This is described in the equation

$$v_{RX}(t) = \int_{-\infty}^{\infty} \zeta(\tau) v_{TX}(t-\tau) d\tau \tag{2.3}$$

The scene impulse response $\zeta(\tau)$ has infinite bandwidth. It is therefore a real-world limitation that only a section of $\zeta(\tau)$ can be recorded. In the frequency domain, $\zeta(f)$ is multiplied with the band-limited approximately rectangular signal $V_{RX}(f)$ as illustrated in Figure 2.2.

2.2.3 Choice of Signal for Transmission

The signal analysis as applicable to this dissertation takes into consideration the mainstream approach to measuring coherent down-range profiles as being reflections of transmitted chirp pulses. According to [13], a chirp pulse has experienced almost universal application in remote-sensing SAR.

A chirp pulse is a pulse that has instantaneous frequency that is linearly swept across a range of frequencies that are set by the designer. The description of the transmission and reception of a chirp pulse in this section follows the nomenclature and methodology of [5].

The real RF signal representation of a chirp signal centred on frequency f_0 is

$$v_{RF}(t) = rect\left(\frac{t}{T}\right)\cos\left(2\pi\left[f_0 t + \frac{1}{2}Kt^2\right]\right) \tag{2.4}$$

where T is pulse length in seconds and K is sweep rate in Hz/s.

The analytic representation of the chirp signal using complex phasor notation is

$$v_{TX}(t) = rect\left(\frac{t}{T}\right) e^{j2\pi[f_0 t + \frac{1}{2}Kt^2]} \tag{2.5}$$

The RF phase of the chirp signal is then

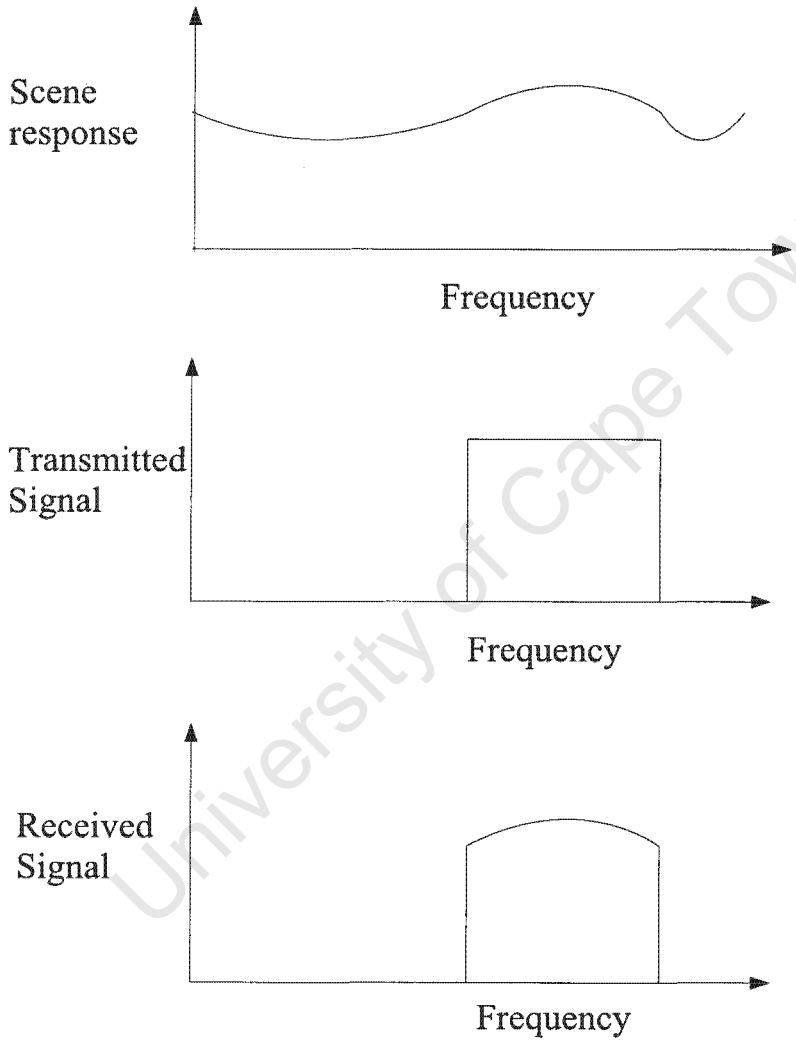

Figure 2.2: Frequency domain version of extended target model

$$\varphi_{RF} = 2\pi\left(f_0 + \frac{1}{2}Kt^2\right)\,[rad] \tag{2.6}$$

The RF instantaneous frequency is

$$\begin{aligned} f_{RF}(t) &= \frac{1}{2\pi}\frac{\varphi_{RF}(t)}{dt} \\ &= f_0 + Kt\,[Hz] \end{aligned} \tag{2.7}$$

Note that the function $f_{RF}(t)$ is linear and therefore represents the range of frequencies over which the chirp pulse is swept.

Basebanding of the analytic chirp signal $v_{TX}(t)$ involves multiplication with complex phasor $e^{-j2\pi f_0 t}$ in the time domain, resulting in a basebanded version of the chirp pulse:

$$v_{bb}(t) = rect\left(\frac{t}{T}\right)e^{j2\pi\frac{1}{2}Kt^2} \tag{2.8}$$

The benefit of using a chirp pulse is that a chirp pulse can be made arbitrarily long independent of the desired bandwidth. The energy in a pulse increases in direct proportion to the length of the pulse. According to matched filter theory, a high signal to noise ratio is obtained at the output of a matched filter when an input signal has high energy. It is therefore a desirable feature of a chirp pulse that the energy in a chirp can be set by creating a chirp pulse of a desired length.

A number of parameters can be used for determining the choice of the transmission signal. Pulse length is limited by the distance to the scene under observation. The maximum pulse length is

$$T_{max} = \frac{2R_{min}}{c}\,[m] \tag{2.9}$$

where R_{min} is the distance to the closest edge of the scene and c represents the speed of light in air in m/s.

As a result of the length of the chirp pulse, a deadband region exists in slant range where point targets are typically not received because of receivers being swamped by the output signal of the transmitter and therefore being unable to receive faint returns from near point targets. The calculation for determining the closest range of a measurable point target is

$$Closest\,range = \frac{cT}{2}\,[m] \tag{2.10}$$

where c represents the speed of light in air in m/s and T represents the time length of the pulse in seconds.

A chirp waveform is characterised by a time-bandwidth product D that is defined by the equation

$$D = \Delta f T = KT^2 \tag{2.11}$$

where Δf is known as the sweep range and represents the range of frequencies over which the chirp pulse is swept.
For D >50, the magnitude spectrum of the matched filter response is approximately rectangular and has a 3 dB bandwidth of approximately Δf.

2.2.4 Range Sampling and Compression

A compressed point target response can be seen in Figure 2.3 where the matched filter output has a $\left|\frac{\sin(x)}{x}\right|$ shape in the time domain. This shape corresponds to a rectangular shape in the frequency domain. Range compression using a matched filter compresses the reflected chirp signal to a 3 dB range resolution of

$$\delta R_{3dB} = \frac{c}{2B} \tag{2.12}$$

where δR_{3dB} is the 3dB resolution in the downrange direction, c represents the speed of light in air, and B represents the bandwidth (i.e. the frequency sweep) of the chirp pulse that is transmitted. The high sidelobes need to be reduced after range compression. Applying a Hanning Window in the frequency domain of the range-compressed signal will result in side-lobes of the signal being reduced in the time domain.

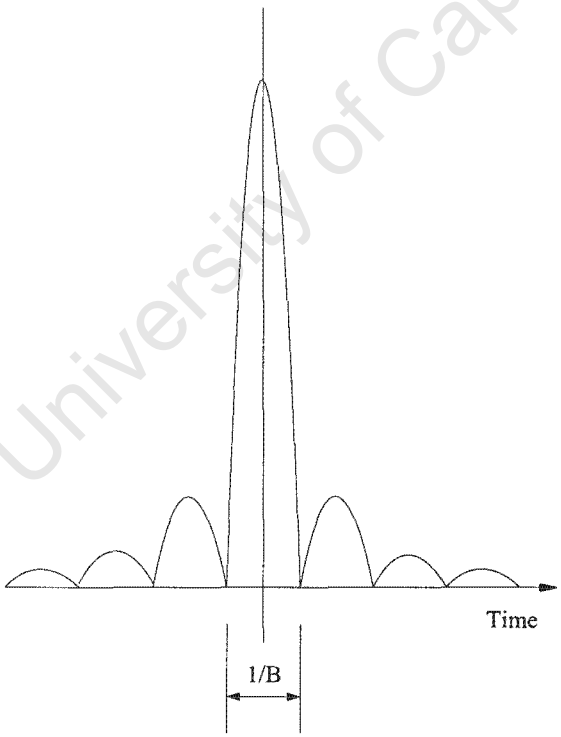

Figure 2.3: Illustration of Compressed Point Target Response

2.2.5 Cross-range compression

Figure 2.4(a) shows the distance of a point target to the antenna as the antenna moves past the point target in a straight line. Positions of the antenna are included from the time position before, during and after the time position at which the point target is closest to the

antenna. This cross range position has the shortest time delay of return of the transmitted pulse.

Figure 2.4(b) shows a plot that clearly demonstrates the hyperbolic nature of the range R(x) from a point target to the antenna as the antenna moves past the point target.

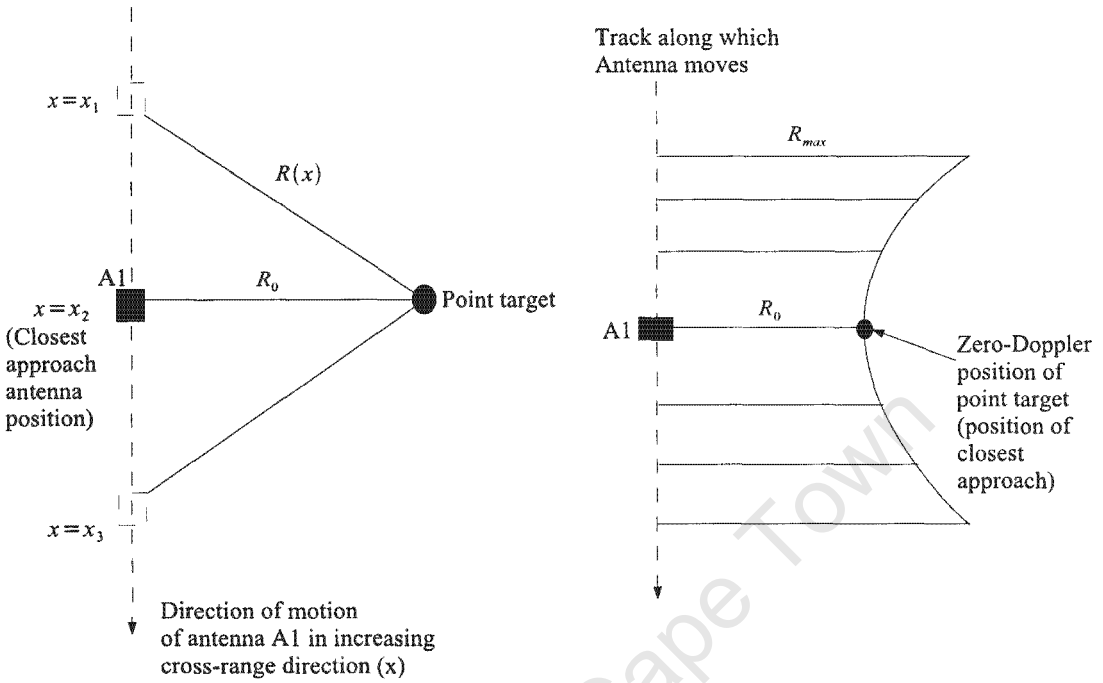

(a) Illustration of distance to point target R(x) as a function of position in cross-range direction at different values of cross-range x

(b) Hyperbolic function of range R(x) to point target (measured relative to an antenna that moves past the point target along a straight line track in cross-range x). The zero-Doppler position of the point target is clearly indicated

Figure 2.4: Diagrams illustrating range as a function of cross range position

The closest-approach position of the point target as the antenna flies by is known as the zero-Doppler position of the point target and has range R_0. The goal of a typical classical time-domain SAR image would be to focus a point target as a point on a two dimensional grid in its zero-Doppler/slant range position.

Consider the case of an unfocussed SAR image that contains a history of coherent responses of a stationary point target received by a transceiver that moves past the point target. In this case, the phase-history of the point target response when considered in the cross range direction approximates a chirp pulse.

The longer the synthetic aperture that is synthesised, the higher the instantaneous frequencies at the edges of the synthesised beam while the point target is still illuminated by the beam. The sampling in azimuth according to the Nyquist theorem needs to be twice the highest frequency, which in this case would occur at an edge of the synthetic aperture.

The wavelength λ of a transmitted signal is related to the frequency f_0 at which it is transmitted and its speed c in air by

$$\lambda = \frac{c}{f_0} \tag{2.13}$$

Figure 2.4 illustrates range as a function of cross range. The received signal can be approximated as follows [5]:

$$\begin{aligned} V(x) &= A(x)e^{-j4\pi R/\lambda} \\ &= A(x)e^{j\psi(x)} \end{aligned} \tag{2.14}$$

where $V(x)$ is the received signal, $A(x)$ is the amplitude of the received signal, and $\psi(x)$ is the two-way range-dependent phase as a function of cross range x. Since the phase as a function of cross range of the returning pulse is dependent on an approximately parabolic range function [5], the point target response curve in the cross range section is an approximate chirp waveform.

Cross-range compression can take place by matched filtering and produces a 3dB resolution of

$$\delta x \approx \frac{0.89}{B_x} \tag{2.15}$$

The cross range bandwidth of the point target response history curve with wavelength λ is

$$B_x = \frac{4\sin(\theta/2)}{\lambda} \tag{2.16}$$

provided that the synthesised aperture is symmetrical with respect to the range line joining the middle of the synthesised aperture to the point target that is to be imaged.

The length of a synthetic aperture in cross range direction is limited by the distance in cross range that the transceiver can move past a point target while simultaneously illuminating the target.

2.2.6 Limitations of Synthetic Aperture Image Formation

Layover

Since sonar images are measured in slant range, a situation can occur where two points occupying different points on the ground and that have different heights can occupy identical slant ranges. This phenomenon is known as layover and results in a mapping of multiple points in the downrange profile into the same slant range bin. Layover is illustrated in Figure 2.5 where points A and B will map to the same position in slant range since both points share a common range arc from the imaging antenna.

Shadowing

Shadowing occurs when an obstacle is found between the imaging radar and the target, resulting in information from the obstructed target section being absent from the scene profile. Region BCD in Figure 2.5 is an example of a region in a scene that experiences shadowing.

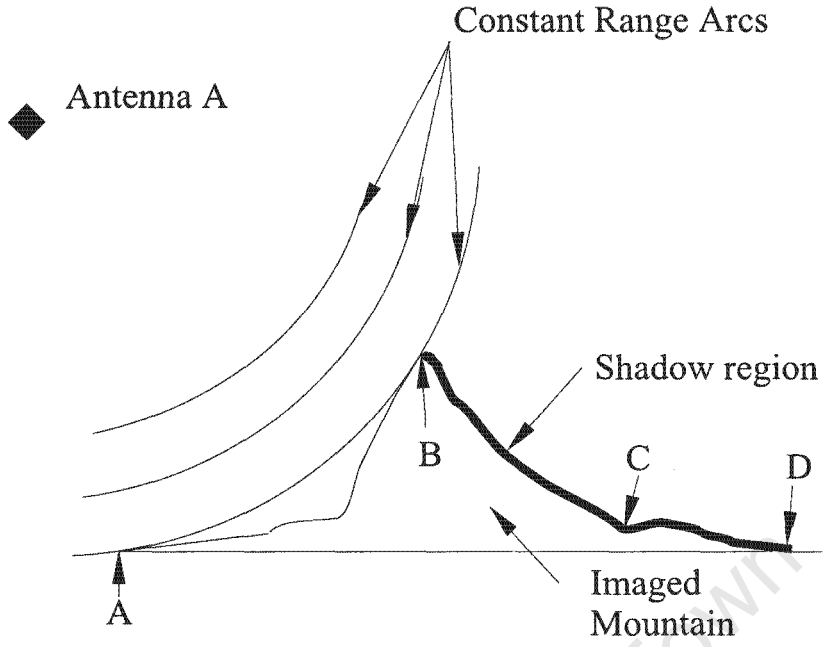

Figure 2.5: Illustration of Layover and Shadowing

2.3 SAR Interferometric Processing

2.3.1 Background to SAR Interferometry

Interferometric processing typically pays attention to the difference in phase of the returned signals from the multiple SAR images produced after focussing multiple raw SAR images obtained from an imaged scene [10, 4, 8].

SAR interferometry is typically operated in one of two modes: single-pass or repeat-pass configuration. Single-pass SAR interferometry simultaneously takes all recordings that will later be processed. In contrast, repeat-pass SAR interferometry configurations take readings from the imaged scene multiple times separated by a period of time [4, 8, 19].

Focussed SAR images that have simultaneously been taken from different vantage points in single-pass configuration can be used to produce a height map of the area on the ground that is common to all the images. Signal processing algorithms can be used to determine the common area of the SAR images where different reflection characteristics as seen from different vantage points from the scene can be utilized to provide more information about the scene than would be possible with only one recorded SAR image [4, 8].

Differential interferometry involves taking more than one pass over a scene and producing an image that displays a measure of the difference between the images after a period of time has passed. An example of a real-world application for this form of interferometry includes measuring shifts in the earth's surface as a result of earthquakes.

2.3.2 SAR Interferometry Geometry

Consider a dual antenna SAR Interferometry system as in Figure 2.6 with two transceivers, TxRx1 and TxRx2, a distance b apart. The distance b between the two antennas

is known as the interferometric baseline. With this geometry the time delay for the echo of a transmitted pulse to return to TxRx1 is t_{d1} and for TxRx2 it is t_{d2} as described in the following formulae

$$t_{d1} = \frac{2r_1}{c} \tag{2.17}$$

$$t_{d2} = \frac{2r_2}{c} \tag{2.18}$$

where r_1 and r_2 represent the slant ranges from TxRx1 to a point target P and from TxRx2 to a point target P respectively, and c is the speed of sound.

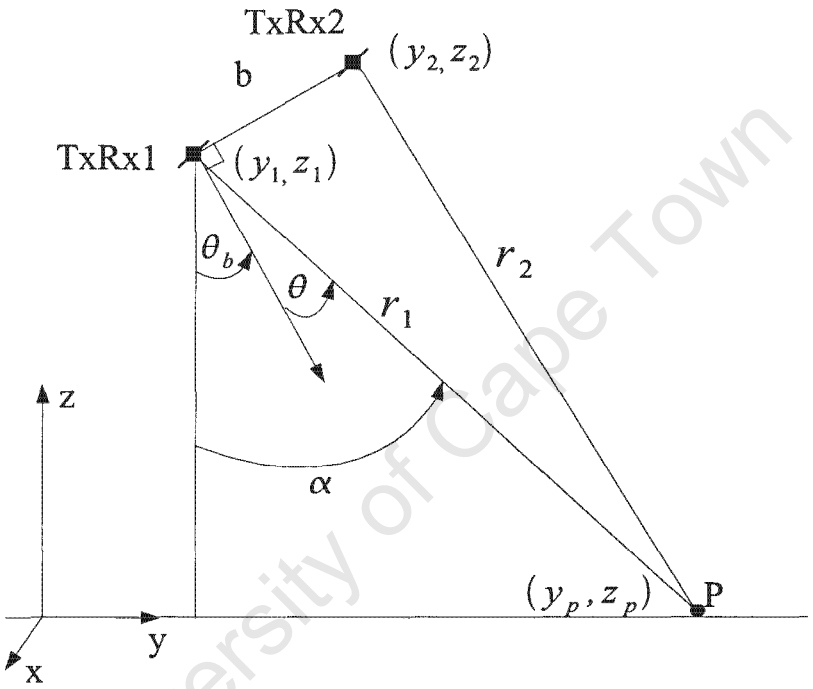

Figure 2.6: Side-view illustration of a multiple antenna interferometric SAR geometry

In [4] the interferometric phase φ of a dual pass system is then derived as

$$\begin{aligned} \varphi &= 2\pi f_0(t_{d2} - t_{d1}) \\ &= \frac{4\pi}{\lambda}(r_2 - r_1) \end{aligned} \tag{2.19}$$

A general equation for the interferometric phase φ_{12} is given by

$$\varphi_{12} = \frac{2\pi Q(r_2 - r_1)}{\lambda} \tag{2.20}$$

where Q is a constant defined as Q=1 for the case of a single pass dual antenna system, while Q=2 for the case of a dual pass system.

The interferometric phase that is measured is a modulo 2π measurement that is limited to the range $(-\pi, \pi]$ of the absolute phase φ_{12}, i.e. $\psi_{12} = arg\{e^{j\varphi_{12}}\}$ where

$$\varphi_{12} = \psi_{12} + k.2\pi \tag{2.21}$$

for k an integer. This means in effect that wrapped phase ψ_{12} needs to be unwrapped by adding the proper multiple of 2π to it in order to determine the absolute phase φ_{12}. Height reconstruction techniques use the unwrapped interferometric phase to form height maps. The absolute interferometric phase φ_{12} for a single-pass where Q=1 can be calculated as follows:

$$\varphi_{12} = \frac{2\pi}{\lambda}\left(\left[b^2 + r_1^2 - 2r_1 b\sin(\theta)\right]^{\frac{1}{2}} - r_1\right) \tag{2.22}$$

Rearranging terms allows the angle of arrival to be made the subject of this formula:

$$\theta = \arcsin\left(\frac{-\lambda\varphi_{12}}{2\pi b} + \frac{b}{2r_1} - \frac{\lambda^2\varphi_{12}^2}{8\pi^2 b r_1}\right) \tag{2.23}$$

Finally, the angle of arrival parameter θ and the angle of the baseline from the vertical θ_b can be used to reconstruct the position of a point in cartesian co-ordinates according to the following equations:

$$y_p = y_1 + r_1\sin\left(\theta + \theta_b\right) \tag{2.24}$$

$$z_p = z_1 - r_1\cos\left(\theta + \theta_b\right) \tag{2.25}$$

2.3.3 Ambiguity Analysis

The wrapped interferometric phase needs an unknown constant integer multiple of 2π added to it before the absolute phase is determined. It should be noted that there are multiple values of unwrapped phase that could have identical wrapped phase values. If the two-dimensional case in Figure 2.7 is considered, the spacing along an arc of identical ranges has angular ambiguities that are offset from the true direction of arrival by an integer multiple of $\Delta\theta_{amb}$. This ambiguity can be calculated as follows [4, 8]:

$$\Delta\theta_{amb} = \left|\frac{d\theta}{d\varphi_{12}}\right|\Delta\varphi_{12} = \left|\frac{d\theta}{d\varphi_{12}}\right|2\pi \tag{2.26}$$

$$\Delta\theta_{amb} = \left|\frac{\lambda[b^2 + r_1^2 - 2r_1 b\sin(\theta)]^{\frac{1}{2}}}{r_1 b\cos(\theta)}\right| \tag{2.27}$$

Using far field approximation where $r_1 >> b$ leads to the equation:

$$\Delta\theta_{amb} \approx \left|\frac{\lambda}{b\cos(\theta)}\right| \tag{2.28}$$

The height error Δh_{amb} as illustrated in Figure 2.7 can be calculated as

$$\Delta h_{amb} = \left|\frac{dh}{d\theta}\right|\Delta\theta_{amb} \tag{2.29}$$

which simplifies to

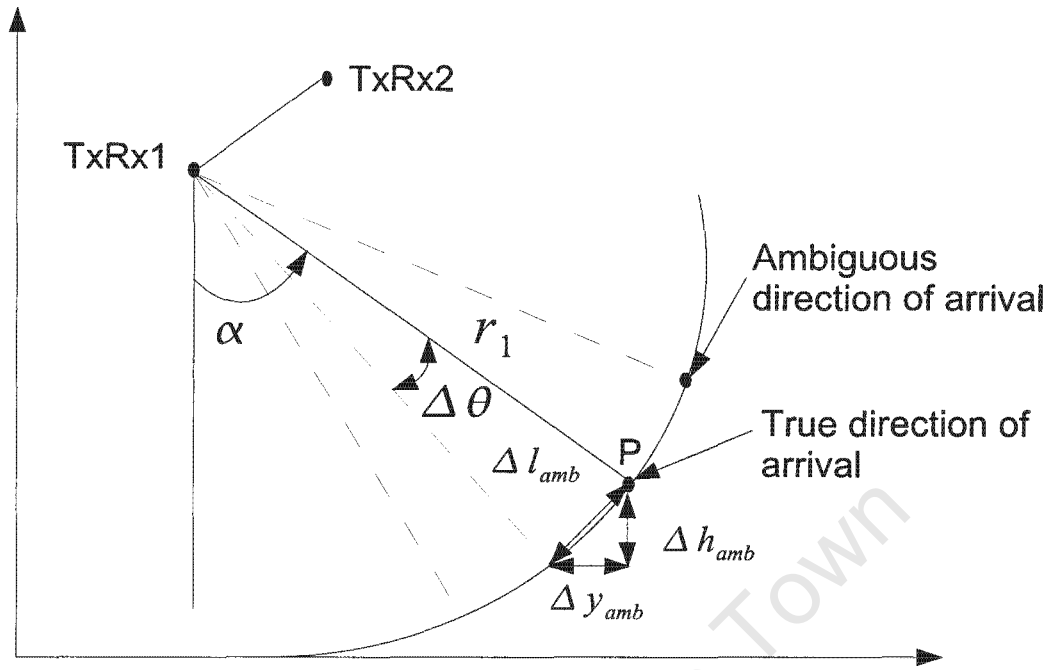

Figure 2.7: Ambiguous direction of arrival

$$\Delta h_{amb} = \Delta\theta_{amb}.r_1 \sin(\alpha) \tag{2.30}$$

The displacement ambiguity Δl_{amb} and horizontal ambiguity Δy_{amb} as shown in Figure 2.7 is

$$\Delta l_{amb} = \Delta\theta_{amb}.r_1 \tag{2.31}$$

$$\Delta y_{amb} = \Delta\theta_{amb}.r_1 cos(\alpha) \tag{2.32}$$

2.3.4 Speckle

The speckle effect is a property of a distributed scatterer scene that displays random signal return characteristics. According to [10] this random signal return is as random as Gaussian noise. However, for the purposes of single-pass interferometry, which consists of using two or more receivers that receive echoes from a target, the multiple scenes have a correlation that is affected by baseline size.

2.3.5 Coherence

The coherence description that follows takes into account factors described in [8]. The complex coherence γ of two complex signals V_1 and V_2 can be defined as [22]:

$$\gamma = \frac{E\{V_1.V_2^*\}}{\sqrt{E\{|V_1|^2\}}\sqrt{E\{|V_2|^2\}}}$$

where $E\{x\}$ is the expected value of x. The coherence magnitude $|\gamma|$ is called the degree of coherence and is affected by the following 3 factors:

- temporal coherence,
- geometric coherence and
- receiver noise coherence.

The relationship can be modelled as shown in the following formula [14, 4, 8] involving three components:

$$|\gamma| = |\gamma_{time}| \cdot |\gamma_{geometry}| \cdot |\gamma_{snr}| \tag{2.33}$$

where γ represents coherence, γ_{time} represents temporal coherence, $\gamma_{geometry}$ represents geometric coherence and γ_{snr} represents receiver noise coherence.

Temporal coherence

Repeat-pass SAR interferometry involves measuring differences between SAR images of a common surface taken at different times. During the time that elapses between passes, it is possible for changes to occur to the imaged scene. Examples of possible changes include a change in density of vegetation on the imaged scene's surface, and a change in atmospheric conditions that would affect propagation of radar signals. The surface change causes decorrelation.

The effect of these changes can be modelled by introducing a temporal decorrelation factor γ_{time}.

Geometric coherence

Decorrelation that is a result of different viewing angles results in an observable spectral shift in returned signals [11, 8]. This shift is directly proportional to the baseline distance between antennas receiving the returned signal. The decorrelation effect due to baseline can be measured by a geometric coherence indicator that is calculated as follows:

$$\gamma_{geometry} = \frac{BW - |\Delta f_{range}|}{BW} \tag{2.34}$$

where BW is the radar pulse bandwidth and Δf_{range} is a spectral shift in the range direction that lies within the limits $-BW \leq \Delta f_{range} \leq BW$.

The geometry under investigation in this dissertation involves a common transmitter and multiple receiving antennas. The following formula [8] can be used for modelling spectral shift in the case of one transmitting antenna and two receiving antennas:

$$\delta f_{range} = f_0 \left[1 - \left(\frac{\sin(\theta_{t1}) + \sin(\theta_{r1})}{\sin(\theta_{t1}) + \sin(\theta_{r2})} \right) \right] \tag{2.35}$$

where the angles are defined in Figure 2.8. Spectral shift is represented by δf_{range}, f_0 is the radar operating frequency and θ is the incidence angle relative to the surface normal of a point on a sloping surface.

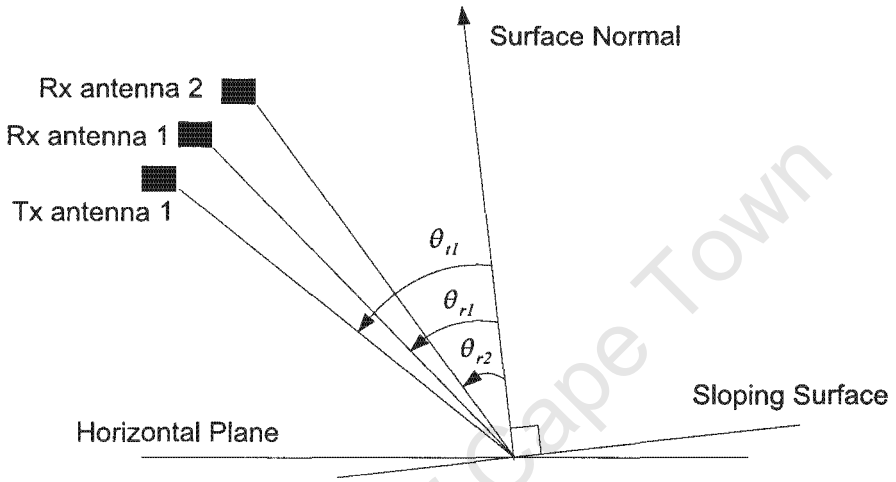

Figure 2.8: Geometry used to describe spectral shift in terms of incidence angles

Receiver noise coherence

Receiver noise reduces the coherence between images, and is modelled by the factor [15, 8]

$$\gamma_{snr} = \frac{1}{\sqrt{1 + \frac{1}{SNR_1}}} \cdot \frac{1}{\sqrt{1 + \frac{1}{SNR_2}}} \tag{2.36}$$

where SNR_1 and SNR_2 represent the signal to noise ratios of the two SAR images.

2.4 Sonar-specific design considerations

In practice, the main differences between sonar signal processing, as discussed in this dissertation, and radar signal processing, are

- the size of the imaged scene, and
- the propagation properties of the transmitted signal.

The speed of sound in dry air is calculated according to the formula [1]

$$v_{sound\,in\,air} \approx 331.4 + 0.6T_C\, m/s \tag{2.37}$$

where T_C is the temperature of the air in degrees Celsius.
The following points summarise the differences between SAR interferometry and SAS interferometry

- **Speed in air:** Radar signals travel in air at approximately $3 \times 10^8\, m.s^{-1}$, the speed of light in air, while sonar signals typically travel at the speed of sound in air, at approximately $340.5\, m.s^{-1}$ in dry air at $15°C$.
- **Air Propagation range of operation:** Radar typically outperforms sonar in its ability to operate over much larger distances in air with less attentuation than a sonar system experiences.
- **Polarization:** Radar signals are electromagnetic waves that are polarized, whereas sonar waves are non-polarized.
- **Hardware costs:** Satellite or airplane radar systems are expensive to implement and operate, whereas a small laboratory scale sonar system is built using cheap components and requires little maintenance.
- **Sampling rates:** Radar systems typically use much higher sampling rates than sonar systems. This means that more sophisticated equipment with higher specification are required for radar systems.
- **Wavelength:** A radar signal's wavelength is typically larger than that of a sonar system in air. Typical values of radar wavelengths for a radar system as seen from Table 2.1 would be for example 5.67 cm for ERS-1 and 3.1 cm for DRA airborne SAR. This is larger than a typical sonar wavelength of for example 8.5 mm for a chirp signal centred on a 40 kHz carrier signal.

2.5 Sonar Design Graphs

Initial values of antenna heights, spacing and frequency parameters were assumed in order to perform calculations that reflect the restrictions on space in a typical laboratory environment.
The scale of imaging required for the emulator was implemented after consulting the design graphs that follow. The design graphs that follow were plotted using equations reviewed in the preceding sections of this chapter. The lower limit to baseline length was imposed by the fact that the readily available 40 kHz sonar transducers that were to be used for the design investigation each had a diameter of 16 mm. It was also assumed in the design graphs that a scene for imaging was to be placed onto a mobile platform of height 13 cm from the ground for imaging from a mounted antenna platform. A cross-section of the imaging geometry is depicted in Figure 2.9.
Figures 2.10 to 2.14 were plotted using the following geometry and assumptions:

- Sonar transmitter antenna height is 1.4 m above the ground. Note that for the experiments, the transmitter antenna height relative to the scene is 1.27 m, as a result of the use of the platform

- Sonar transmitters and receivers are identical (diameter 16 mm). Transmitter TX1 is to be placed at the bottom and three receivers, with names RX1, RX2 and RX3, are to be placed above it, one on top of the other, all on a platform that is oriented 45^o from the vertical. This platform in turn will be mounted onto a stepper motor controlled platform on a straight track that will be standing on a table.
- The incidence angle for the scene (in slant range) would be 39^o at near range, 53^o at mid range and 62^o at far range .
- Figure 2.9 shows the observation angles, measured from the vertical, from the transmitter to the scene to be 39^o at near range and 62^o at far range (spanning an angle of 23^o) . Mid range would have an observation angle measured from the vertical of 53^o.
- Slant range would be 1.648 m at near range, 2.122 m at mid range and 2.671 m at far range
- Ground range would be 1.05 m at near range, 1.7 m at mid range and 2.35 m at far range
- Calculations also assume a centre frequency f_0 of 40.55 kHz (corresponding to a wavelength of 0.0084 m) and a pulse bandwidth of 2.5 kHz. These parameters were assumed to be suitable for use with the sonar transducers that were planned to be used.
- The sampling frequency is set to 94340 Hz for each input channel since this is more than double the highest frequency that needs to to be sampled.
- The temperature affects the speed of propagation of sonar signals in dry air and was calculated to be $340.5\, m.s^{-1}$ for an assumed temperature of 15^oC.
- The aperture length of 33.4 cm is to be sampled in spacings of 1.7 mm in cross range.
- The size of a typical focussed scene is 1.3 m in ground range by 0.93 m in cross range.

The previously stated geometrical assumptions are illustrated in Figure 2.9.

It is desirable for coherence between images obtained from the emulator at mid-swath not to drop below 0.8, which is the calculated value as seen in Figure 2.10 for a baseline of 32 mm. The receiver transducers are 16 mm in diameter and therefore impose a lower limit of 16 mm on the smallest baseline. As a result of this limitation, the most sensible baseline choices for achieving mid-swath coherences above 0.8 are baselines of length 16 mm and 32 mm.

Figure 2.11 shows that for the previously discussed baselines of 16 mm and 32 mm, the displacement standard deviation is approximately the same for near-, mid-, and far-swath for the chosen geometry. The 16 mm baseline corresponds to a displacement standard deviation of approximately 125 mm, while a 32 mm baseline corresponds to a displacement standard deviation of approximately 80 mm.

Figure 2.12 shows plots of phase standard deviation versus coherence for interferograms that are not averaged using a smoothing window, as well as a plot for the result of the interferogram being smoothed by a 4-by-4 independent resolution cell smoothing window. Notice that after applying a 4-by-4 independent resolution cell smoothing window (i.e. a

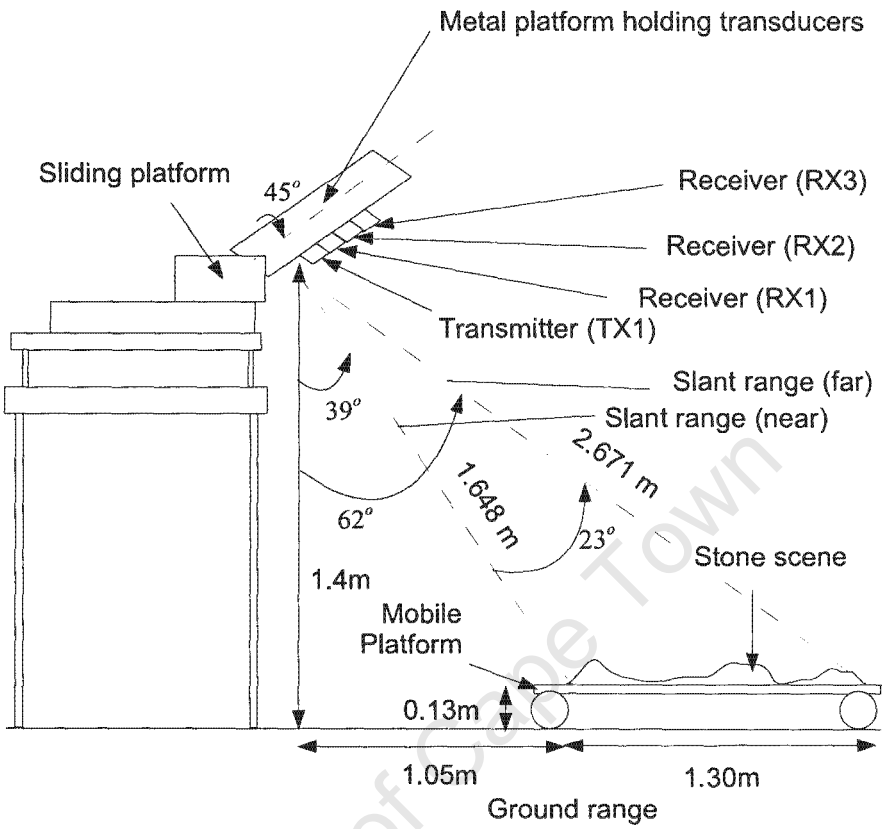

Figure 2.9: Side view of assumed geometry for design purposes

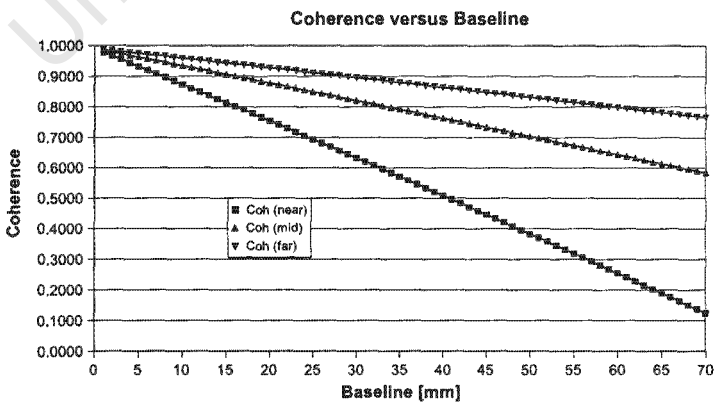

Figure 2.10: Coherence versus baseline

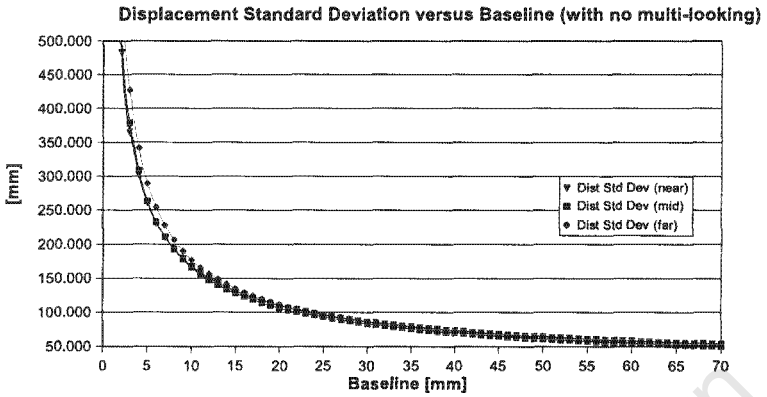

Figure 2.11: Displacement standard deviation versus baseline

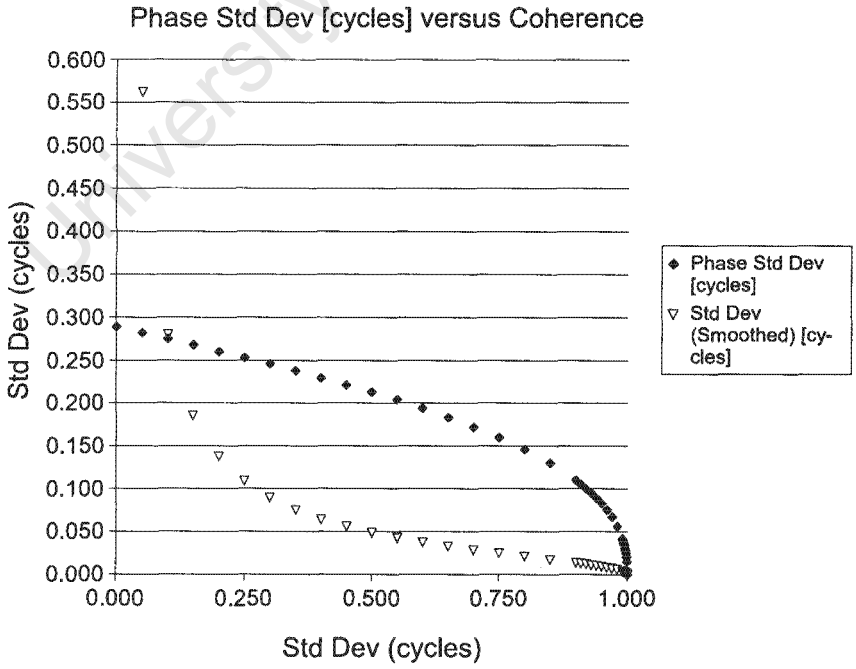

Figure 2.12: Phase standard deviation (without and with smoothing) versus coherence

window effectively containing 4×4=16 statistically independent samples), phase standard deviation decreases quite dramatically.

Figure 2.13 shows a plot of phase standard deviation as a function of baseline; Figure 2.14 shows fringe spacing on a slant-range interferogram as a function of baseline.

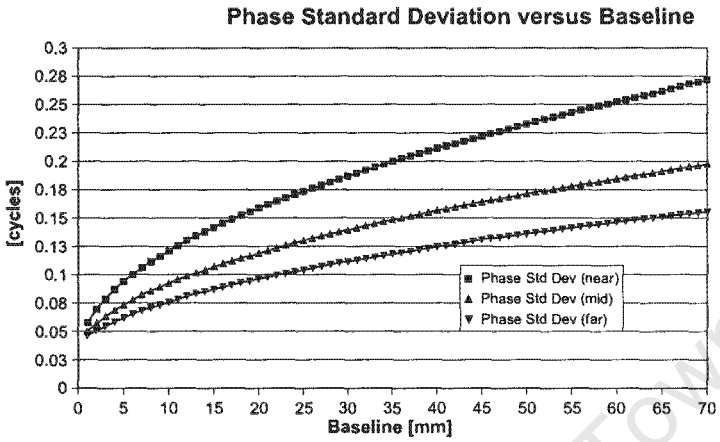

Figure 2.13: Phase standard deviation versus baseline

Figure 2.15 shows a plot of slant range versus ground range as measured from a point at different heights H1 = 1 m, H2 = 2 m, and H3 = 3 m. The plot is shown for values of ground range from 0 m to 5 m.

Figure 2.16 is a plot of the ratio of (ground range resolution/slant range resolution) versus observation angle. For a fixed value of slant range resolution, the ground range resolution value varies as a function of observation angle. This graph is needed in order to determine ground range resolution from near to far swath. The ratio is calculated by using an incidence angle $\theta_{incidence}$ from the vertical that varies from 8^{o} to 90^{0}. The ground range to slant range ratio can be approximated by $\frac{1}{sin(\theta_{incidence})}$. The graph indicates that increase in incidence angle improves the resolution until ground-range resolution equals slant range resolution.

Figure 2.17 shows a plot of slant range resolution versus bandwidth using equation 2.12 and sweeping over values of bandwidth from 1 kHz to 10 kHz. According to this graph, approximately 2.5 kHz bandwidth corresponds to a slant range resolution of approximately 0.07 m .

From Figures 2.16 and 2.17, the approximate ground range resolutions for the chosen geometry and 2.5 kHz bandwidth are therefore:

near ground range: $1.5 \times 0.07 = 0.105$ m = 10.5 cm

mid ground range: $1.2 \times 0.07 = 0.084$ m = 8.4 cm

far ground range: $1.1 \times 0.07 = 0.077$ m = 7.7 cm

From aperture theory, the 3 dB beamwidth $\theta_{1\,antenna}$ of an antenna operating as either transmitter or receiver is given by

$$\theta_{1\,antenna} \approx \frac{\lambda}{D} \tag{2.38}$$

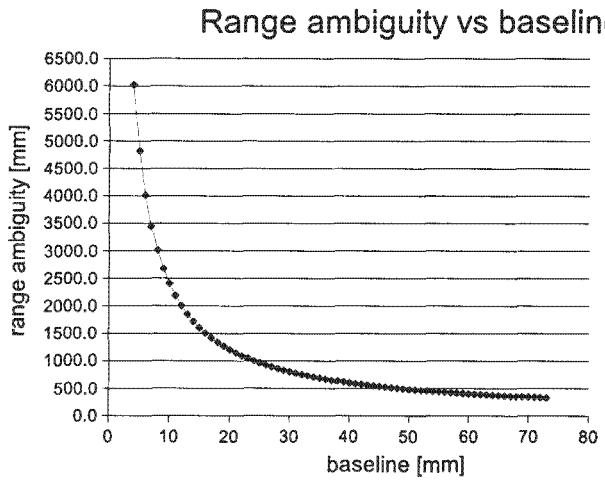

Figure 2.14: Range ambiguity in slant range (corresponding to fringe spacing on a slant-range interferogram) versus baseline

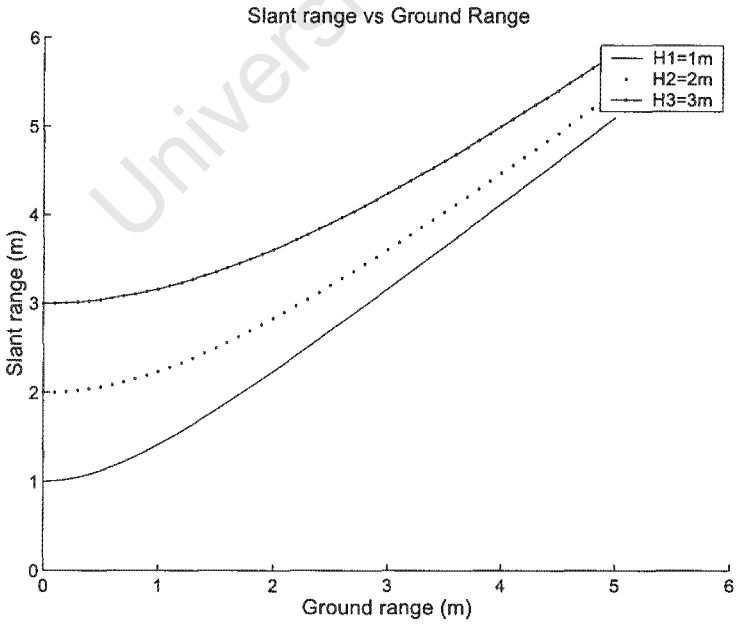

Figure 2.15: Slant range versus ground range as seen from different heights above a flat scene

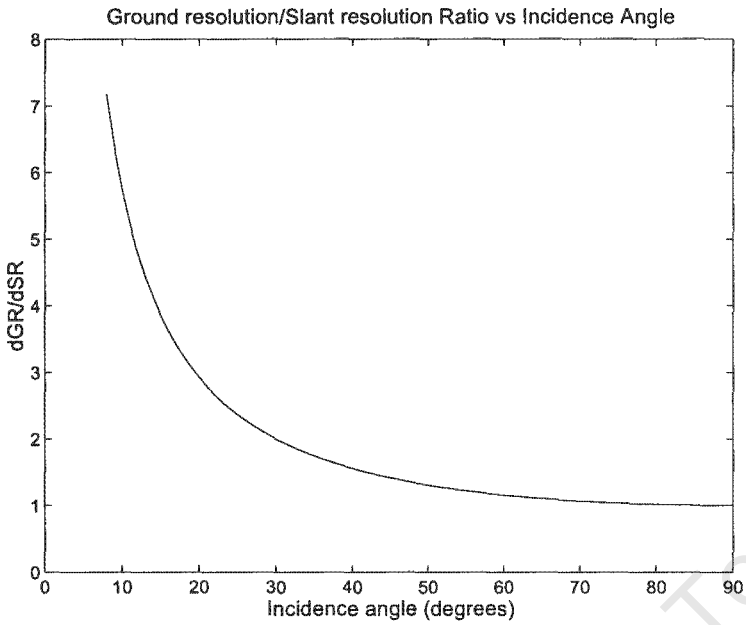

Figure 2.16: Ground range resolution/slant range resolution versus incidence angle

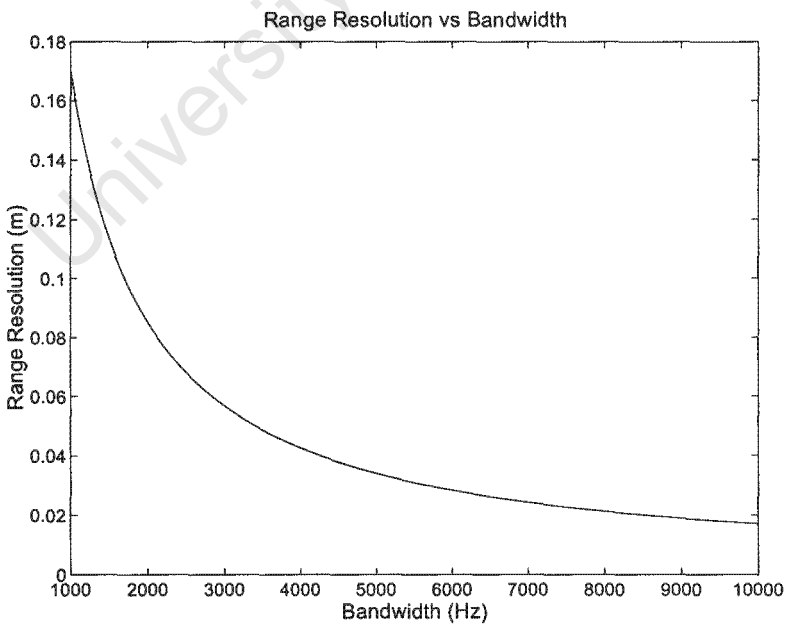

Figure 2.17: Slant range resolution versus bandwidth

where λ is the wavelength of the transmitting frequency and D is the aperture width. For the case of a synthesised aperture in which both the transmitter and receiver are moved along a track of length D, the synthesised beamwidth $\theta_{2\,antennas}$ is:

$$\theta_{2\,antennas} \approx \frac{\lambda}{2D} \tag{2.39}$$

The factor of $\frac{1}{2}$ is a result of the fact that the (two-way) phase changes at twice the rate if both the transmitter and receiver are moved across the aperture length.

The cross range resolution CR for a focussed point target is then :

$$CR = R_{target} \cdot \theta_{2\,antennas} \tag{2.40}$$

where R_{target} is the closest approach range to the target.

The cross range resolution varies over the swath from near to far range. A plot of cross range resolution versus aperture length can be seen in Figure 2.18 for three different values of slant range being r1 = 1 m, r2 = 2 m and r3 = 3 m.

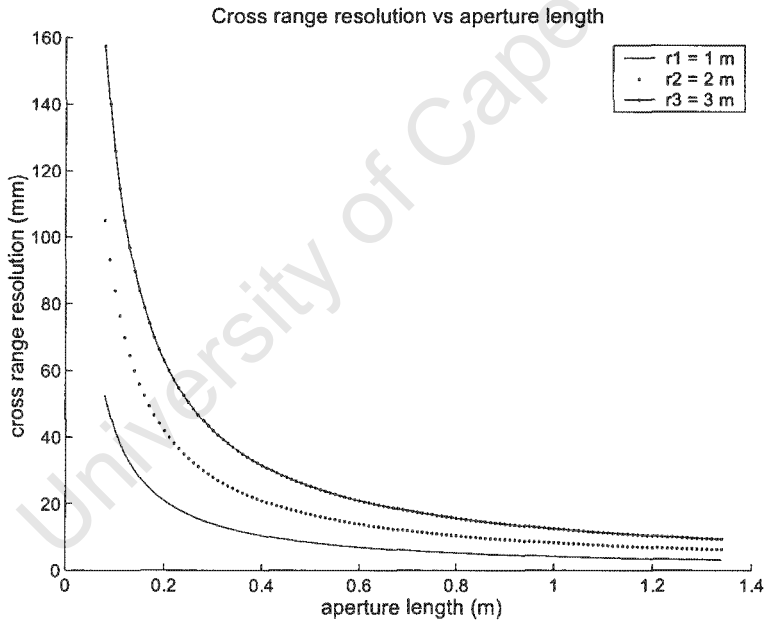

Figure 2.18: Cross range resolution versus aperture length

The beamwidth of the focussed beam is also a function of the offset angle (squint angle) α from boresight, as is illustrated in Figure 2.19. When the data is focussed in the direction perpendicular to the motion of the synthesised aperture (boresight A in Figure 2.19), the cross-resolution is the finest. In contrast, if the data is focussed along angle α from boresight A as indicated in Figure 2.19, the cross range resolution becomes coarser as a result of the synthesised aperture in that direction reducing in size.

As seen in a plot of aperture beamwidth versus angle from boresight in Figure 2.20, aperture beamwidth increases as a function of angle from boresight, the angle from boresight being the direction in which squinting or beamforming at an angle from boresight occurs. This was done assuming a 33.4 cm synthetic aperture with centre frequency of 40.55 kHz and wavelength of 8.4 mm. The increase in squinted beamwidth results in broader cross

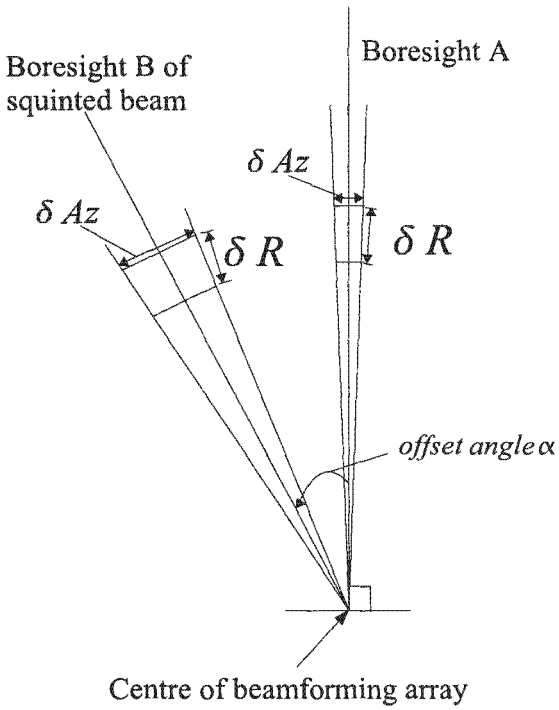

Figure 2.19: Illustration of difference in cross range resolution as offset angle from boresight increases

range resolution. This is due to the smaller aperture size that can be synthesised when beamforming in a direction other than along the boresight. It should be noted that for SAR, the cross range resolution is independent of range. In contrast, the aperture length of the ultrasonic emulator is however of a constant length and hence focussing at a squint angle results in broader cross range resolution.

Figure 2.21 uses the slant range values r1 = 1 m, r2 = 2 m and r3 = 3 m for plotting different cross range resolution curves that correspond to these slant ranges and that illustrate the decrease in cross range resolution as angle from boresight increases. This was done assuming a 33.4 cm synthetic aperture with centre frequency of 40.55 kHz and wavelength of 8.4 mm.

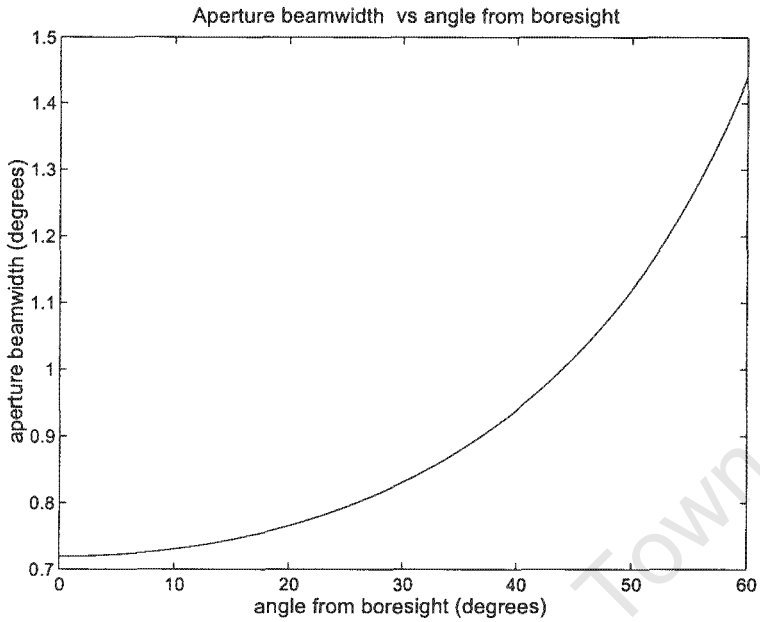

Figure 2.20: Aperture beamwidth versus angle from boresight for a 33.4 cm synthetic aperture (centre frequency of 40.55 kHz and wavelength of 8.4 mm)

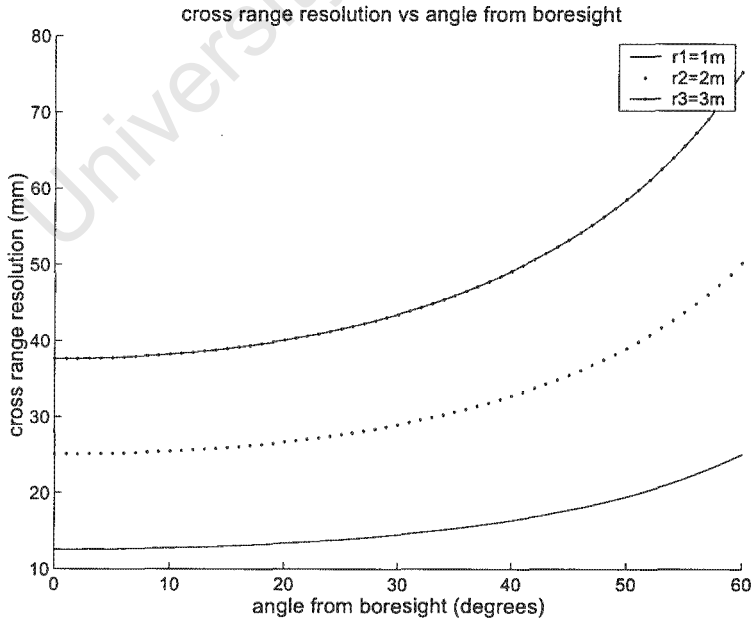

Figure 2.21: Cross range resolution versus angle from boresight for a 33.4 cm synthetic aperture (centre frequency of 40.55 kHz and wavelength of 8.4 mm)

Chapter 3

Emulator Design and Implementation

This chapter describes work done in implementing a suitable emulation system for producing sonar interferograms that emulate characteristics of radar interferograms. Measurements taken using a data acquisition card (DAQ), as well as the physical geometry of the system are described.

3.1 Emulator System Overview

For emulation purposes, at least four channels need to be recorded, one being the recording of the amplified and filtered transmitted signal (referred to as "local loopback"). This channel is used in order to remove time delays. Three other channels that each record data from a different receiver are necessary in order to have more than two baselines. The design of the multiple antenna single pass interferometry system took into account the following requirements:

- one output channel that could output a signal at a sufficiently high sampling rate, while simultaneously being able to record input signals,
- strict control over the timing of transmission and reception of signals,
- a mechanism for moving the transducers along a straight track that could be controlled by a logic signal sent by the PC, and
- the co-ordination of the movement of the transducers along a track as well as transmission of chirps and recording of echoes.

Figure 3.1 shows a block diagram that illustrates an overview of the input and output processes that are controlled using a PC with data acquisition card (Eagle Technologies PCI703S-16A card).

3.1.1 Output

The output chain of the emulator system consists of an output channel of a data acquisition card that produces an output analogue signal. This is connected to circuitry by means of an external connector. The circuitry consists of a bandpass filter and amplifier. The output of the amplifier is connected to a transformer with a turns ratio of approximately 5:1. The output of the transformer is then connected to the output transducer. This transducer is connected with the intention of placing a voltage of approximately 50 V peak to peak across its terminals during pulse transmission.

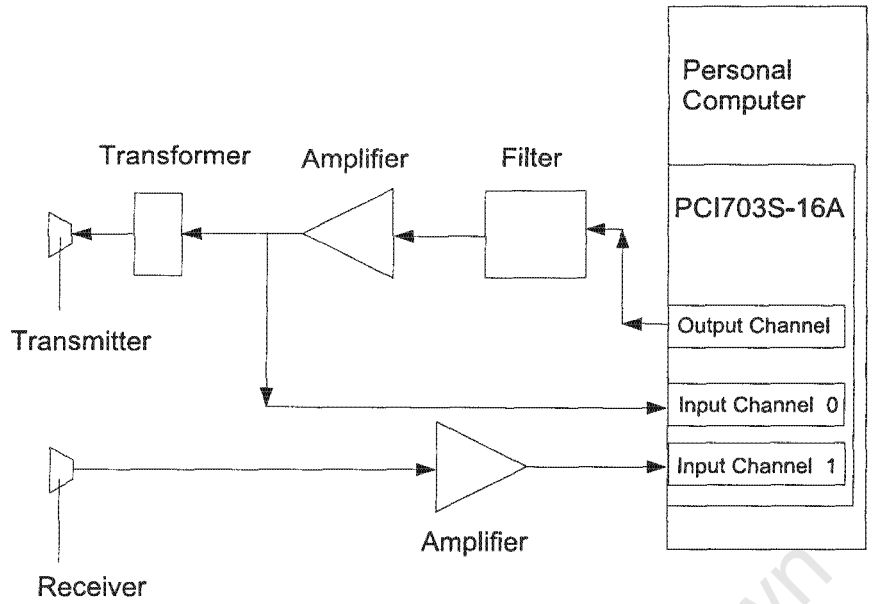

Figure 3.1: Block diagram showing system overview for the simultaneous transmitting and receiving process

3.1.2 Receiver and Transmitter Transducers

Identical SQR40 ultrasonic transducers were used for both transmission and reception of sonar signals. The design decision to use these transducers was because of the approximately constant frequency response of 2.5 kHz centred approximately around 40 kHz.

3.1.3 Input channels

The input channel circuitry consists of three input channels that each consist of the following: a receiver transducer that is connected to a bandpass filter and amplifier that is connected via an external connector to the data acquisition card. Figure 3.2 contains the circuit diagram that is implemented each time for each of the 3 receiver input channels. The circuit uses a cascaded version of a state-variable active filter [16] that performs the bandpass filtering and amplifying function using LMF100 operational amplifiers. Bandpass filtering and amplication functions are tuned by adjusting the variable resistors. The input of Figure 3.2 is connected directly to the output of a receiver transducer. The output of Figure 3.2 is connected to an external connector that in turn is connected to the data acquisition card. The circuit has an output bandwidth of 2.5 kHz centred around 40.55 kHz.

A fourth input channel is connected to the output of the transmitter channel on the data acquisition card on a channel referred to as the "local loopback" channel. This output does not use the input channel circuit in Figure 3.2 but is fed directly into an input channel via a data acquisition card external connector.

3.1.4 Eagle Technologies data acquisition card

The first design consideration was to decide which interface to use to read received signals into the PC. In [18, 24, 20], a sound card of a PC was used with transmitter and receiver circuitry in order to record and transmit signals. However, a major flaw in this design was

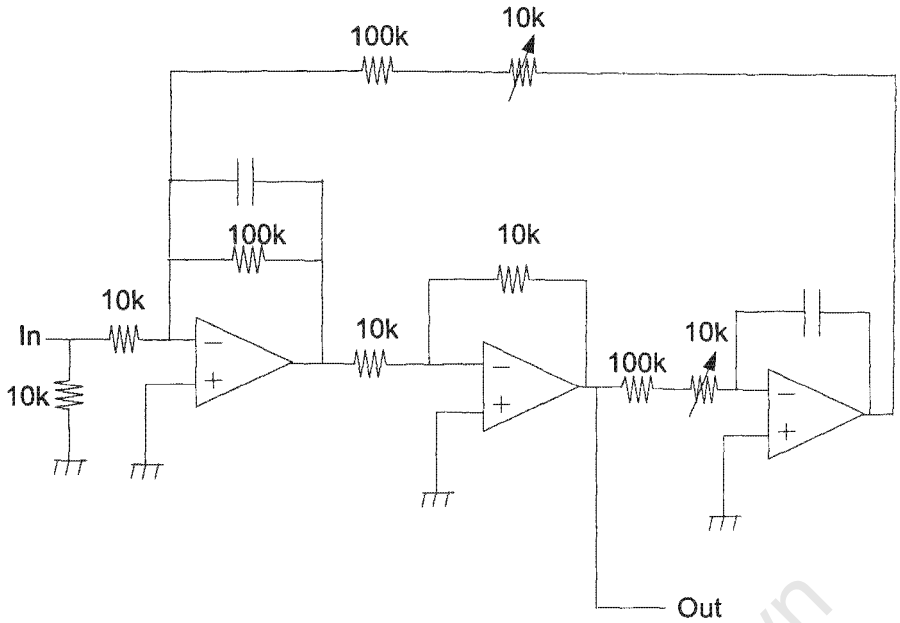

Figure 3.2: Input circuit diagram

the inability to record multiple inputs simultaneously using the sound card of the PC. A design decision was therefore made to use the Eagle Technologies PCI703S-16A because of its ability to simultaneously transmit and receive on multiple channels. Technical details concerning the PCI703S-16A card and programming interfaces were obtained from [3, 2].

The card has the following features that make it desirable for use as part of an emulator system:

- 8 digital input/output lines
- 16 analogue input sampling channels with 14 bit A/D resolution (stable to 12 bits)
- 2 analogue output channels
- an A/D FIFO depth of 4096 samples for storing samples from the sampling channels

According to the documentation of this equipment [2] the PCI703S-16A card can sample N channels simultaneously at 400 kHz/(N+1) where N represents the number of channels that are recording samples. The card is also able to transmit a signal at 400 kHz on the output channel while simultaneously sampling the input channels.

Digital to Analogue Output

The maximum output frequency of the Eagle PCI703S-16A is 400 kHz. The software interface to the card requires parameters to be set so that a sample output frequency of 400 kHz is used to transfer samples in a supplied data buffer to the output of the card.

Data Acquisition Software

The data acquisition software for the interferometric emulator system uses a Matlab script to call an executable that uses C++ functions to use the Eagle data acquisition card.

This executable that is written in the C++ programming language interfaces with the signal generation and signal sampling functions of the Eagle data acquisition card. The C++ programming interface library of functions provided by Eagle Technologies with the PCI703S-16A card provides a means for directly setting up parameters and activation of the input and output functions of the card. Software used in [9] to interface with the Eagle data acquisition card was modified in order to interface with the Eagle data acquisition card. The functions performed by software are summarised in the flowchart of Figure 3.3.

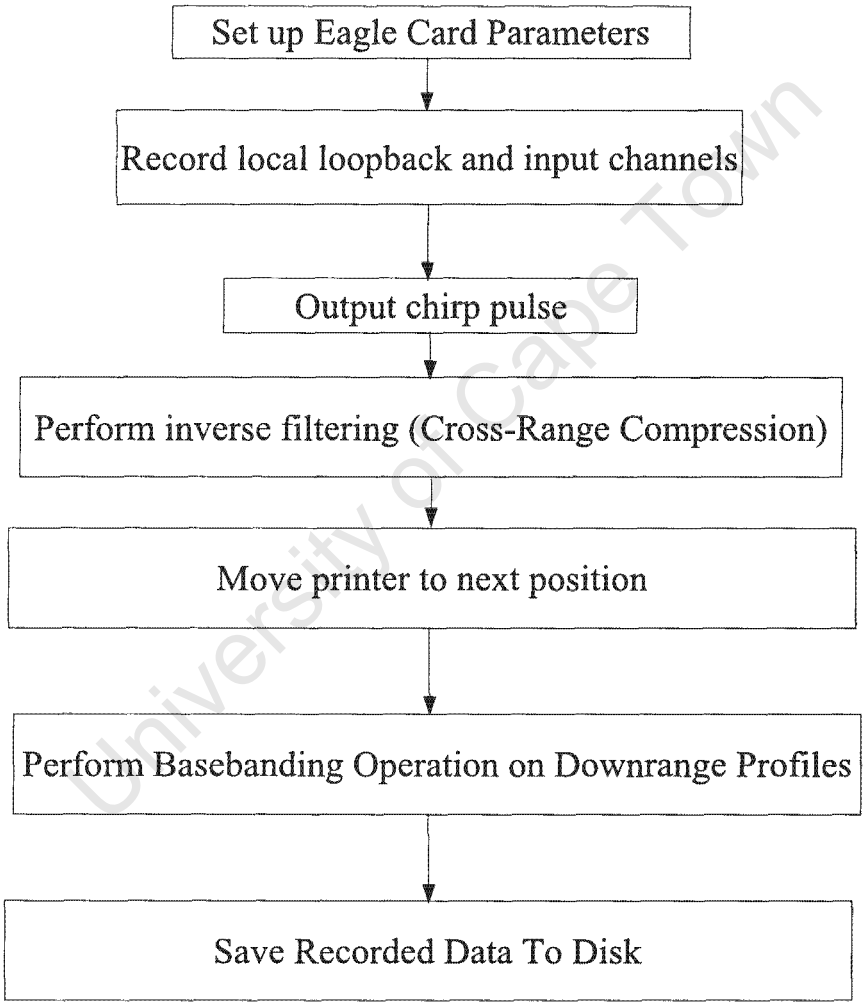

Figure 3.3: Flowchart showing functions performed by software

The previous sections have described the output and input chains for the imaging process as demonstrated in Figure 3.1. The signal from the output analogue channel of an Eagle PCI703S-16A data acquisition card is first filtered and then amplified by circuitry on a printed circuit board. The signal voltage is increased to approximately 50 V peak to peak using a step-up transformer before being fed to an output transducer. The signal on the transmitter chain is recorded on an input channel after being filtered and amplified, as it

is presented on the input side of the transducer. It is used for cross-correlation operations that are similar to matched filtering, but that are used for synchronisation of transmission and recordings of signals. The need for synchronisation is due to the need to cancel the effect of the variable time delay involved in transmitting the output signal. A variable time delay in transmission that is not accounted for causes uncertainty as to the round-trip time and therefore the range to a target.

The output chain is implemented as shown in Figure 3.4 and in the following derived equation, relating the recorded response $V_O(\omega)$ to the transmitted signal $V_{TX}(\omega)$ and the impulse response $\zeta(\omega)$ of the scene

$$\begin{aligned} V_O(\omega) &= V_{TX}(\omega) A_{TX}(\omega) \zeta(\omega) A_{RX}(\omega) H_{rec}(\omega) \\ &= \zeta(\omega) H_S(\omega) \end{aligned} \tag{3.1}$$

$A_{TX}(\omega)$ represents the response of the output stage and the 40 kHz transmitting transducer. $A_{RX}(\omega)$ represents the reshaping effects of receiving transducer and the input circuitry involved in the input stage for the input channels. $H_{rec}(\omega)$ models the response of the amplifiers and filters that are applied to the signal between transmission and recording by the data acquisition card. $H_S(\omega)$ is the system response, combining all the linear system effects.

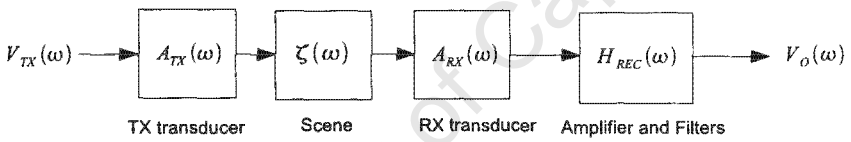

Figure 3.4: Implementation of output chain

Signal Processing

The signal processing involves two steps:

1. time alignment of the return echo via correlation of the received signal with the local loopback recording of the transmitted signal, and
2. application of an inverse filter to deconvolve all linear system effects.

The signal processing involved in inverse filtering is implemented in the frequency domain as

$$\zeta(\omega) = V_O(\omega) H_C(\omega) H_d(\omega) \tag{3.2}$$

where $V_O(\omega)$ is the signal that will be inverse filtered. This correlation filtering is achieved by using $H_C(\omega)$, the complex conjugate of $V_{LL}(\omega)$ that is recorded on the first channel

The signal that is received on the first receiver channel is shown in Figure 3.7. The filtering and distortion effects on the transmitted signal are seen in the recording. The signal is still clearly 5 ms in length after passing through the transducers, air and after being amplified and filtered. The received signal clearly needs to have compensation introduced for system distortions in order for signal compression efficiency to be maximised.

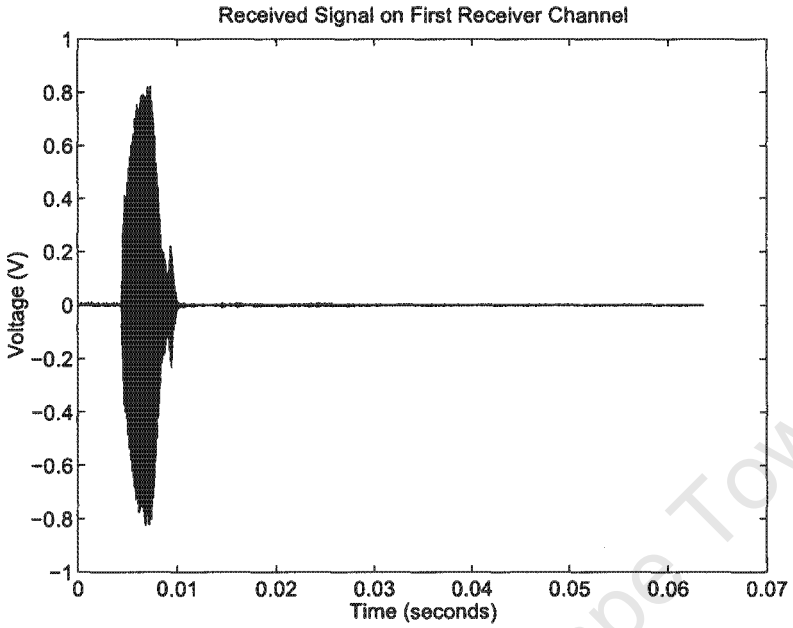

Figure 3.7: Received signal from the first receiver channel

The previously mentioned filtering and distortion effects are most clearly seen in the frequency domain. Figure 3.8 shows the magnitude of the positive frequency spectrum of the recorded local loopback signal in the frequency domain. After system effects are introduced, Figure 3.9 shows the magnitude of the positive portion of the FFT of the returned signal from the receiver connected to the first receiver channel. A comparison of the two previously mentioned figures clearly shows the resultant decrease in bandwidth of the frequency spectrum. The amplitudes of certain frequency components have also clearly become smaller.

Figure 3.10 shows the positive frequency spectrum of the matched filter that is used on all channels in order to remove the variable time delay. All frequency components other than those shown on the graph are zeroed out. The bandwidth that is usable for signal processing as measured from this figure is 2.5 kHz.

Figure 3.11 shows the result of matched filtering the first receiver channel's recording.

Figure 3.12 shows the magnitude of the FFT of the inverse filter that is used to compensate for the system effects on the received data.

The magnitude of the FFT of the inverse filtered signal on the first receiver channel, as shown in Figure 3.13 is clearly rectangular. The corresponding slant range compressed signal is shown in Figure 3.14 where the time axis has been relabelled to the corresponding range r in metres using the equation

$$r = \frac{c.t}{2}$$

where c is the speed of sound and t is the time value. Notice the characteristic $\left|\frac{sin(x)}{x}\right|$ shape of the range compressed signal.

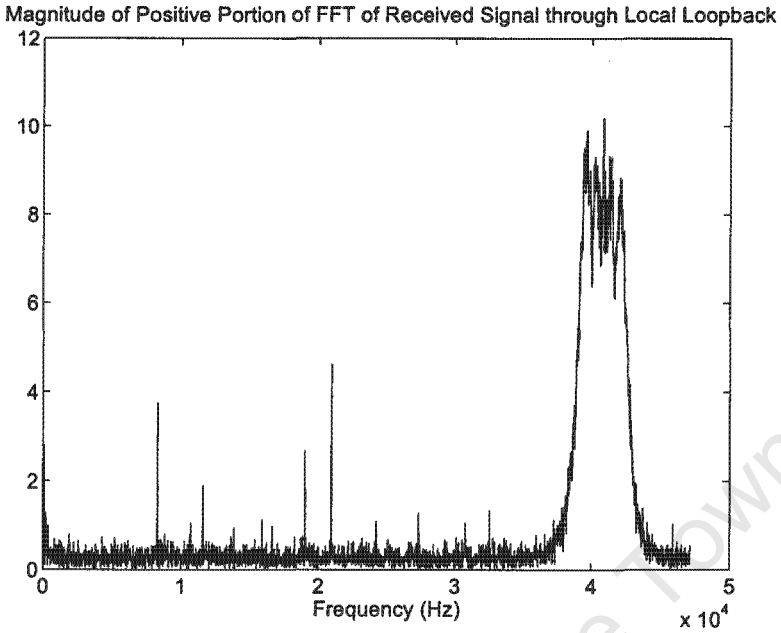

Figure 3.8: Magnitude of FFT of Local Loopback Signal

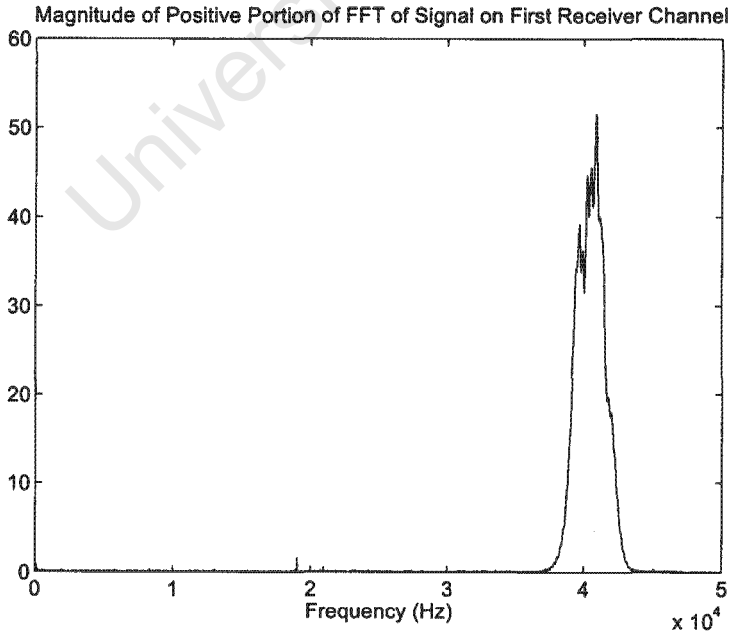

Figure 3.9: Magnitude of FFT of first receiver channel signal

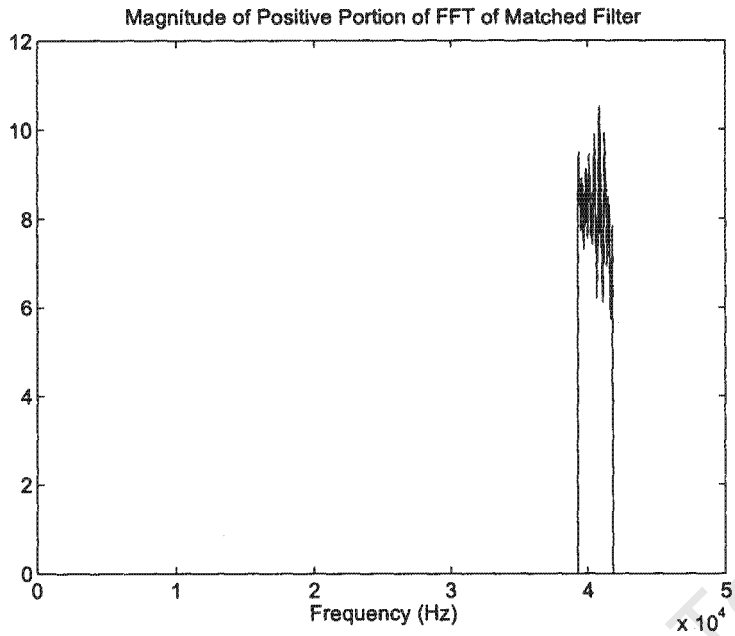

Figure 3.10: Magnitude of positive frequency spectrum of the FFT of the matched filter

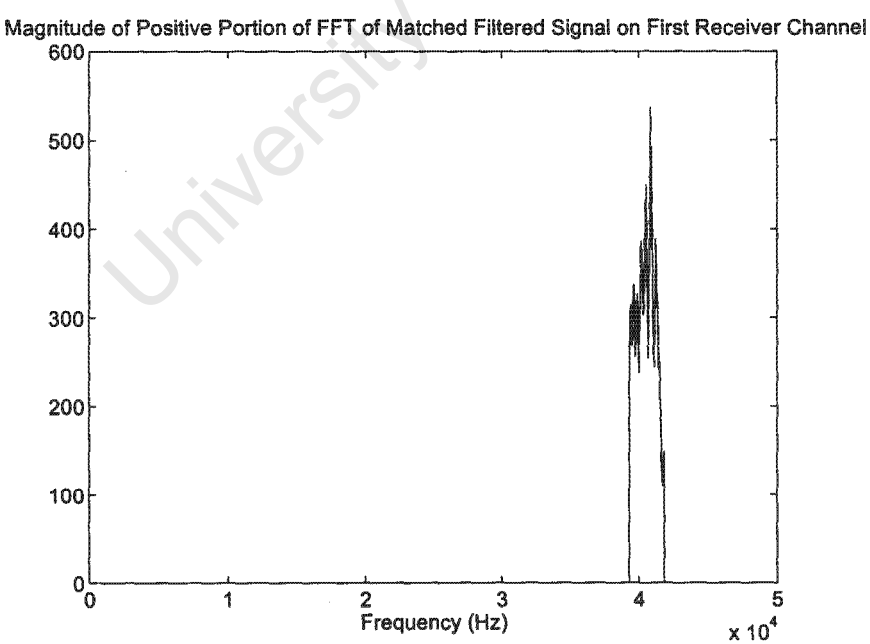

Figure 3.11: Magnitude of the FFT of the time-compensated matched filtered result for the first receiver channel

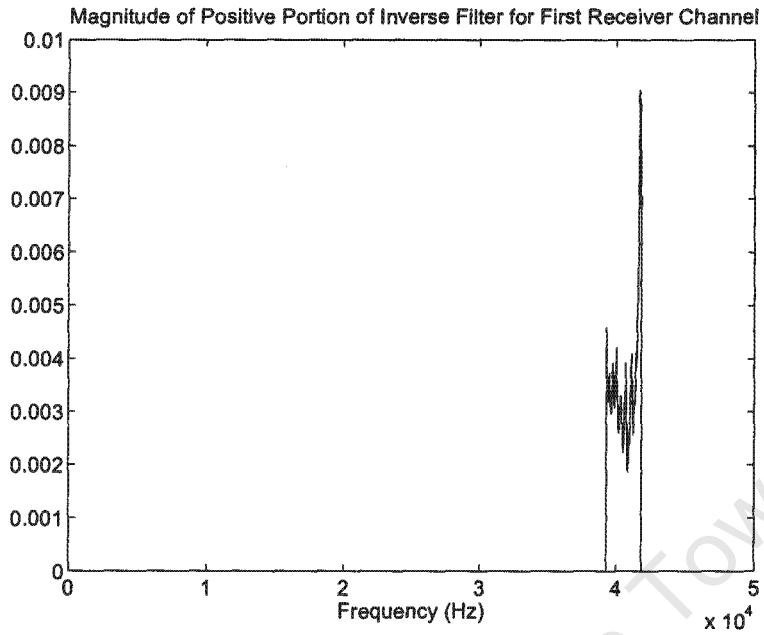

Figure 3.12: Magnitude of the positive frequency spectrum of the FFT of the reshaping filter

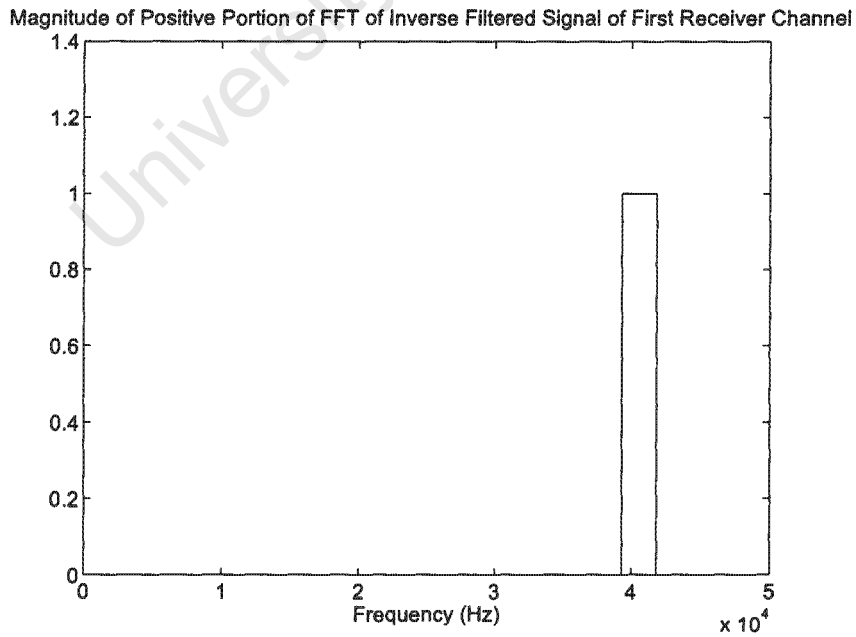

Figure 3.13: Magnitude of the FFT of the inverse filtered signal of the first receiver channel

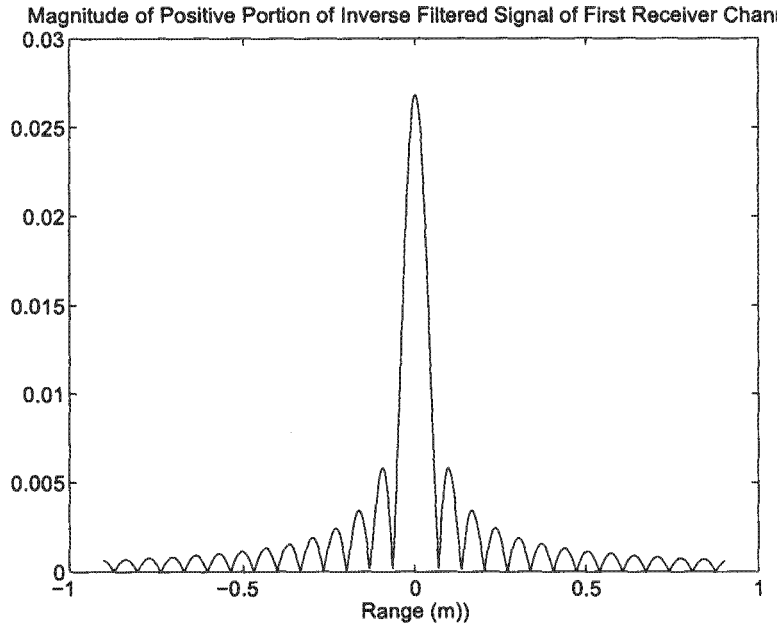

Figure 3.14: Magnitude of the inverse filtered signal of the first receiver channel

Figure 3.15 shows the magnitude of the inverse filtered signal of Figure 3.14 after basebanding, while Figure 3.16 shows the phase of the basebanded signal. Notice that the phase is flat over the main lobe of the basebanded signal.

In order to suppress sidelobes, a Hanning window is applied in the frequency domain as shown in Figure 3.17.

Figure 3.18 shows the frequency spectrum of the signal received on the first receiver channel after basebanding but before applying the Hanning window in the frequency domain.

Figure 3.19 clearly shows the suppression of sidelobes and broadening of the main lobe after applying a Hanning window.

Figure 3.20 shows the constant phase over the main lobe of the downrange profile is maintained.

3.1.6 Emulator Physical Setup

The printed circuit board used for the experiments is shown in Figure 3.21. Only the output stage of the circuit board was used for the purposes of this dissertation. The printed circuit board was the result of work done by Stewart Reid in implementing a printed circuit board version of the circuitry described in [24, 20].

Notice the output transformer that is used for the amplification of the output signal that is placed across the terminals of the output transducer in Figure 3.21 with a winding ratio of approximately 5:1. This was wound by the author of this dissertation and placed on the printed circuit board. The output voltage of the amplifier that is placed across the terminals of the transformer is typically of magnitude 10 V peak to peak and the output voltage of the transformer is then typically 50 V peak to peak.

The computer and input circuitry setup can be seen in Figure 3.22.

The bottom transducer TX1 functioned as the transmitter while the three transducers RX1, RX2 and RX3 above TX1 functioned as receivers, as indicated in Figure 3.23. All transducers were placed one on top of the other. Each transducer had a diameter of 16 mm.

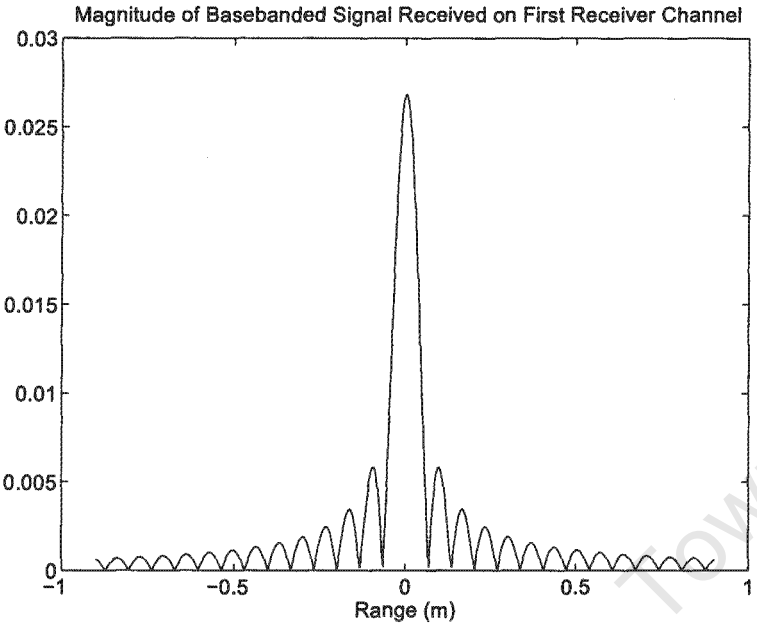

Figure 3.15: Magnitude of the basebanded and inverse filtered signal of the first receiver channel

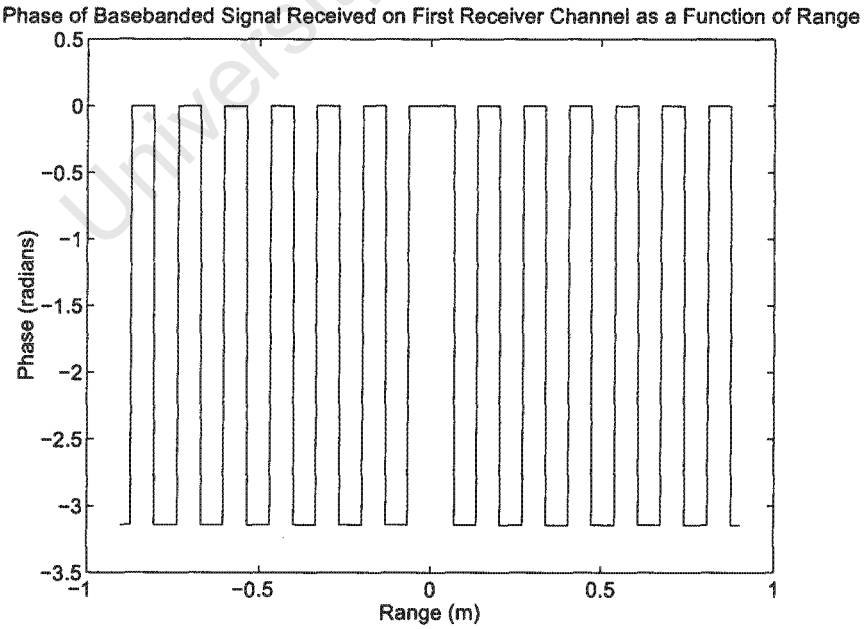

Figure 3.16: Phase of the basebanded and inverse filtered signal of the first receiver channel

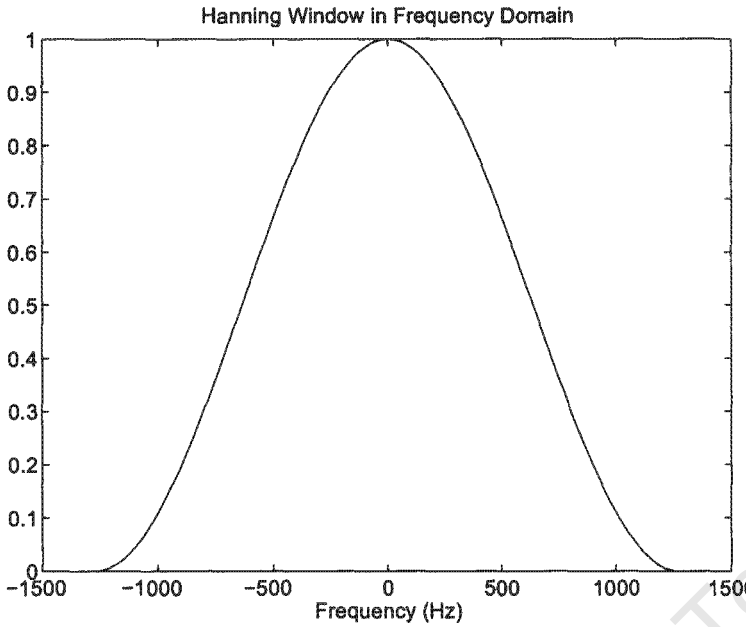

Figure 3.17: Hanning window that is applied in the frequency domain

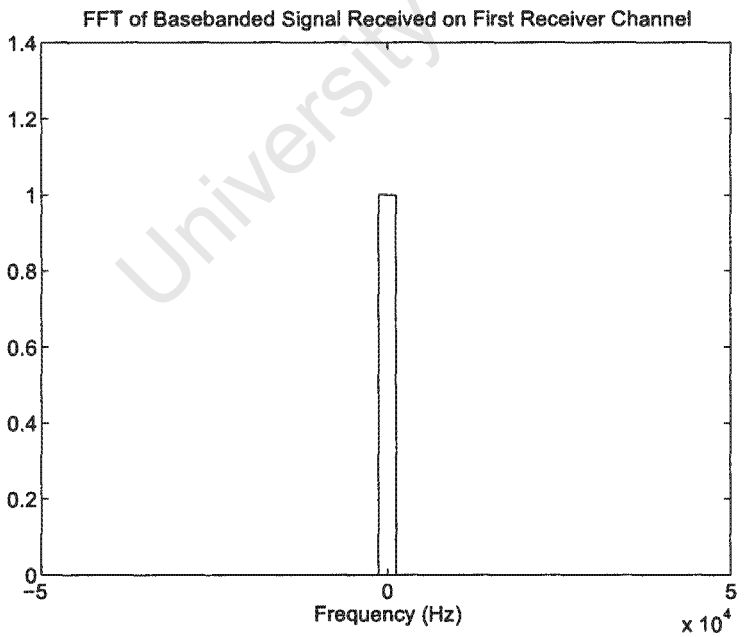

Figure 3.18: FFT of basebanded and inverse filtered first receiver channel signal before the Hanning window is applied

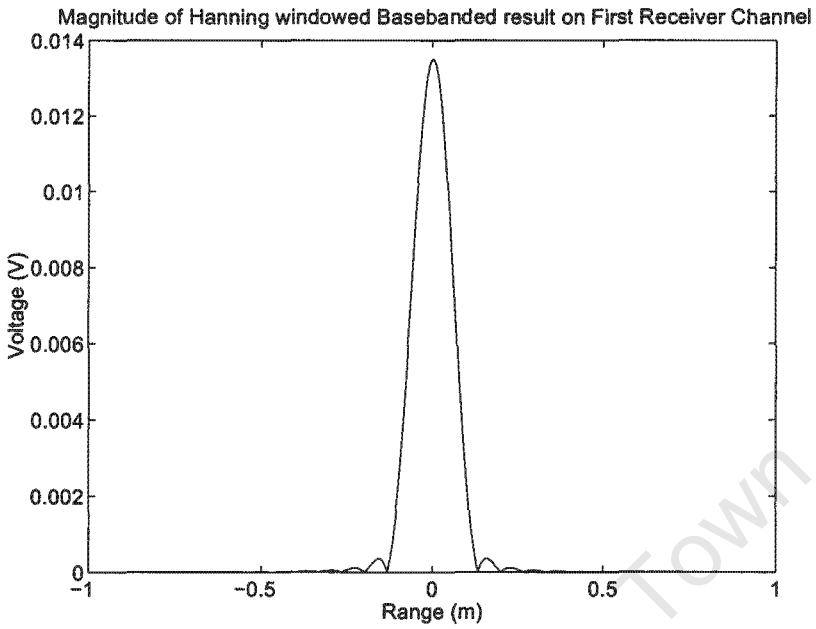

Figure 3.19: Magnitude of basebanded and inverse filtered first receiver channel signal after the Hanning window is applied

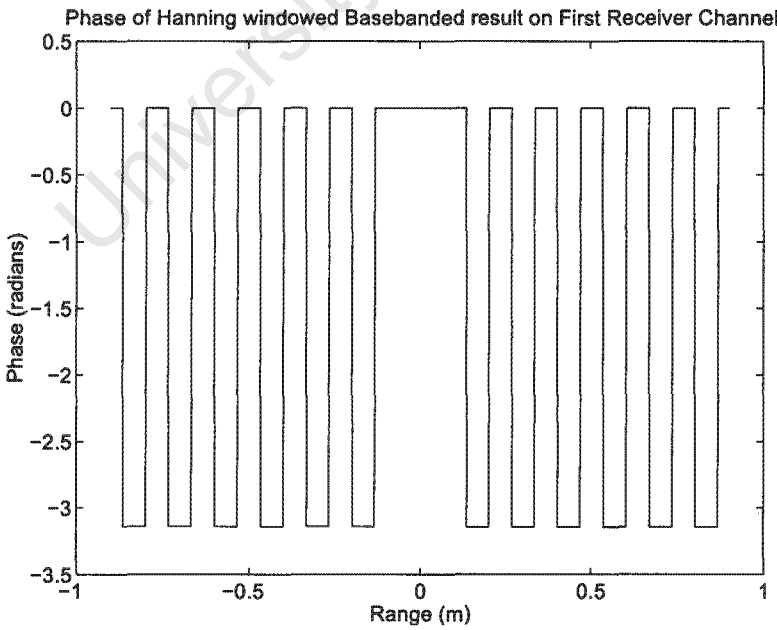

Figure 3.20: Phase of basebanded and inverse filtered first receiver channel signal after the Hanning window is applied

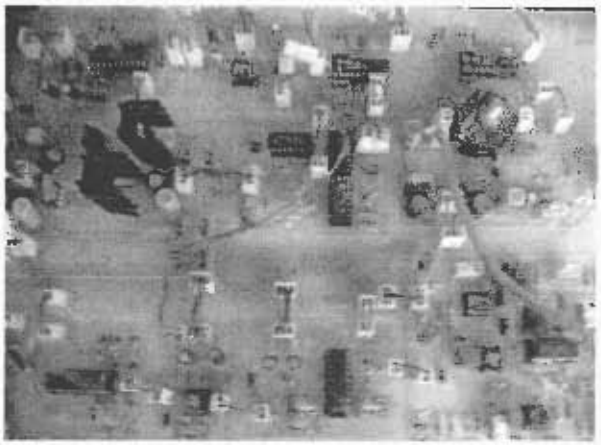

Figure 3.21: Printed circuit board with output transformer

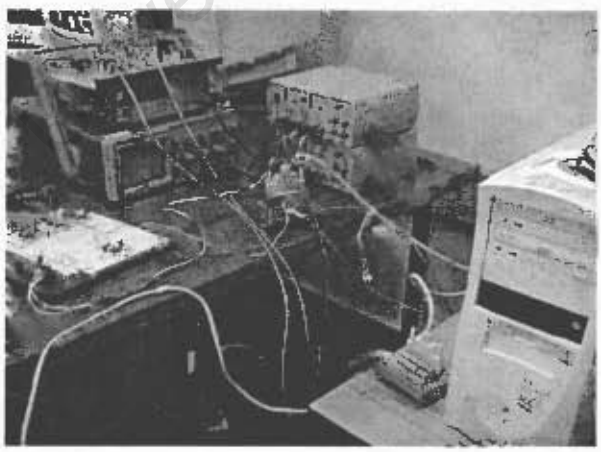

Figure 3.22: Computer and input circuitry setup

The baselines between receivers that were used for interferometric imaging were 16 mm between RX1 and RX2, and 32 mm between RX1 and RX3.

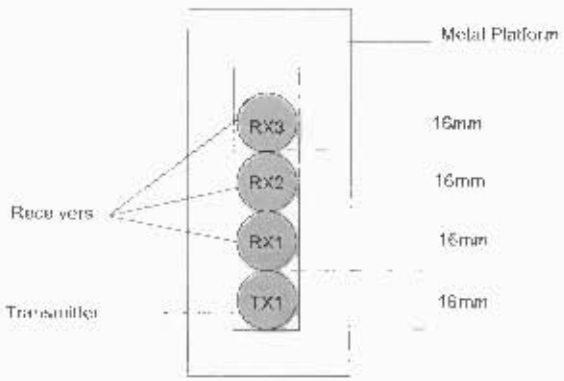

Figure 3.23: Transducer platform and geometry setup

The physical setup and geometry of the imaged scenes that are described in this dissertation are illustrated in the top view of the geometry of the emulator in Figure 3.24 and in the side view that was shown in Figure 2.9. Four identical SQR40 transducers were used, one functioning as the output transducer and three functioning as input transducers. An old-fashioned dot-matrix printer was modified to provide the moving platform. Input and output transducers were placed on a metal platform that was fitted onto the printer head on the printer rail as seen in Figure 3.25. The printer head moves approximately 0.42 mm for each step. The design decision was made to move the printer head 4 steps or 1.7 mm each time after recording each downrange profile. It takes approximately 3 minutes to record one aperture length of 33.4 cm.

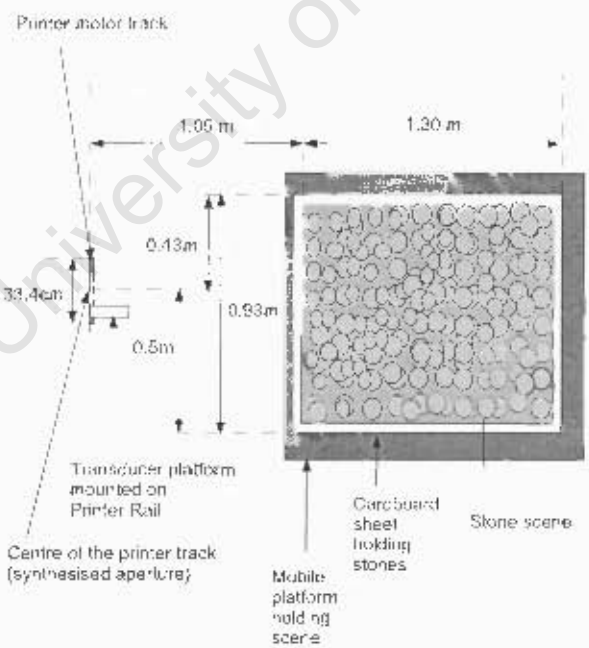

Figure 3.24: Top view of geometry of emulator

The generic scene that was used for imaging was a scattered stone scene (with stone size of average diameter 5 mm) that was placed on a flat-surfaced wheeled mobile platform to emulate a distributed scatterer scene. This is shown in Figure 3.26.

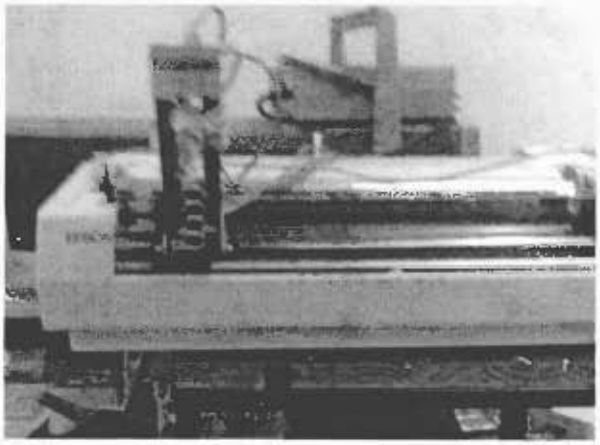

Figure 3.25: Printer rail fitted with input and output transducers

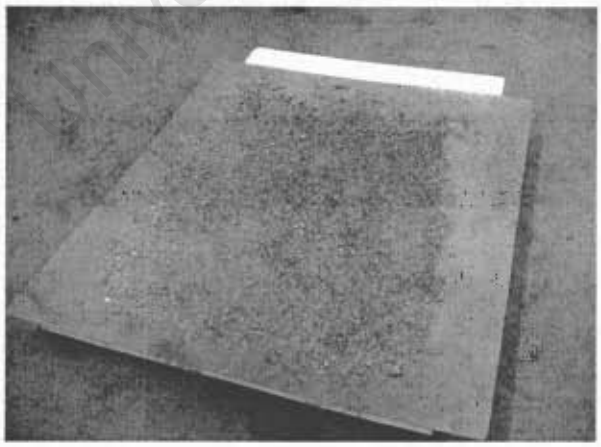

Figure 3.26: Distributed scatterer stone scene

3.1.7 Emulator System Output Data Format and Storage

The output of the recording process consists of three files that each contain the basebanded range-compressed receiver channel information recordings of one of the three receiver channels respectively. These files are stored in a matrix format in Matlab files that are saved on disk. These files are then used by further signal processing scripts written in Matlab to form focussed images.

Chapter 4

Cross range focussing and interferogram formation from beamforming array data

This chapter first describes the calculations required to determine required synthetic aperture size. The sonar beamforming algorithm that was used is then discussed, followed by steps taken after beamforming to form a sonar interferogram. This chapter concludes with a discussion of major differences between radar and sonar interferograms that use synthetic aperture and beamforming techniques respectively.

4.1 Sonar synthetic aperture and beamforming design

This section first discusses calculations required to determine synthetic aperture size for a chosen resolution. This is followed by a discussion of the implemented beamforming algorithm.

4.1.1 Sonar synthetic aperture

The beam from a radiating aperture is initially columnated in the so-called "near field" and then diverges (in the "far field").

The identical sonar SQR40 40 kHz transducers that were used as transmitter and receivers each had a diameter of 16 mm that included external casing, but a circular aperture of diameter D of 14 mm. For a centre frequency of 40.55 kHz the wavelength λ of the transmitted signal is calculated using equation 2.13:

$$\begin{aligned} \lambda &= \frac{c}{f_0} \\ &= \frac{340.5}{40550} \\ &= 0.0084\,m \\ &= 8.4\,mm \end{aligned}$$

The near to far field transition region for sonar transducers with aperture diameter 14 mm is approximately [17]

$$\frac{2D^2}{\lambda} = \frac{2 \times 0.014^2}{0.0084}$$

$$= 0.047 \text{ m}$$

$$= 4.7\,cm$$

Figure 4.1 shows a cross section side view of a sonar transducer. It also illustrates the aperture size, the near field region that extends to 4.7 cm, and the far field region that extends beyond 4.7 cm in range.

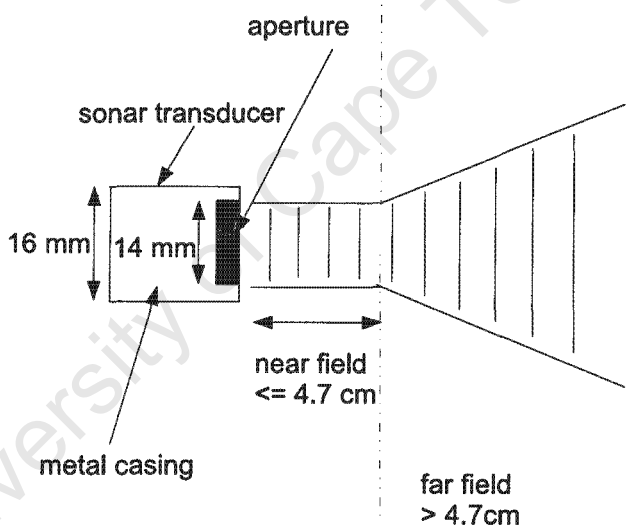

Figure 4.1: Cross section side view of a sonar transducer as well as near field and far field regions

As a result of the far field region extending beyond 4.7 cm, all the targets will be in the far field of the transducer in the geometry of the scene as described in section 2.5 and illustrated in Figure 2.9.

The 3 dB far field beamwidth of the SQR40 transducers can be calulated using the formula for the 3 dB beamwidth from equation 2.38 as follows:

$$\begin{aligned}\theta_{3\,dB} &= arcsin\left(\frac{\lambda}{D}\right)\\ &= arcsin\left(\frac{0.0084}{0.014}\right)\\ &\approx 37^o\end{aligned}$$

Using the same transducer as the transmitter and receiver effectively makes this 37^o beamwidth the 6 dB beamwidth. The geometry of the scene as described in section 2.5 and illustrated in Figure 2.9 falls within this 37^o 6 dB beamwidth since the angular span of illuminated scene from near to far swath of the imaging transducers is 23^o.

The maximum size of the synthesised aperture D_{max} is limited by the 3 dB beamwidth in cross range. For a slant range R_0 to a point target and 3 dB beamwidth θ the maximum aperture length for which targets will remain in the 3 dB beamwidth is

$$D_{max} = 2R_0 tan\left(\frac{\theta}{2}\right)$$

The value of D_{max} at far swath is limited by the value of zero-Doppler range R_0. For $R_0 = 2.7\,m$ at far swath,

$$\begin{aligned}D_{max} &= 2 \times 2.7 \times tan\left(\frac{37^o}{2}\right)\\ &\approx 1.8\,m\end{aligned}$$

The cross range resolution of the focussed beam δx at range R is calculated using the 3 dB beamwidth $\theta_{2\,antennas}$ of the synthesised aperture for an identical transmitter and receiver pair as follows:

$$\delta x = \theta_{2\,antennas} \times R \tag{4.1}$$

Rearranging terms and substituting equation 2.39, the calculation of the approximation for minimum aperture width D_{min} to produce square ground range pixels of ground range resolution 7.7 cm at far swath with a total bandwidth of 2.5 kHz processed (as mentioned in section 2.5) where $R \approx 2.7$ m is

$$\begin{aligned}D_{min} &= \frac{\lambda R}{2\delta x}\\ &= \frac{0.0084 \times 2.7}{2 \times 0.077}\\ &\approx 0.147\,m\\ &= 14.7\,cm\end{aligned}$$

The minimum aperture length needed to achieve square ground range pixels is 14.7 cm. In the experimental work reported in chapter 5, a somewhat larger synthetic aperture of size 33.4 cm was used. This synthetic aperture size of $D = 33.4\,cm$ corresponds to a finer cross range resolution at far swath of

$$\begin{aligned} \frac{\lambda R}{2D} &= \frac{0.0084 \times 2.7}{2 \times 0.334} \\ &= 0.034\,m \\ &= 3.4\,cm \end{aligned}$$

4.1.2 Time-domain based fixed-length array beamforming

The beamforming algorithm that is described in this section uses unfocussed data that has been received from the emulator and that has subsequently been inverse filtered, Hanning windowed and basebanded. The algorithm employs a method that focusses the pixels in the imaged scene on a flat surface relative to the centre of a fixed array of antenna positions using the two way range to the pixel under consideration for focussing.

The beamforming algorithm sums range compensated and phase aligned responses from points on a flat ground scene. This is achieved by rotating the phase by an appropriate amount in order to perform coherent addition of the phase response.

Figure 4.2 shows the parameters that are used in the description of the beamforming algorithm that follows.

$R(i)$ represents the round-trip distance to a pixel on the focussing grid from antennas $TX(i)$ and $RX(i)$, the transmitter and receiver at position i in the beamforming array. $R\_TX(i)$ represents the distance from $TX(i)$ to the pixel and $R\_RX(i)$ represents the distance from $RX(i)$ to the pixel. The round trip range is given by

$$R(i) = R\_TX(i) + R\_RX(i) \tag{4.2}$$

Similarly, R_mid represents the round trip range to a pixel on the focussing grid from antennas TX_mid and RX_mid, the transmitter and receiver at the middle position in the beamforming array. R_TX_mid represents the distance from TX_mid to the pixel and R_RX_mid represents the distance from RX_mid to the pixel. The round trip range from the middle of the array is given by

$$R\_mid(i) = R\_TX\_mid(i) + R\_RX\_mid(i) \tag{4.3}$$

$V_{foc}(x, y)$ is the pixel on the plane that is being focussed corresponding to cross-range x and ground range y, and is calculated by

$$V_{foc}(x,y) = \frac{\sum_{i=1}^{N} V_i(t(x,y)) \left(\frac{1}{R\_TX(i)} \times \frac{1}{R\_RX(i)}\right) \times exp\left(\frac{j2\pi}{\lambda}(R(i) - R\_mid(i))\right)}{\sum_{i=1}^{N} \left(\frac{1}{R\_TX(i)} \times \frac{1}{R\_RX(i)}\right)^2} \tag{4.4}$$

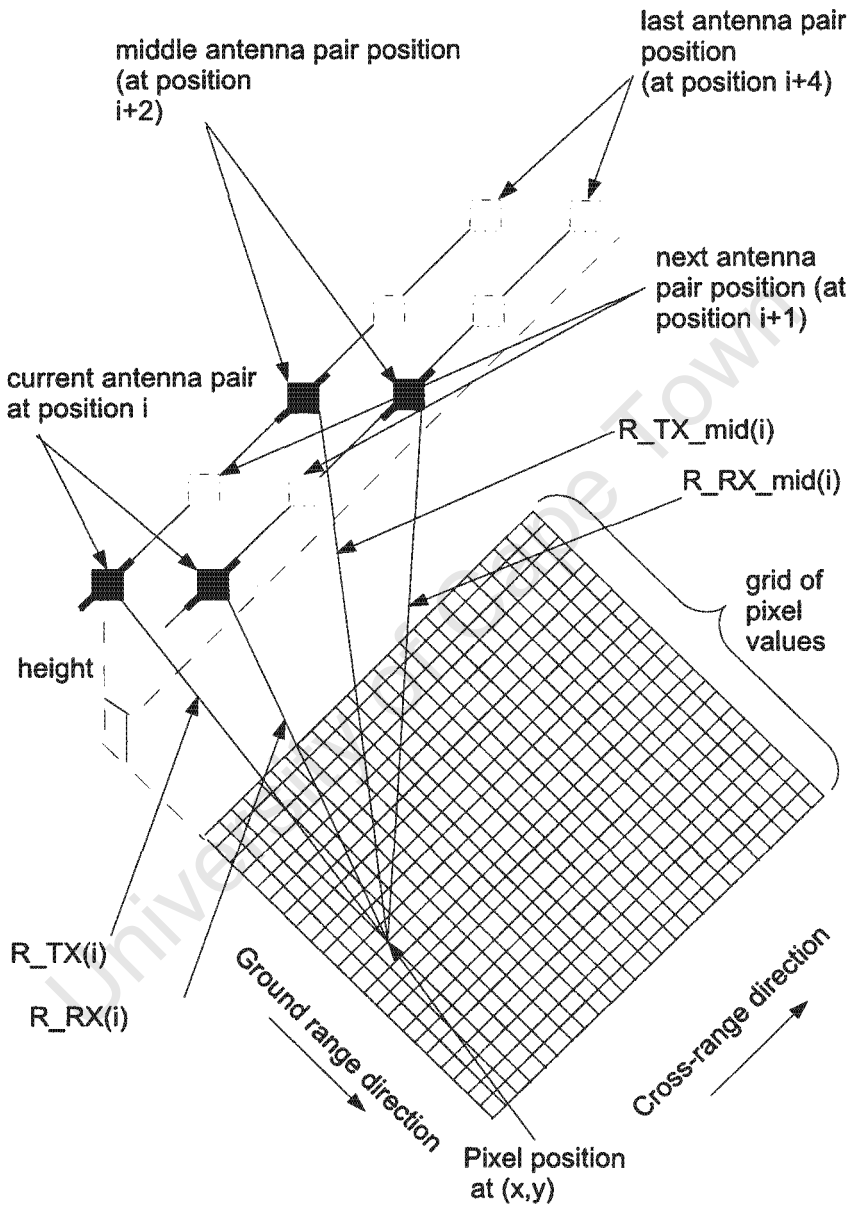

Figure 4.2: Illustration of parameters involved in beamforming

where $V_i(t(x,y))$ is a sample extracted (or interpolated) from the i^{th} range profile at time delay $t(x,y)$. The time delay $t(x,y)$ represents the two-way time delay from the pixel, i.e. transmitter to pixel and from pixel to receiver as a function of cross-range x and ground range y, calculated using the formula $t = 2R/c$. $V_i(t)$ represents the i^{th} antenna's sample extracted at time instant t. $R(i) - R\_mid(i)$ calculates the additional range to the point target from its position of closest approach. The reason for range compensation using this amount is in order to preserve the phase of the point target at its closest approach zero Doppler position for the purposes of interferometry. The factor $\sum_{i=1}^{N}\left(\frac{1}{R\_TX(i)} \times \frac{1}{R\_RX(i)}\right)^2$ in the denominator compensates for the range-dependent weakening of the echo of the transmitted signal and facilitates the formation of an image where the same point target at near and far range will have approximately the same brightness.

It is important to note that $V_{foc}(x,y)$ in this beamforming algorithm assumes a nominally flat scene.

4.2 Sonar interferogram formation

Each pixel of the first basebanded cross-range focussed image was multiplied with the complex conjugate of the corresponding pixel in the second image. The result was a complex interferogram. This process is described by the formula:

$$V\_int\,(x,y) \;=\; V\_1\,(x,y)\,.V\_2^{*}\,(x,y) \tag{4.5}$$

where $V\_int\,(x,y)$ represents the complex interferogram result. $V\_1\,(x,y)$ and $V\_2\,(x,y)$ represent the beamformed results of focussing of images recorded from the outputs of two different receiver antennas respectively.

4.3 Differences between standard synthetic aperture interferometry and the emulator interferometry beamforming algorithm

- **Size of beamforming array and resultant effect on resolution:** Standard synthetic apertures as produced in SAR algorithms involve a finer focussing beam that is a result of a very long synthesised aperture that "slides" past a point target and focusses it into zero Doppler co-ordinates. In contrast, the beamforming algorithm that was chosen for research purposes treats the imaging antennas as being part of a fixed array that focuses pixels relative to a centre beam that is swept across the focussing grid, with the best image resolution being perpendicular to the direction of motion of the mounted antennas.

- **Focussing grid location in space:** Typically interferograms are focussed in slant range. The beamforming algorithm focusses in ground range.

Chapter 5

Emulator Readings and Analysis

This chapter presents the results of taking readings using the emulator and analyses the results. Phase stability, range resolution and cross range resolution are first investigated. Scenes are then imaged using the emulator and the results are discussed.

5.1 Investigation into emulator properties

The phase stability of the emulator is first investigated, followed by an investigation into range and cross range resolutions of the system.

5.1.1 Phase stability

This section describes an investigation into phase stability of the emulator in air. Figure 5.1 shows the physical setup for recording repeated transmissions of pulses from a stationary transmitter to a stationary receiver. Phase stability was investigated by performing the following steps:

1. recording the signal that was transmitted from the transmitter (that was placed 1.53 m away from the receiver) for subsequent creation of an inverse filter,
2. and then waiting approximately a minute before subsequently placing the actively transmitting transmitter 1.60 m away from the receiver and recording.

The one minute delay was introduced in order to investigate the effect on phase a short time delay causes. The transmitter was moved 0.07 m from 1.53 m to 1.60 m from the receiver in order to investigate whether or not a typical Hanning window response would be observed despite the short offset. 257 transmissions of the transmitted signal over a 205 seconds period were subsequently recorded since 205 seconds is a slightly longer delay than the time required for recordings for the aperture to be recorded (approximately 180 seconds).

Figure 5.2 shows a magnitude plot of an ideal point target response that is created using the inverse filter. Notice that the shape of the downrange profile that was produced clearly looks like a Hanning response function.

The corresponding phase profile is shown in Figure 5.3. It is important to note the phase variation is small over the main lobe of the down range profile; this is a desirable property as it means that the created interferogram is less sensitive to registration errors. Since the phase over the main lobe of the down range profile experiences sufficiently small

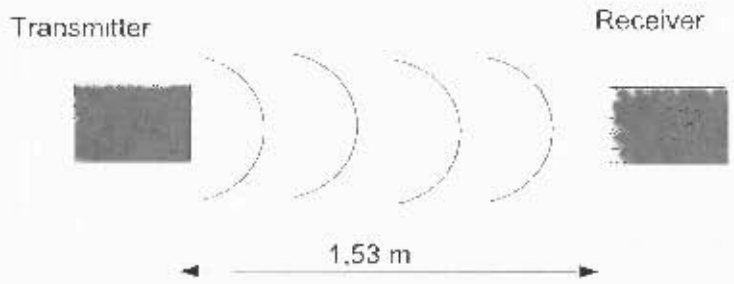

Figure 5.1: Transmitter to receiver physical setup used for recording signal that will be used to create an inverse filter

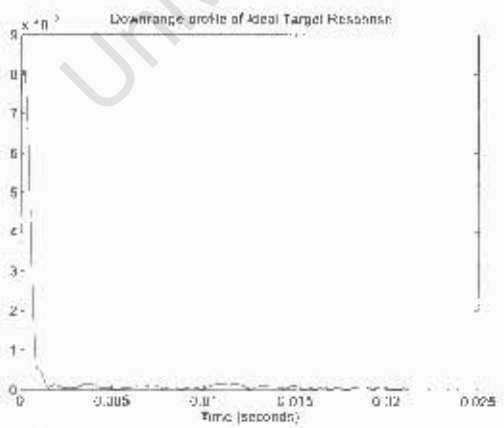

Figure 5.2: Magnitude of an ideal downrange profile created using the inverse filter

fluctuation, i.e. less than 0.125 of a cycle in a time period that is approximately the same time period that a 33.4 cm synthetic aperture data is recorded, coherent processing of the data is feasible.

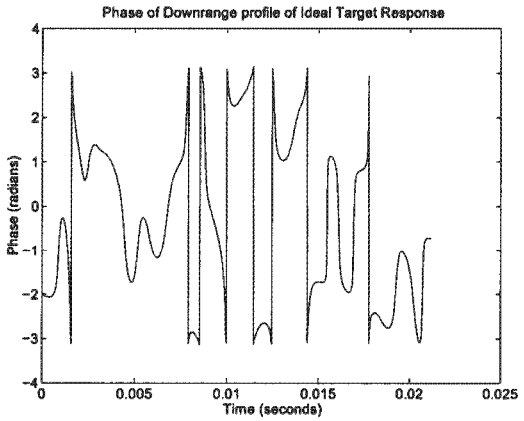

Figure 5.3: Phase of an ideal downrange profile created using the inverse filter

The recorded history of the transmitted signal was then basebanded and Hanning windowed in the slant range direction. The phase history of the range compressed peak of the main lobe is shown in Figure 5.4 while a histogram plot corresponding to Figure 5.4 is shown in Figure 5.5. The phase fluctuated by less than 0.125 of cycle, which is low enough to allow coherent aperture synthesis. The primary cause of the phase fluctuation is disturbance in the air.

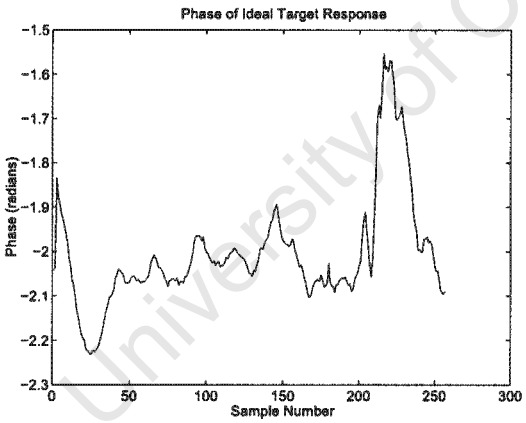

Figure 5.4: Phase history of range compressed peak of received signal at peak of main lobe

The histogram of phase history shows a tendency towards a central value.

5.1.2 Focussed Corner Reflector

The purpose of presenting a focussed corner reflector is to determine cross range and ground range resolutions for the emulator system. The imaging geometry and parameters are described in section 2.5. This geometry and its applicable parameters are relevant to the geometry illustrated in Figures 2.9 and 3.24. Four corner reflectors were placed on the corners of the scene that was to be imaged.

Ground range and cross range profiles of a focussed corner reflector are presented in this section (5.1.2). The corner reflector that is shown was extracted from the upper right

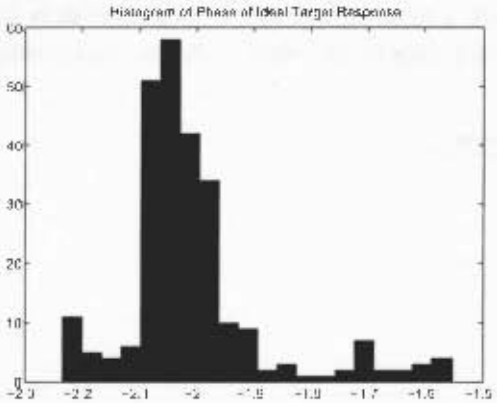

Figure 5.5: Histogram of phase history corresponding to phase history in Figure 5.4

corner of Figures 5.6 and 5.7. The orientation of the photo of Figure 5.6 corresponds to the orientation presented in the focussed images.

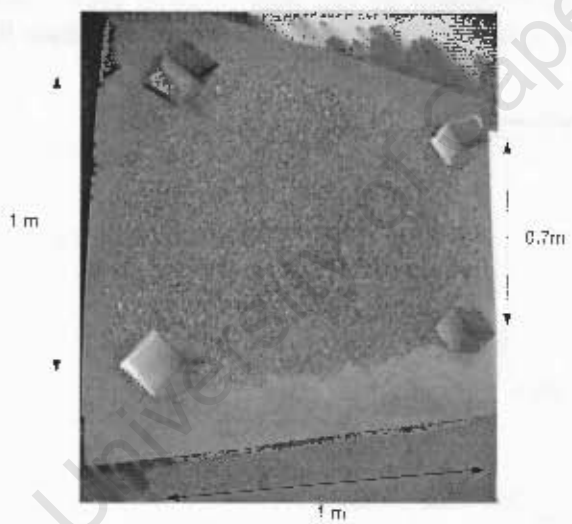

Figure 5.6: Scene with four cardboard corner reflectors oriented to match the presentation of results of focussing and interferogram formation

Figure 5.7 is 91 pixels in cross range and 131 pixels in ground range. Each pixel represents a coherent sum of distributed scatterers in a 0.01 m cross range by 0.01 m ground range cell. One of the four corner reflectors is not very clearly seen in the focussed image of Figure 5.7. A possible reason for this low amplitude is that this particular corner reflector was not oriented in such a way as to effectively reflect the transmitted chirp signal back in the direction of the receiver transducers. Figure 5.8 shows the magnitude of the focussed extracted corner reflector that is 21 pixels in cross range and 31 pixels in ground range.

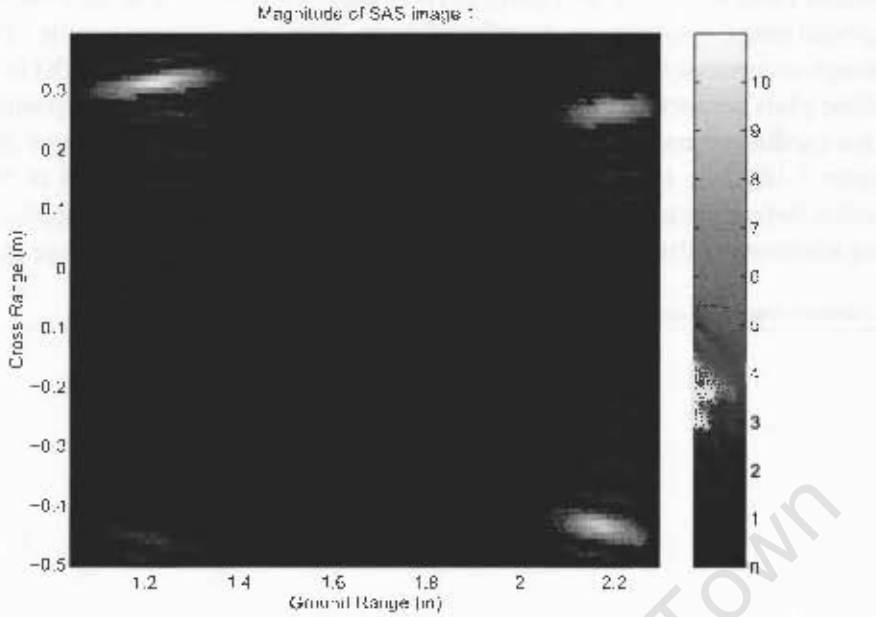

(a) Focussed magnitude image of scene from RX1

Figure 5.7: Magnitude of 4 corner reflectors (one with low amplitude)

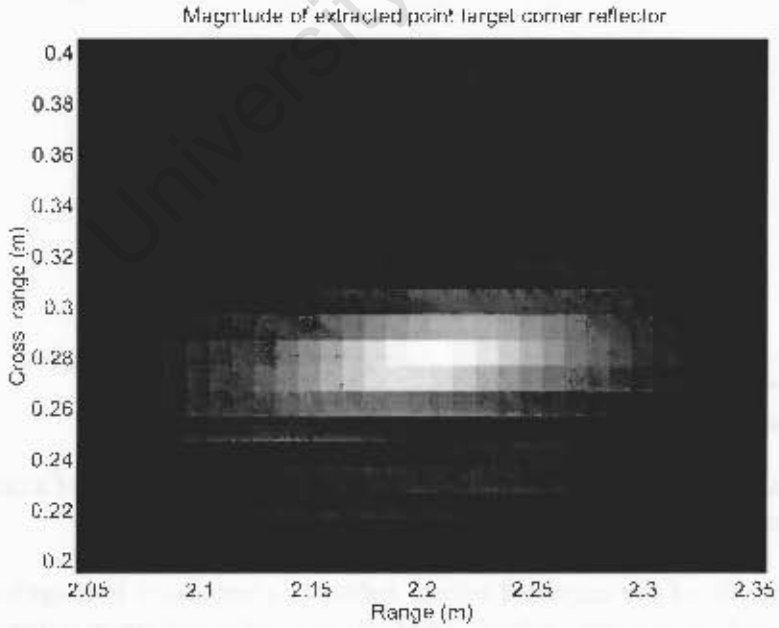

Figure 5.8: Magnitude of focussed extracted corner reflector

According to Figure 2.17, the expected 3 dB resolution (in slant range) for a chirp bandwidth of 2531 Hz is 7 cm with no windowing applied. The ground range to slant range 3 dB resolution ratio according to Figure 2.16 is approximately 1.3 at mid-swath. The expected ground range resolution is therefore 9.1 cm. The ground range profile of a range and cross range compressed corner reflector is shown in Figures 5.9(a) and (b) in magnitude and phase plots respectively. The 3 dB range resolution of the focussed ground range profile of the cardboard corner reflector was measured from the magnitude of the main lobe in Figure 5.10(a) as 10 cm after a Hanning window had been applied in the slant range direction before focussing in ground range onto a flat surface. The application of the Hanning window results in a broadening of the main lobe in the down-range direction.

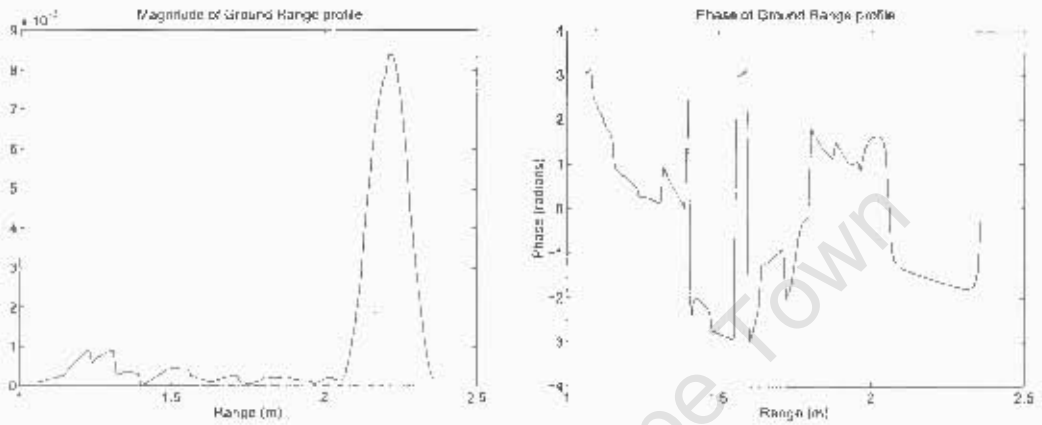

(a) Magnitude plot (b) Phase plot

Figure 5.9: Magnitude and phase plots of a ground range profile of a range and cross range compressed corner reflector

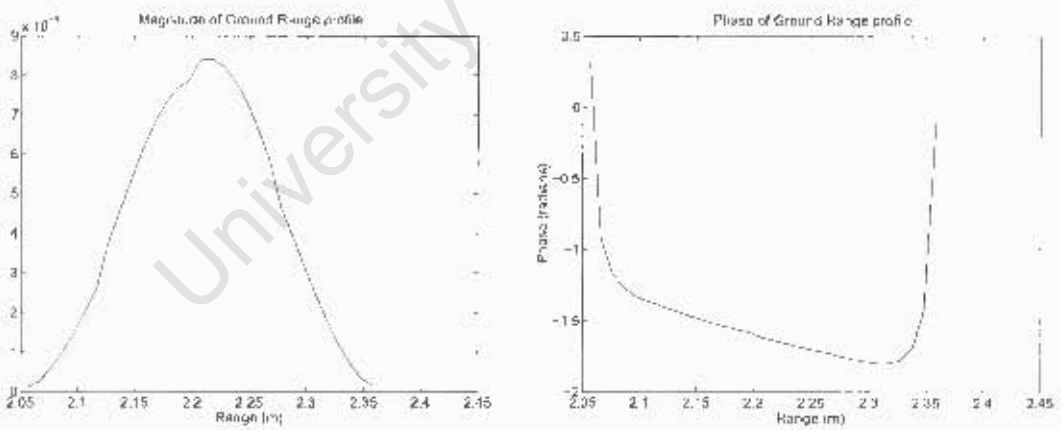

(a) Magnitude of main lobe (b) Phase of main lobe

Figure 5.10: Magnitude and phase of a main lobe of a ground range profile of a range and cross range compressed corner reflector

The cross range profile of the extracted corner reflector is presented in magnitude and phase plots in Figure 5.11. It is important to note that cross range resolution is displayed in co-ordinates of ground range and angle from boresight. The main lobe of the cross range profile of the extracted corner reflector is presented in a zoomed-in format for magnitude and phase in Figure 5.12. The corner reflector cross range profile over the main lobe is centred at approximately 7 degrees off the boresight. The length L of the synthesised

aperture along the boresight is 33.4 cm. The cross range resolution is a function of both range and angle. In the direction of the corner reflector, the effective synthesised aperture length D in the squint direction is calculated as follows:

$$D = L \times cos(\alpha) \tag{5.1}$$

where L is the length of the synthesed aperture that is formed when focussing using the boresight of the array, and α is the squint angle to the target.
Substituting values, gives

$$\begin{aligned} D &= 0.334 \times cos(7^o) \\ &= 0.3315\, m \end{aligned}$$

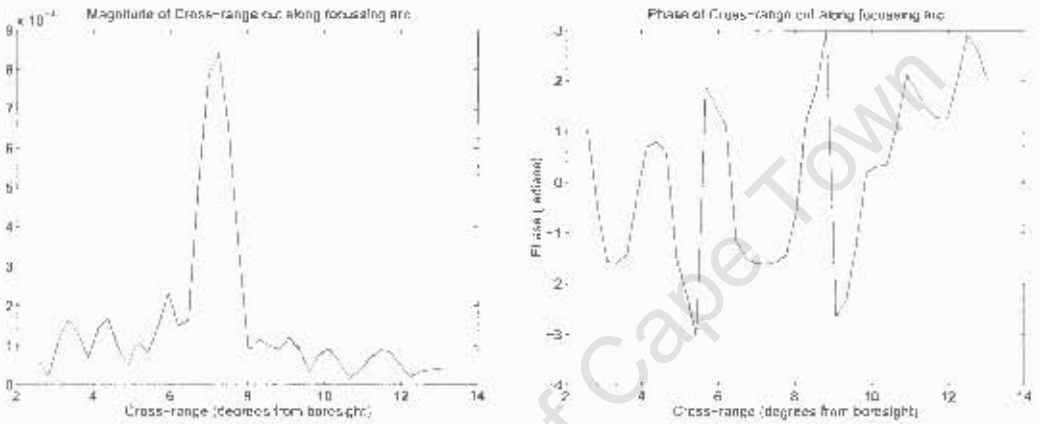

(a) Magnitude along cross-range cut (b) Phase along cross-range cut

Figure 5.11: Magnitude and phase of a cross range cut as a function of angle along a constant range arc of a range and cross range compressed corner reflector's main lobe

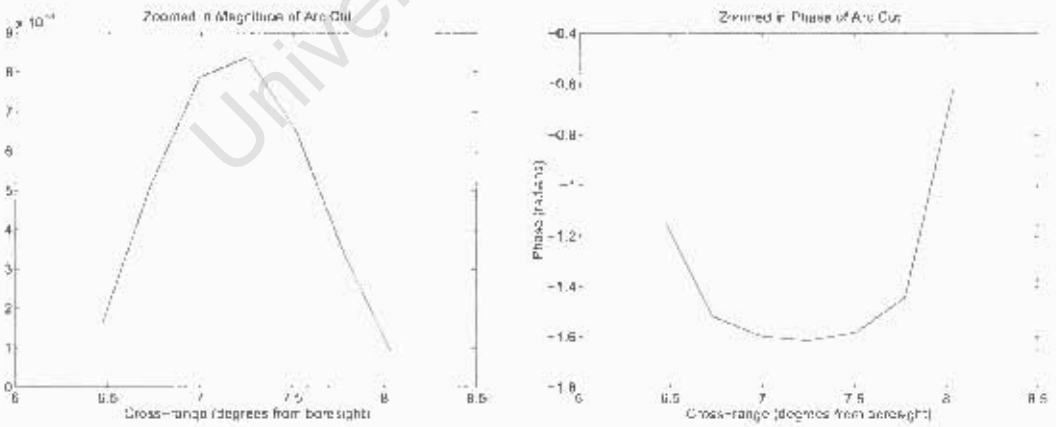

(a) Zoomed in magnitude (b) Zoomed-in phase

Figure 5.12: Zoomed in versions of a magnitude and phase of a cross range cut as a function of angle along a constant range arc of a range and cross range compressed corner reflector's main lobe

The corner reflector in the focussed image is centred at a value of ground range from the centre of the array to the target r_{centre} of 2.218 m. The expected size of the unwindowed

3 dB cross range resolution using angular resolution $d\theta$ and ground range from the centre of the array to the target r_{centre} is calculated using the following formula:

$$Expected\,cross\,range\,resolution\,along\,arc \;=\; r_{centre} \times (d\theta) \qquad (5.2)$$

The value of angular resolution $d\theta$ is calculated using equation 2.39:

$$\begin{aligned} d\theta &= \frac{\lambda}{2D} \\ &= \frac{0.0084}{2 \times 0.334 \times cos(7^o)} \\ &= 0.0127\,radians \end{aligned}$$

The expected cross range resolution in metres is

$$\begin{aligned} Expected\,cross\,range\,resolution\,along\,arc &= r_{centre} \times \frac{\lambda}{2D} \\ &= 2.218 \times \frac{0.0084}{2 \times 0.334 \times cos(7^o)} \\ &= 0.0281\,m \end{aligned}$$

The measured cross range resolution CR was slightly finer than this approximation. It was converted to cross range resolution along the constant ground range arc that is found by using the measured angular width of 0.5^o between the 3dB points of the main lobe shown in Figure 5.12. It was found to be 0.0202 m as shown in the following calculation that converts from angle to distance in cross range:

$$\begin{aligned} CR &= r_{centre} \times d\theta \\ &= 2.218 \times 0.5^o \\ &= 0.0202\,m \end{aligned}$$

5.2 SAR Interferometry Emulation Using Sonar

5.2.1 Beamforming using a distributed scatterer scene with four corner reflectors

The purpose of presenting four focussed corner reflectors is to demonstrate the ability of the emulator system to compress point target signatures in unprocessed data. The geometry and applicable parameters of this scene are as described in section 2.5 and illustrated in Figures 2.9 and 3.24. Four corner reflectors were placed on the corners of the scene that was to be imaged.

Signals received on receivers RX1 and RX2 with baseline 16 mm between them were used for analysis.

The photograph of the scene that was imaged can be seen alongside a focussed SAS image from RX1 in Figure 5.13. Note that the orientation of the photograph corresponds to the orientation of Figures 5.14, 5.15 and 5.16.

Figure 5.14 shows the two unfocussed images from antennas RX1 and RX2 that clearly look similar to one another, as was expected. Notice that the images contain signatures

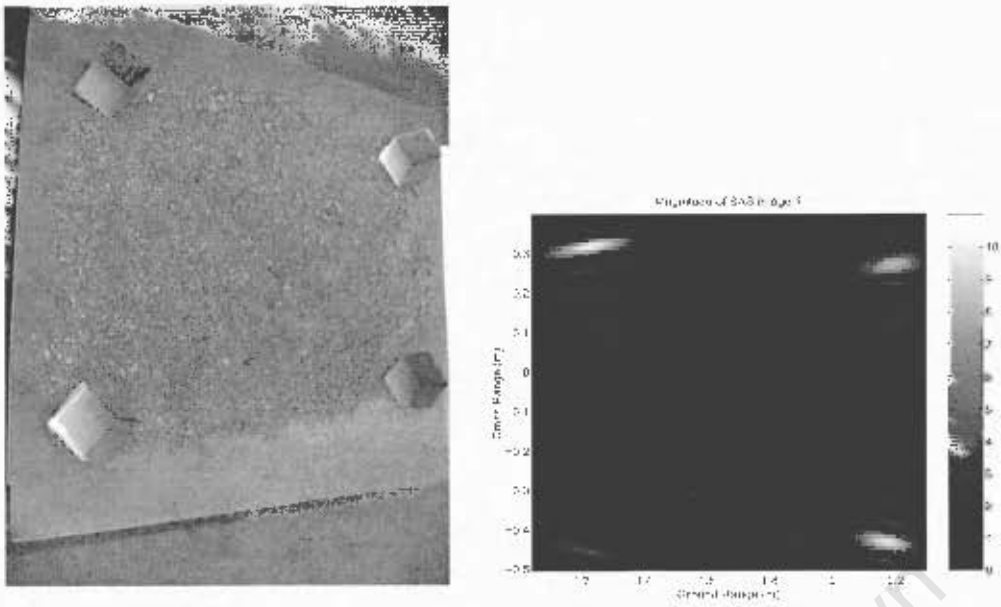

(a) Photograph of scene (b) Focussed magnitude image of scene from RX1

Figure 5.13: Photographed distributed scatterer stone scene with four cardboard corner reflectors placed alongside a magnitude plot of SAS image from antenna RX1

of the point targets. An interference pattern is visible resulting from constructive and destructive interference of echoes received from two corner reflectors at the same slant range. The frequency is higher for the closer pair of corner reflectors at (slant range $\approx$ 1.8 m) than the further pair at (slant range $\approx$ 2.55 m). This is because one of the corner reflectors at identical slant range from the closer pair in slant range did not return a strong echo to the receivers since it was not oriented towards the receivers as well as the other three corner reflectors were.

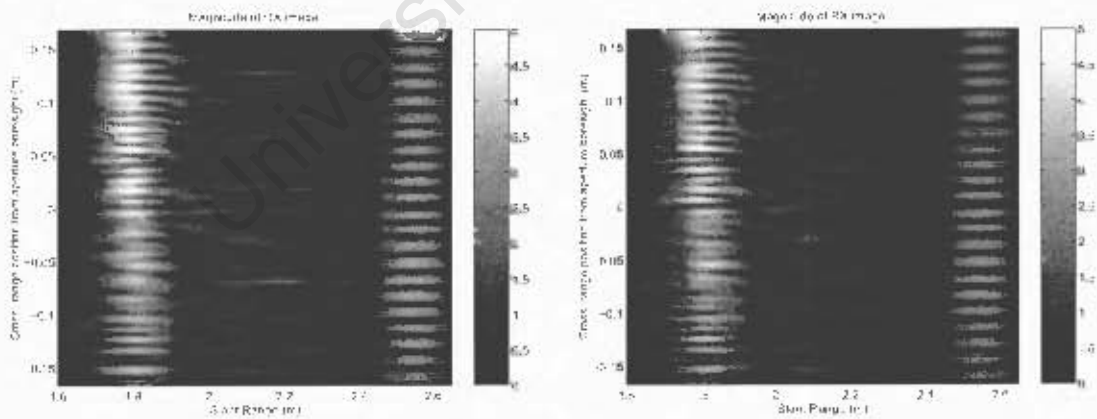

(a) Unfocussed image from RX1 (b) Unfocussed image from RX2

Figure 5.14: First Flat Stone Scene: Unfocussed images from antennas RX1 and RX2 respectively

Figure 5.15 shows the magnitudes of the SAS images from RX1 and RX2. Notice the similarity between these two images that were focussed in ground range. Take note that the complex SAS images are 91 pixels in cross range and 131 pixels in ground range. Each pixel represents a coherent sum of distributed scatterers in a 0.01 m cross range by 0.01 m ground range cell.

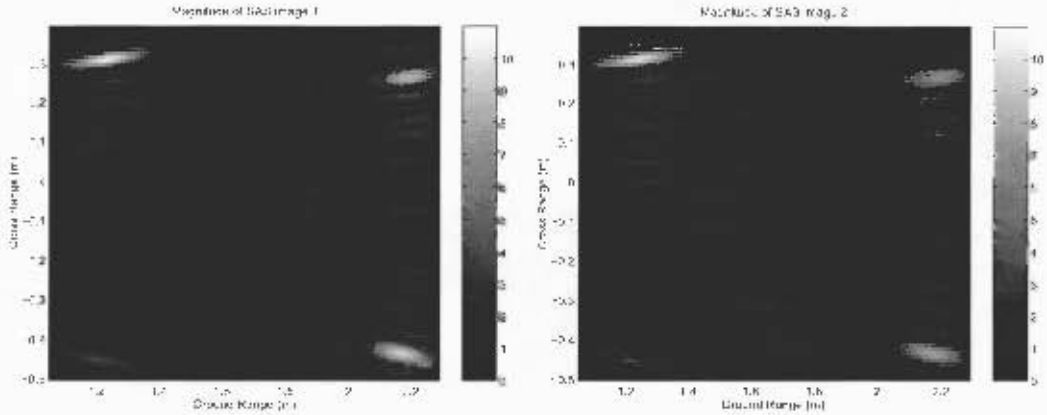

(a) Focussed image from RX1 (b) Focussed image from RX2

Figure 5.15: Magnitudes of SAS images from antennas RX1 and RX2 respectively

Figure 5.16 is a 3 dimensional plot of the magnitude of the SAS image from RX1 plotted on a grid representing cross range and ground range. Clearly, the focussing of different point corner reflectors on the corners of the desired area for imaging was successful, even though the one corner reflector had a low amplitude due to its orientation away from the receivers.

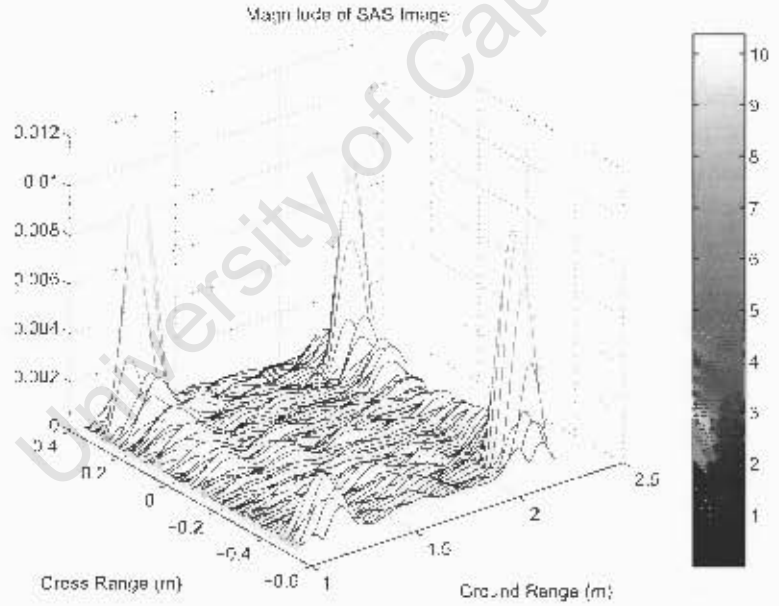

Figure 5.16: Mesh plot of magnitude of SAS image from antenna RX1

5.2.2 Interferograms of a distributed scatterer stone scene (Baselines 16 mm and 32 mm)

The geometry and applicable parameters of this scene are as described in section 2.5 and illustrated in Figures 2.9 and 3.24. The scene was set up by removing the four corner reflectors from the scene described in section 5.2.1.

The baselines between receivers that were used for interferometry were:

- 16 mm between RX1 and RX2, and
- 32 mm between RX1 and RX3.

The bottom transducer functioned as the transmitter while the three transducers above it functioned as receivers, as indicated in Figure 3.23. All transducers were placed one on top of the other. Each transducer had a diameter of 16 mm. The baselines between receivers that were used were 16 mm between RX1 and RX2 and 32 mm between RX1 and RX3. Signals received on receivers RX1 and RX2 with baseline 16 mm between them were used for interferogram formation. The recorded signal on RX3 was used in order to form an interferogram using the baseline of 32 mm between receivers RX1 and RX3.

A photo of the imaged scene can be seen in Figure 3.26. Notice in Figure 3.26 the scattered stones that are meant to emulate the distributed scatterer scene. The image recording process took approximately 3 minutes to complete.

Unfocussed magnitude images are presented in Figures 5.17 and 5.18. Notice the high degree of similarity between the different images.

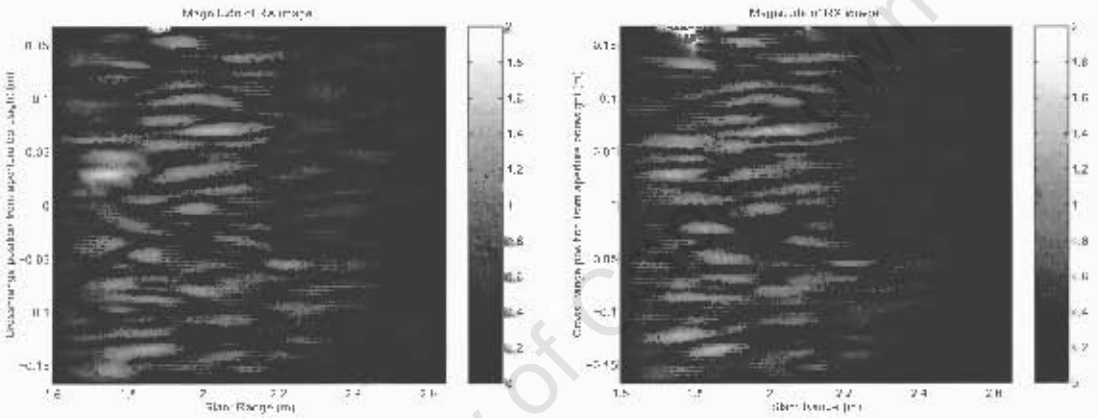

(a) Unfocussed image from RX1 (b) Unfocussed image from RX2

Figure 5.17: Distributed scatterer stone scene: Unfocussed magnitude images from antennas RX1 and RX2 respectively

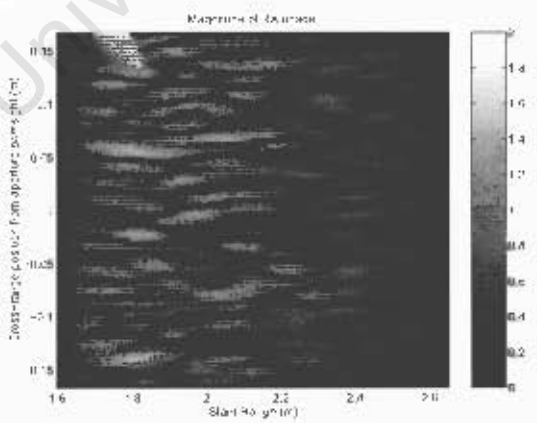

(a) Unfocussed image from RX3

Figure 5.18: Distributed scatterer stone scene: Unfocussed magnitude image from antenna RX3

High degrees of similarity between SAS images from the distributed scatterer stone scene can be observed in the focussed SAS images in Figures 5.19 and 5.20. Take note that

the complex SAS images, from which interferograms are formed, are 91 pixels in cross range and 101 pixels in ground range. Each pixel represents a coherent sum of distributed scatterers 0.01 m cross range by 0.01 m ground range cell.

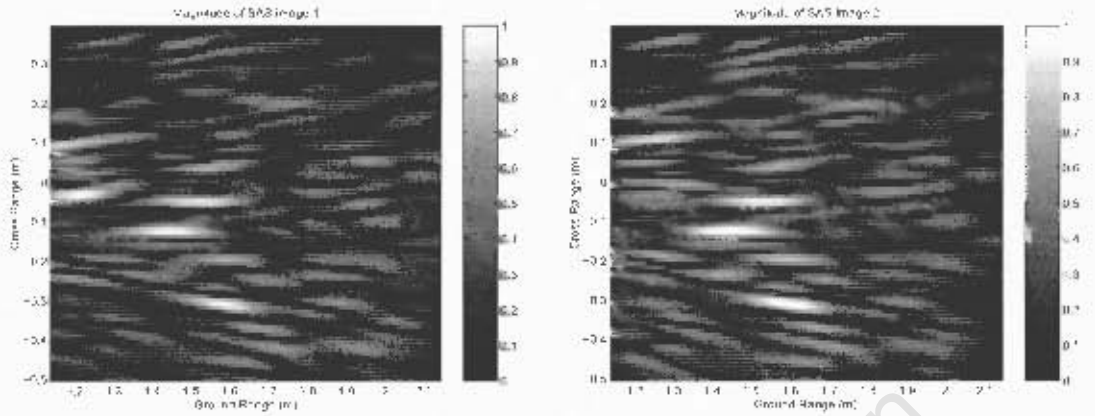

(a) Focussed image from RX1 (b) Focussed image from RX2

Figure 5.19: Distributed scatterer stone scene: Magnitudes of focussed SAS images from antennas RX1 and RX2 respectively

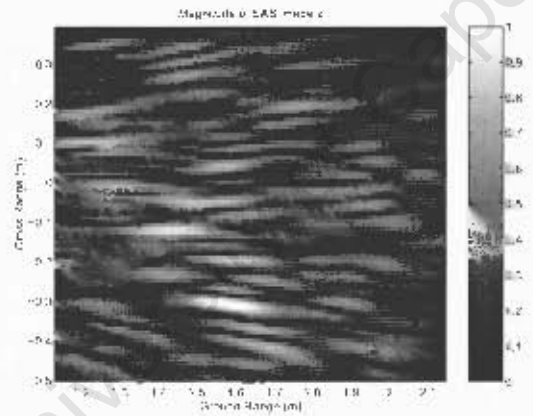

Figure 5.20: Distributed scatterer stone scene: Magnitude of the focussed SAS image from antenna RX3

Magnitudes and phase plots of interferograms formed using (RX1 and RX2 with baseline 16 mm) and (RX1 and RX3 with baseline 32 mm) are presented in Figures 5.21 and 5.22.

Unwrapped and smoothed complex interferograms are presented in Figure 5.23. The scenes were smoothed by using a 4-by-4 independent resolution cells averaging window for minimising the effect of noise on the interferogram. The window size was 40 pixels in ground range and 10 pixels in cross range.

A range profile along the boresight of the array (i.e. at cross range position of 0 m) is presented showing interferometric phases between (RX1 and RX2 with baseline 16 mm) and (RX1 and RX3 with baseline 32 mm) in Figure 5.24. The plot shows that the 32 mm baseline between RX1 and RX3 results in a phase slope that is, as predicted, approximately twice the slope of the phase slope for the (RX1 and RX2 with baseline 16 mm) case.

Figure 5.25 shows plots of the simulated phase calculated according to Equation 2.20 using ground range spacing identical to that of SAS images, as well as measured phases

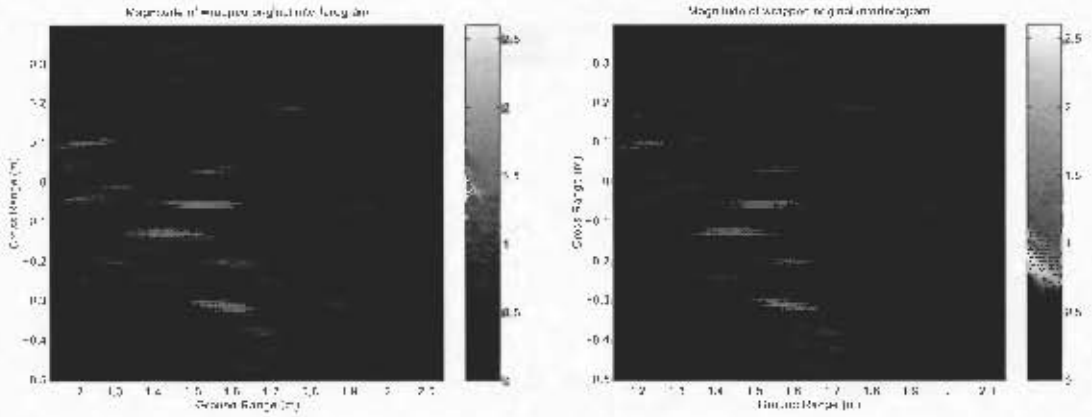

(a) Magnitude of interferogram from RX1 and RX2 (b) Magnitude of interferogram from RX1 and RX3

Figure 5.21: Distributed scatterer stone scene: Magnitudes of the unsmoothed complex interferograms (RX1 and RX2 with baseline 16 mm) and (RX1 and RX3 with 32 mm baseline)

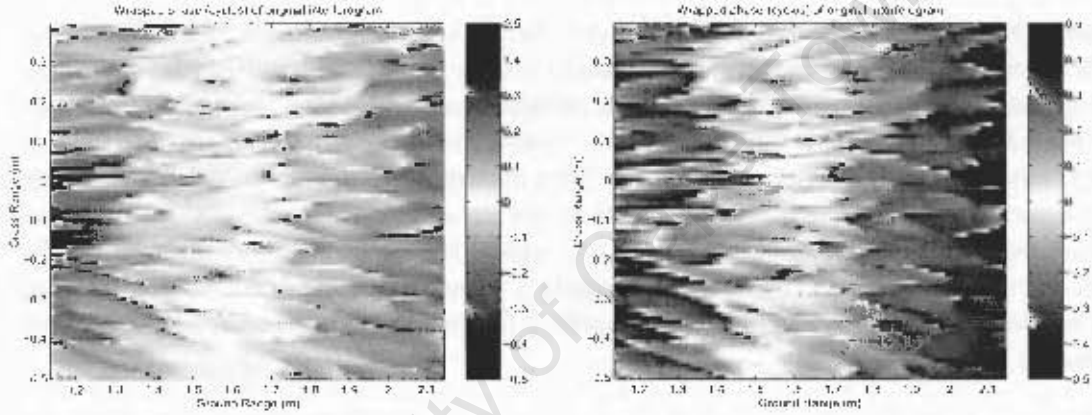

(a) Interferogram from images from RX1 and RX2 (b) Interferogram from images from RX1 and RX3

Figure 5.22: Distributed scatterer stone scene: Phase plots of the unsmoothed complex interferograms (RX1 and RX2 with baseline 16 mm) and (RX1 and RX3 with baseline 32 mm)

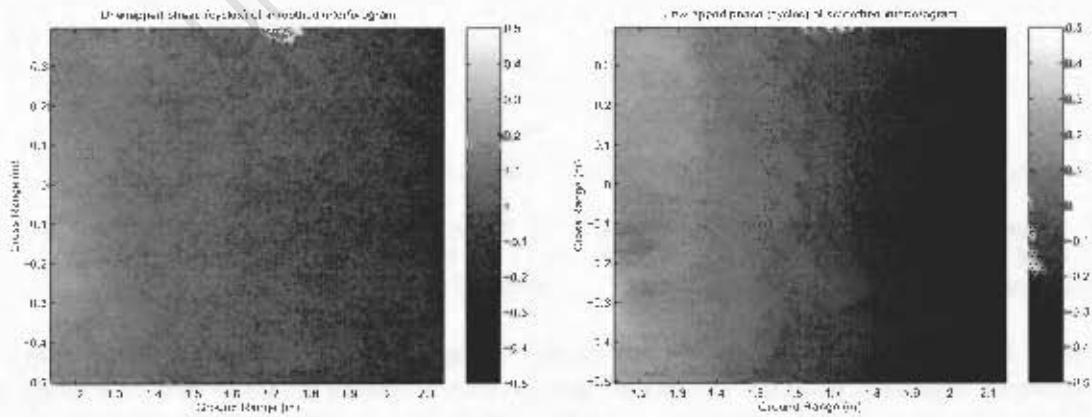

(a) Smoothed interferogram using RX1 and RX2 (b) Smoothed interferogram using RX1 and RX3

Figure 5.23: Distributed scatterer stone scene: Unwrapped smoothed complex interferograms (RX1 and RX2 with baseline 16 mm) and (RX1 and RX3 with baseline 32 mm) obtained using a 4-by-4 independent resolution cells smoothing window

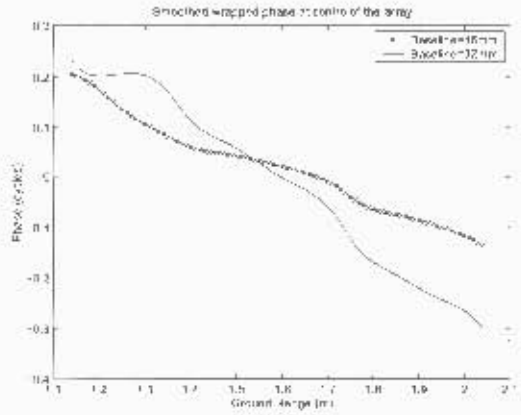

Figure 5.24: Distributed scatterer stone scene: Range profile along boresight of array comparing simulated phases with smoothed (4-by-4 independent resolution cells averaging window) interferometric phases obtained along boresight for interferograms made using (RX1 and RX2 with baseline 16 mm) and (RX1 and RX3 with baseline 32 mm)

using (RX1 and RX2 with 16 mm baseline) and (RX1 and RX3 with 32 mm baseline). Simulations seem to disagree with measured interferograms. The differences in phase slope are most prominent. The scene was imaged again using identical conditions. This repeated data recording is referred to as the "second measurement" as opposed to the first data recording which is referred to as the "first measurement". The second measurement was performed in order to check whether or not the difference in phase slope measurement from the expected simulated result is a typical feature of the emulator system. The second measurement was made approximately 3 minutes after the first measurement was completed. The time to complete data recording for the second measurement was approximately 3 minutes.

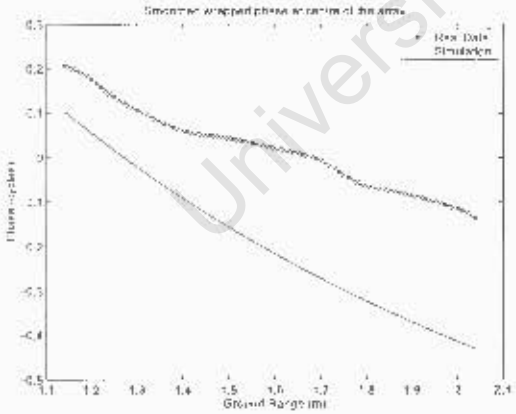

(a) Range profile of interferometric phase using RX1 and RX2 compared to its simulated interferometric phase

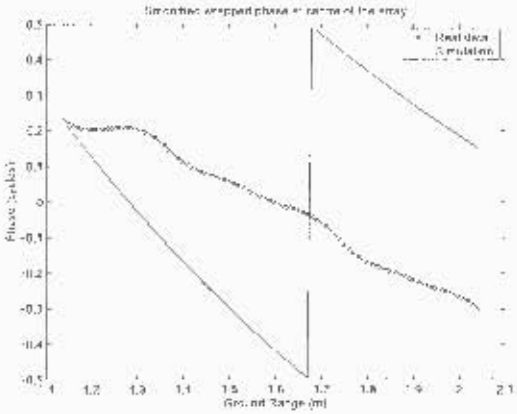

(b) Range profile of interferometric phase using RX1 and RX3 compared to its simulated interferometric phase

Figure 5.25: Distributed scatterer stone scene: Range profile along boresight of array comparing simulated phases with smooth interferometric phases obtained along boresight for interferograms made using (RX1 and RX2 with baseline 16 mm) and (RX1 and RX3 with baseline 32 mm)

Analysis of coherence and repeatability of synthetic aperture recordings

The coherence image for the first measurement for (RX1 and RX2 with baseline 16 mm) was generally above 0.9, while slightly lower coherence can be seen in the coherence image for (RX1 and RX3 with baseline 32 mm). This was still generally above 0.8. The expected coherence at mid-swath at 1.75 m in ground-range for the imaged scene is 0.9 for a 16 mm baseline and 0.81 for a 32 mm baseline according to Figure 2.10. The coherence images for the first measurement were plotted in Figure 5.26.

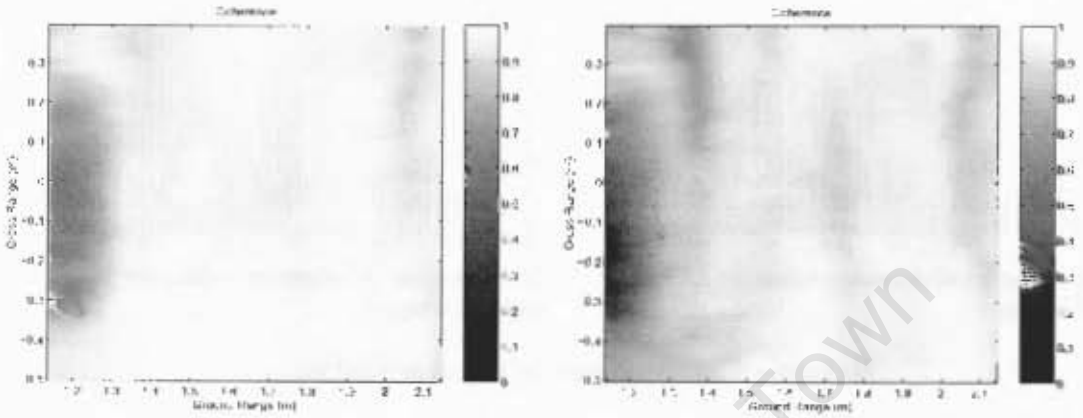

(a) Coherence for images from RX1 and RX2

(b) Coherence for images from RX1 and RX3

Figure 5.26: Distributed scatterer stone scene: Coherence images for (RX1 and RX2) and (RX1 and RX3) respectively

Figure 5.27 shows coherence images of the second measurement. These images show that coherence remains acceptable for the second measurement of the imaged scene as in the case of the first measurement of the scene. Notice that the coherences of the first and second measurements look identical. This implies repeatability of imaging of a scene as a result of stability of the coherence images.

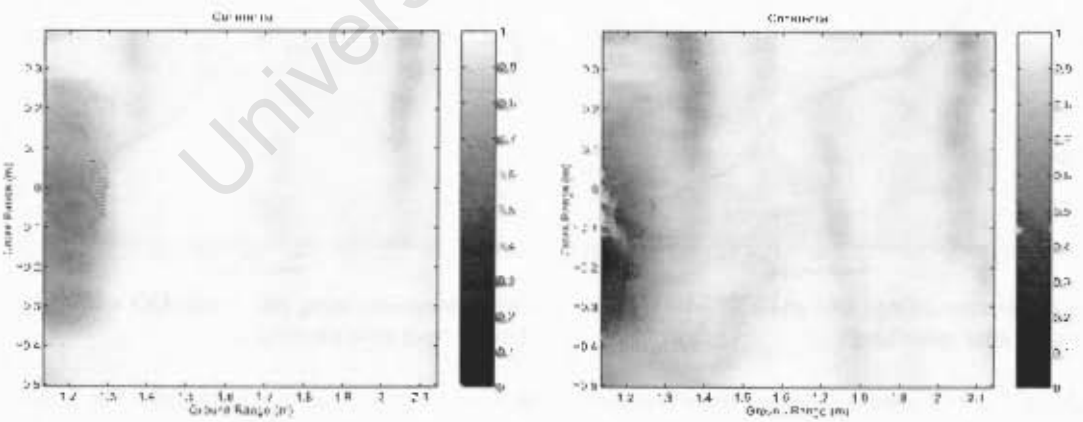

(a) Coherence image using RX1 and RX2 with 16 mm baseline

(b) Coherence image using RX1 and RX3 with 32 mm baseline

Figure 5.27: Coherence images for second measurement using the distributed scatterer stone scene of the first measurement: (RX1 and RX2 with baseline 16 mm) and (RX1 and RX3 with baseline 32 mm) respectively

Figures 5.28(a) and (b) show histograms from the first recording of coherence values for the region defined by cross range values varying from 0.08 m to 0.58 m and ground-range

values varying from 1.34 m to 1.84 m for the pairs (RX1 and RX2 with baseline 16 mm) and (RX1 and RX3 with baseline 32 mm) respectively. Take note that Figures 5.28(a) and (b) have different spans. As seen from these figures, a longer baseline results in lower incidences of high coherence.

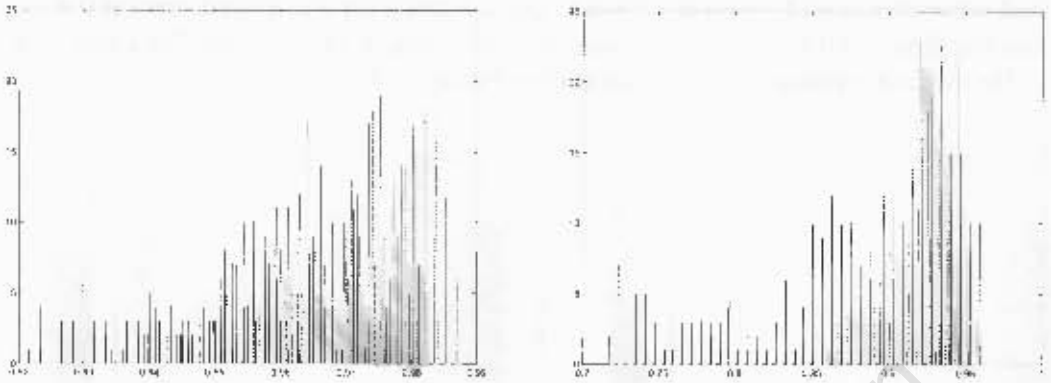

(a) Histogram of coherence values for RX1 and RX2 images

(b) Histogram of coherence values for RX1 and RX3 images

Figure 5.28: Histogram of coherence values

Figures 5.29(a) and 5.29(b) depict the smoothened boresight interferometric profiles (at cross range = 0 m) for 16 mm and 32 mm baselines from the first measurement. Comparisons between interferometric phases during the two passes over the distributed scatterer stone scene are shown to remain almost identical. It therefore seems that the deviation of measured phase from expected phase is a feature of the emulator system and remains a constant factor.

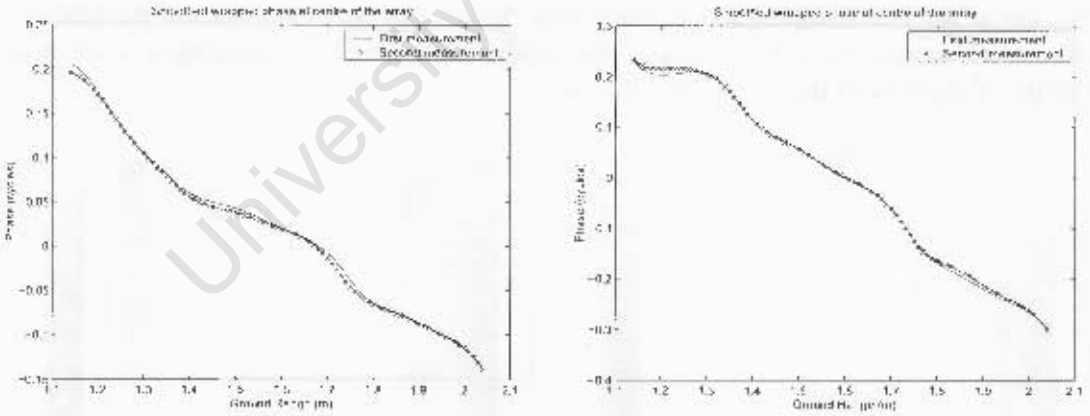

(a) Comparison using (RX1 and RX2 with baseline 16 mm) after smoothing

(b) Comparison using (RX1 and RX3 with baseline 32 mm) after smoothing

Figure 5.29: Comparison of interferometric phases obtained along boresight for interferograms taken during two recordings of the distributed scatterer stone scene using (a) (RX1 and RX2 with baseline 16 mm) and (b) (RX1 and RX3 with baseline 32 mm) after smoothing using a 4-by-4 independent resolution cell window

5.2.3 Distributed scatterer stone scene with step (Baselines 16 mm and 32 mm)

The purpose of this measurement is to establish the effect of adding a step to the scene by comparing the phase from a scene with a step to a scene that does not have a step. The physical setup and geometry of the distributed scatterer stone scene as described in 5.2.2 was left the same except for the addition of a step by adding three 72 mm high boxes to the scene on top of which stones were placed.

The geometry and applicable parameters of this scene are as described in section 2.5, and illustrated in Figures 2.9 and 3.24. The scene was set up by placing the previously mentioned three 72 mm high boxes onto the scene that was used in section 5.2.2.

The baselines between receivers that were used for interferometry were:

- 16 mm between RX1 and RX2, and
- 32 mm between RX1 and RX3.

The bottom transducer functioned as the transmitter while the three transducers above it functioned as receivers, as indicated in Figure 3.23. All transducers were placed one on top of the other. Each transducer had a diameter of 16 mm. The baselines between receivers that were used were 16 mm between RX1 and RX2 and 32 mm between RX1 and RX3. Signals received on receivers RX1 and RX2 with baseline 16 mm between them were used for interferogram formation. The recorded signal on RX3 was also used in order to form an interferogram using the baseline of 32 mm between receivers RX1 and RX3. A 72 mm high step was introduced into the part of the scene furthest away from the imaging transducers in ground range. This was achieved by the placement of 72 mm high cardboard boxes on top of the distributed scatterer stone scene on the cardboard that in turn had been placed onto the mobile platform. Stones were then placed on top of the boxes. The step was located at approximately 2 m in slant range. The image recording process took approximately 3 minutes to complete. The scene that was imaged is shown in Figure 5.30.

Figures 5.30 and 5.31 show two views of the scene with the 72 mm step that was imaged.

Figure 5.31 shows a profile of the distributed scatterer stone scene with the 72 mm step.

Figures 5.32 and 5.33 show data that is uncompressed (unfocussed) in cross range for the distributed scatterer stone scene with the 72 mm step. The step is located at approximately 2 m in slant range.

Figures 5.34 and 5.35 show the magnitudes of the focussed data corresponding to the aforementioned unprocessed data. Take note that the complex SAS images, from which interferograms are formed, are 91 pixels in cross range and 101 pixels in ground range. Each pixel represents a coherent sum of distributed scatterers in a 0.01 m cross range by 0.01 m ground range cell. The similarity between the different images is clear.

Figure 5.36 shows the magnitudes of the interferograms that were formed using the beam-forming algorithm. Both the magnitudes of the interferograms show a disturbance in cross range at 1.8 m in ground range. This would be caused by the perpendicular slope produced by the placement of the cardboard boxes on the stone scene. Strong returns from the boxes were expected and were subsequently recorded.

Figure 5.37 shows the phase plots of the complex interferograms that were produced. As with the magnitude images in Figure 5.36, a definite change in phase is noticed at 1.8 m in ground range.

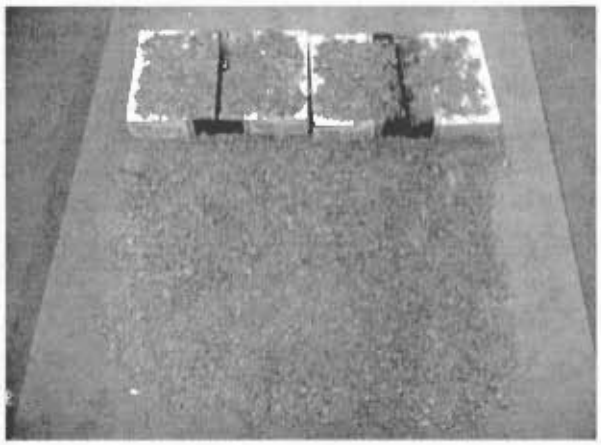

Figure 5.30: Distributed scatterer stone scene with 72 mm step as seen from the emulator track

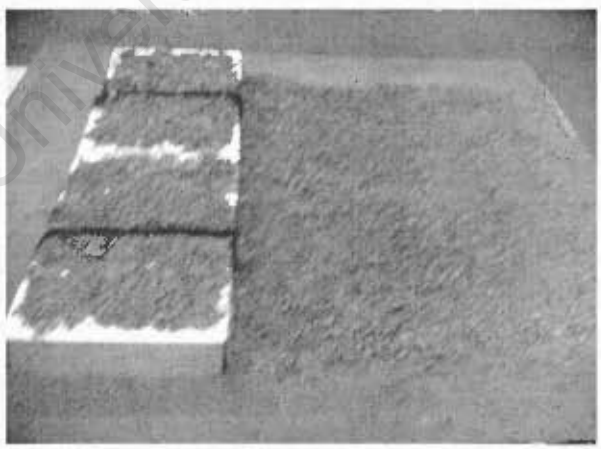

Figure 5.31: Profile of distributed scatterer stone scene with 72 mm step as seen from the left hand side of the scene when looking at the scene from behind the emulator track

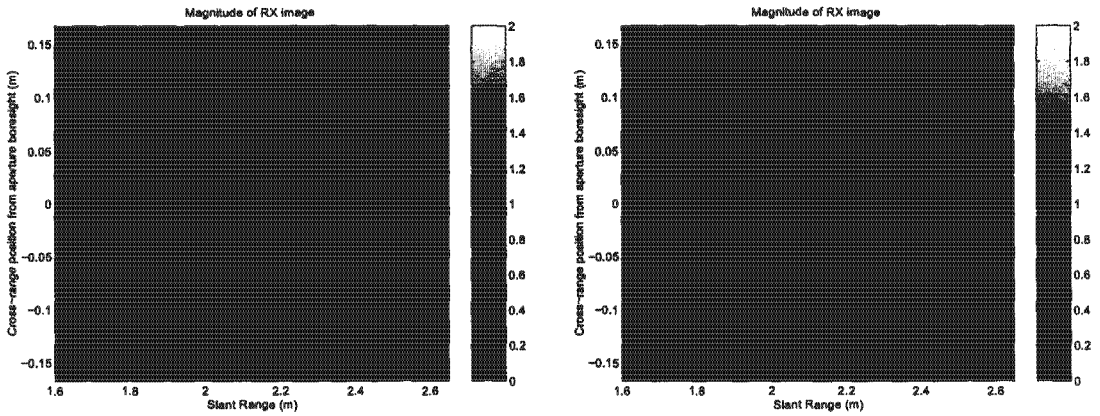

(a) Unfocussed image from RX1 (b) Unfocussed image from RX2

Figure 5.32: Distributed scatterer stone scene with 72 mm step: images from antennas RX1 and RX2 respectively

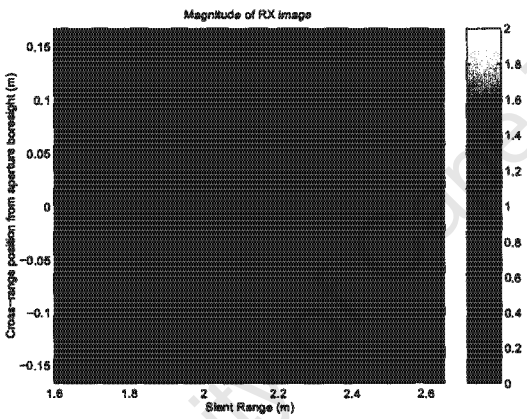

(a) Unfocussed image from RX3

Figure 5.33: Distributed scatterer stone scene with 72 mm step: Unfocussed image from antenna RX3

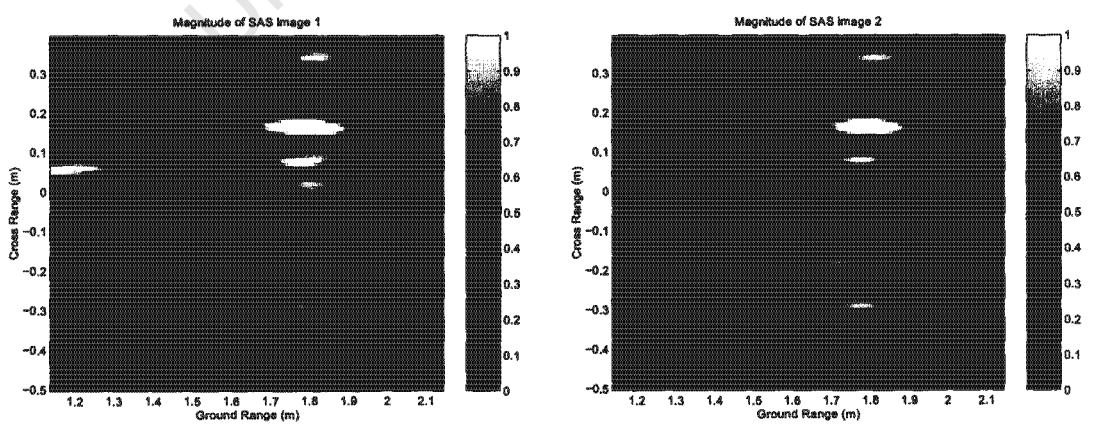

(a) Focussed image from RX1 (b) Focussed image from RX2

Figure 5.34: Distributed scatterer stone scene with 72 mm step: Magnitudes of SAS images from antennas RX1 and RX2 respectively

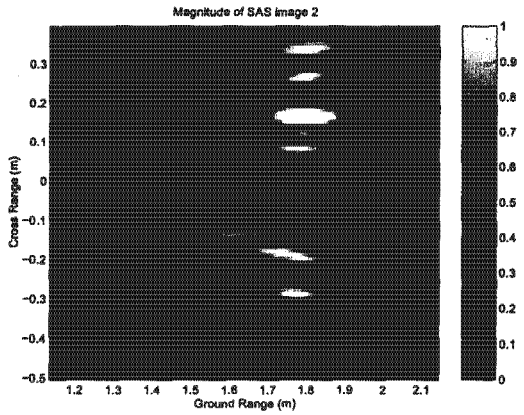

(a) Focussed image from RX3

Figure 5.35: Distributed scatterer stone scene with 72 mm step: Magnitude of the SAS image from RX3

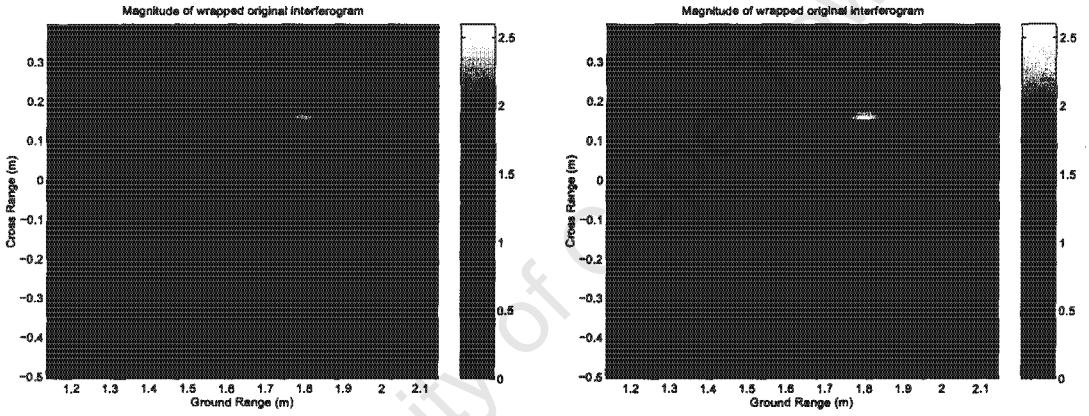

(a) Magnitude of interferogram from RX1 and RX2 (b) Magnitude of interferogram from RX1 and RX3

Figure 5.36: Distributed scatterer stone scene with 72 mm step: Magnitudes of the complex interferograms (RX1 and RX2 with 16 mm baseline) and (RX1 and RX3 with 32 mm baseline)

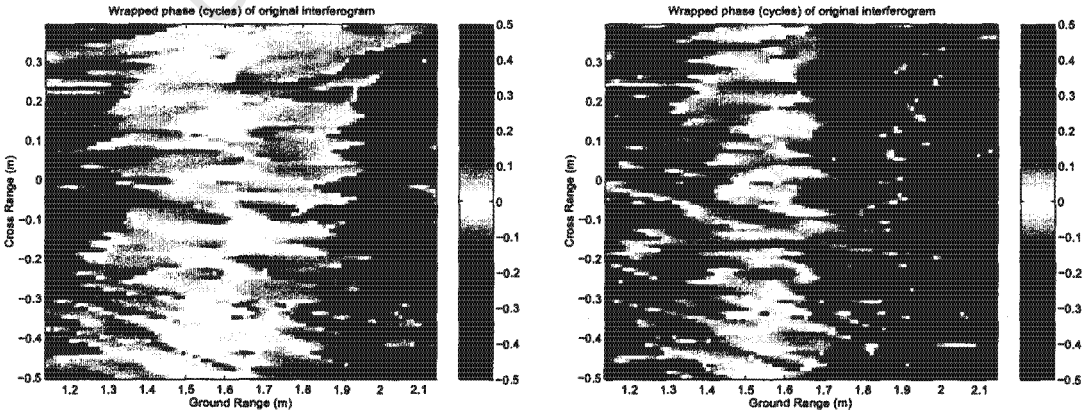

(a) Phase of interferogram from RX1 and RX2 (b) Phase of interferogram from RX1 and RX3

Figure 5.37: Distributed scatterer stone scene with 72 mm step: Phase plots of the complex interferograms (RX1 and RX2 with 16 mm baseline) and (RX1 and RX3 with 32 mm baseline)

5.2.3 Distributed scatterer stone scene with step (Baselines 16 mm and 32 mm)

The purpose of this measurement is to establish the effect of adding a step to the scene by comparing the phase from a scene with a step to a scene that does not have a step. The physical setup and geometry of the distributed scatterer stone scene as described in 5.2.2 was left the same except for the addition of a step by adding three 72 mm high boxes to the scene on top of which stones were placed.

The geometry and applicable parameters of this scene are as described in section 2.5, and illustrated in Figures 2.9 and 3.24. The scene was set up by placing the previously mentioned three 72 mm high boxes onto the scene that was used in section 5.2.2.

The baselines between receivers that were used for interferometry were:

- 16 mm between RX1 and RX2, and
- 32 mm between RX1 and RX3.

The bottom transducer functioned as the transmitter while the three transducers above it functioned as receivers, as indicated in Figure 3.23. All transducers were placed one on top of the other. Each transducer had a diameter of 16 mm. The baselines between receivers that were used were 16 mm between RX1 and RX2 and 32 mm between RX1 and RX3. Signals received on receivers RX1 and RX2 with baseline 16 mm between them were used for interferogram formation. The recorded signal on RX3 was also used in order to form an interferogram using the baseline of 32 mm between receivers RX1 and RX3. A 72 mm high step was introduced into the part of the scene furthest away from the imaging transducers in ground range. This was achieved by the placement of 72 mm high cardboard boxes on top of the distributed scatterer stone scene on the cardboard that in turn had been placed onto the mobile platform. Stones were then placed on top of the boxes. The step was located at approximately 2 m in slant range. The image recording process took approximately 3 minutes to complete. The scene that was imaged is shown in Figure 5.30.

Figures 5.30 and 5.31 show two views of the scene with the 72 mm step that was imaged.

Figure 5.31 shows a profile of the distributed scatterer stone scene with the 72 mm step.

Figures 5.32 and 5.33 show data that is uncompressed (unfocussed) in cross range for the distributed scatterer stone scene with the 72 mm step. The step is located at approximately 2 m in slant range.

Figures 5.34 and 5.35 show the magnitudes of the focussed data corresponding to the aforementioned unprocessed data. Take note that the complex SAS images, from which interferograms are formed, are 91 pixels in cross range and 101 pixels in ground range. Each pixel represents a coherent sum of distributed scatterers in a 0.01 m cross range by 0.01 m ground range cell. The similarity between the different images is clear.

Figure 5.36 shows the magnitudes of the interferograms that were formed using the beamforming algorithm. Both the magnitudes of the interferograms show a disturbance in cross range at 1.8 m in ground range. This would be caused by the perpendicular slope produced by the placement of the cardboard boxes on the stone scene. Strong returns from the boxes were expected and were subsequently recorded.

Figure 5.37 shows the phase plots of the complex interferograms that were produced. As with the magnitude images in Figure 5.36, a definite change in phase is noticed at 1.8 m in ground range.

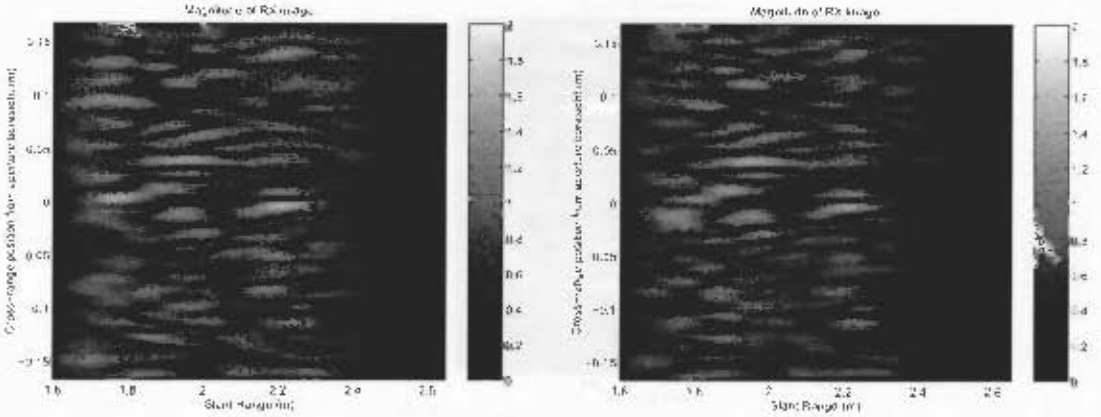

(a) Unfocussed image from RX1 (b) Unfocussed image from RX2

Figure 5.32: Distributed scatterer stone scene with 72 mm step: images from antennas RX1 and RX2 respectively

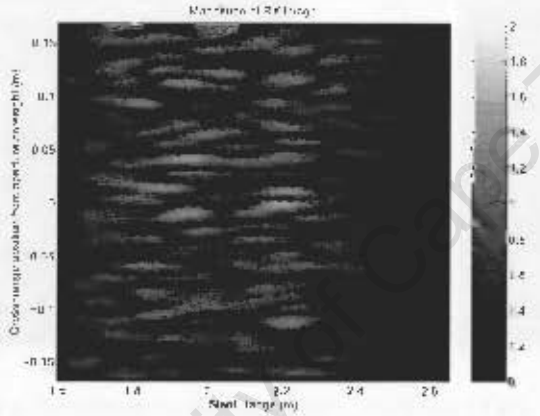

(a) Unfocussed image from RX3

Figure 5.33: Distributed scatterer stone scene with 72 mm step: Unfocussed image from antenna RX3

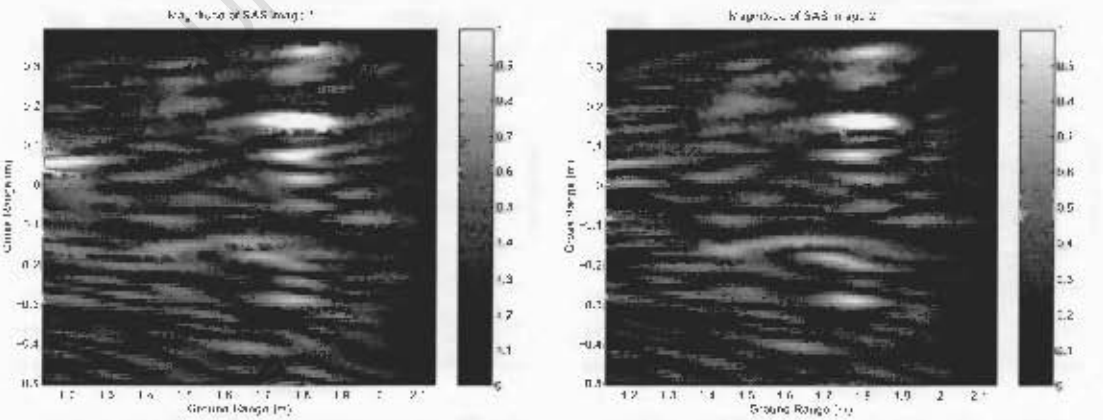

(a) Focussed image from RX1 (b) Focussed image from RX2

Figure 5.34: Distributed scatterer stone scene with 72 mm step: Magnitudes of SAS images from antennas RX1 and RX2 respectively

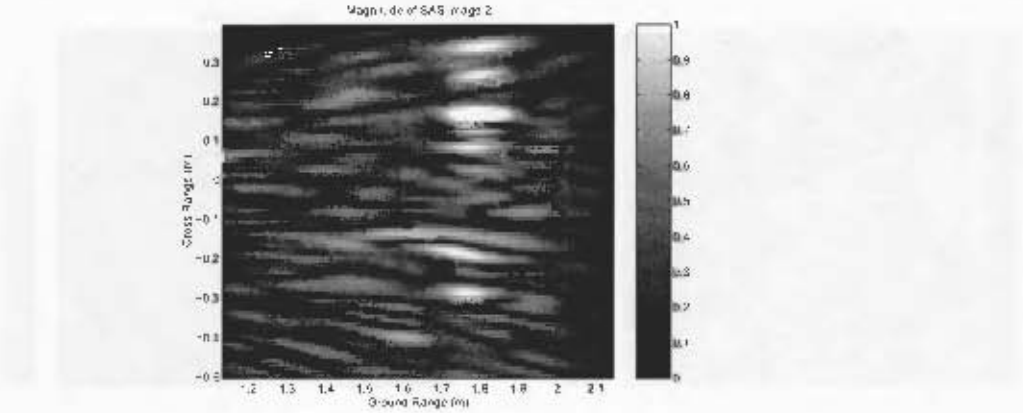

(a) Focussed image from RX3

Figure 5.35: Distributed scatterer stone scene with 72 mm step: Magnitude of the SAS image from RX3

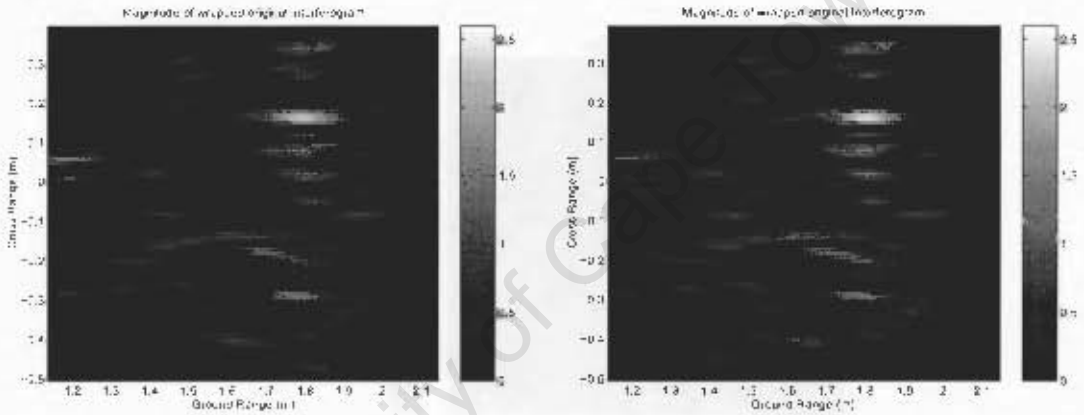

(a) Magnitude of interferogram from RX1 and RX2 (b) Magnitude of interferogram from RX1 and RX3

Figure 5.36: Distributed scatterer stone scene with 72 mm step: Magnitudes of the complex interferograms (RX1 and RX2 with 16 mm baseline) and (RX1 and RX3 with 32 mm baseline)

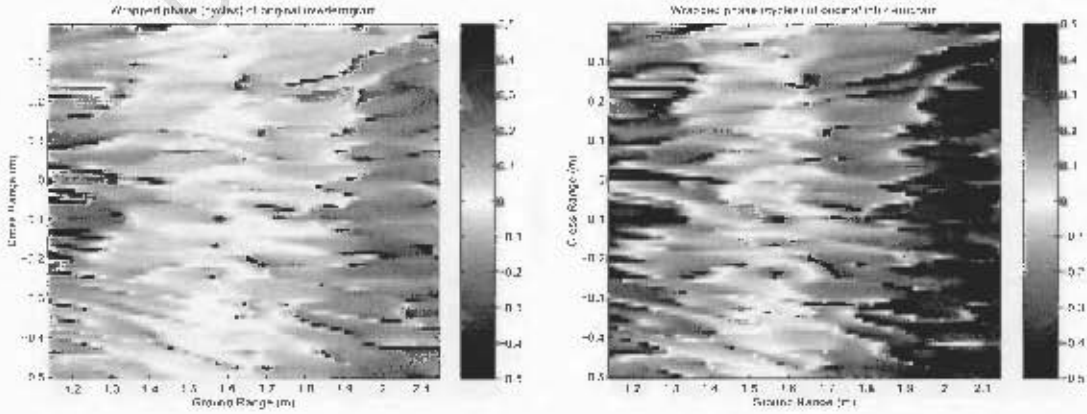

(a) Phase of interferogram from RX1 and RX2 (b) Phase of interferogram from RX1 and RX3

Figure 5.37: Distributed scatterer stone scene with 72 mm step: Phase plots of the complex interferograms (RX1 and RX2 with 16 mm baseline) and (RX1 and RX3 with 32 mm baseline)

Figure 5.38 shows plots of the phases of the complex interferograms after smoothing using a 4-by-4 independent resolution cell smoothing window identical to the one described for Figure 5.23. The effect of the step after 1.9 m in ground range becomes more obvious with the smoothing as can be observed by the darker colour in the images.

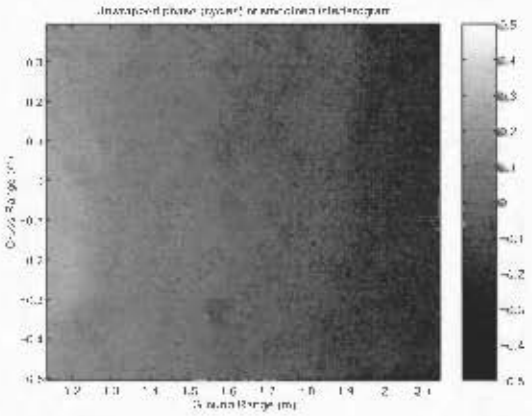

(a) Smoothed phase of interferogram from RX1 and RX2

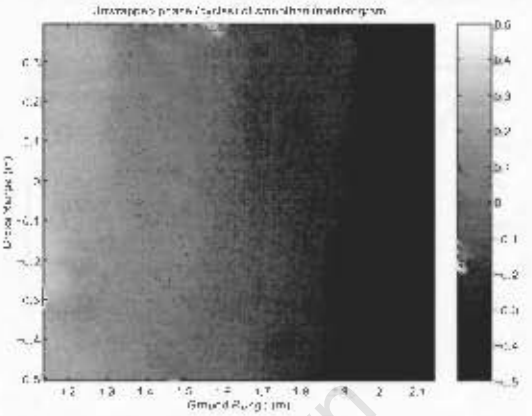

(b) Smoothed phase of interferogram from RX1 and RX3

Figure 5.38: Distributed scatterer stone scene with 72 step: Phases of smoothed complex interferograms (RX1 and RX2 with 16 mm baseline) and (RX1 and RX3 with 32 mm baseline)

Figures 5.39(a) and (b) shows coherence images of the scene with the 72 mm step. These images show that coherence remains above 0.8. This is acceptable for the measurement of the imaged scene as it was in the case of previous results in Figure 5.27.

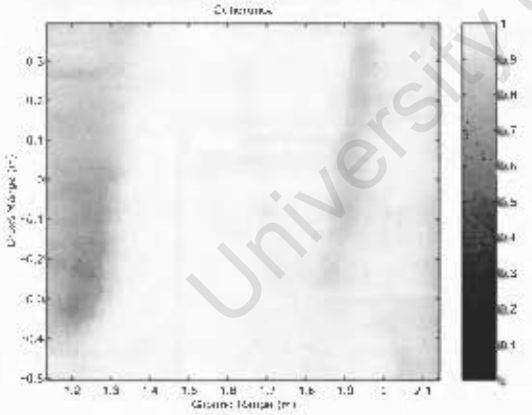

(a) Coherence image using RX1 and RX2 with 16 mm baseline

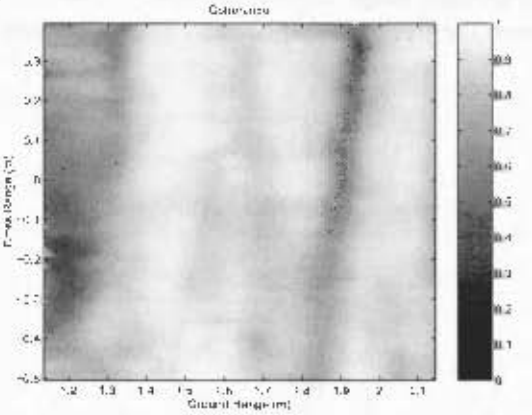

(b) Coherence image using RX1 and RX3 with 32 mm baseline

Figure 5.39: Coherence images for measurement using the distributed scatterer stone scene with 72 mm step: (RX1 and RX2 with baseline 16 mm) and (RX1 and RX3 with baseline 32 mm) respectively

Figures 5.40(a) and 5.40(b) show comparisons of smoothed interferometric phases obtained along the boresight for interferograms taken during two measurements: the first before the step was added, and the second after the step was added. This was done for interferograms formed using (RX1 and RX2 with 16 mm baseline in Figure 5.40(a)) and (RX1 and RX3 with 32 mm baseline in Figure 5.40(b)). The results are clear: the phase of the scene with the step deviates most substantially at the location of the step, namely from

1.8 m in ground range onwards. This section would naturally correspond to the section in which the 72 mm high step was introduced into the scene. The phase of the scene in this section can be seen at approximately 1.8 m as a dark low coherence band. The band varies in the range with slight variation in range versus cross-range because the step was positioned at a slight angle in cross range versus range.

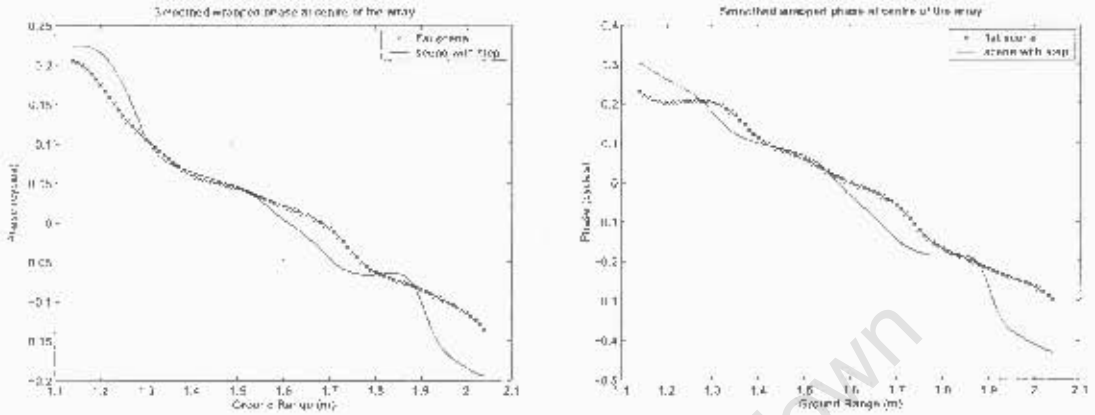

(a) RX1 and RX2 with 16 mm baseline (b) RX1 and RX3 with 32 mm baseline

Figure 5.40: Comparison of smoothed interferometric phases taken during two measurements

Figure 5.41 shows a comparison of flattened phases for smoothed interferometric phases obtained along boresight for interferograms taken during two measurements using (RX1 and RX2 with 16 mm baseline): the first before the step was added, and the second after the step was added. The region where the step is found can clearly be seen from the region of ground range extending from 1.9 m to 2.1 m since the phase clearly deviates largely from the flat scene's phase by approximately 0.06 cycles.

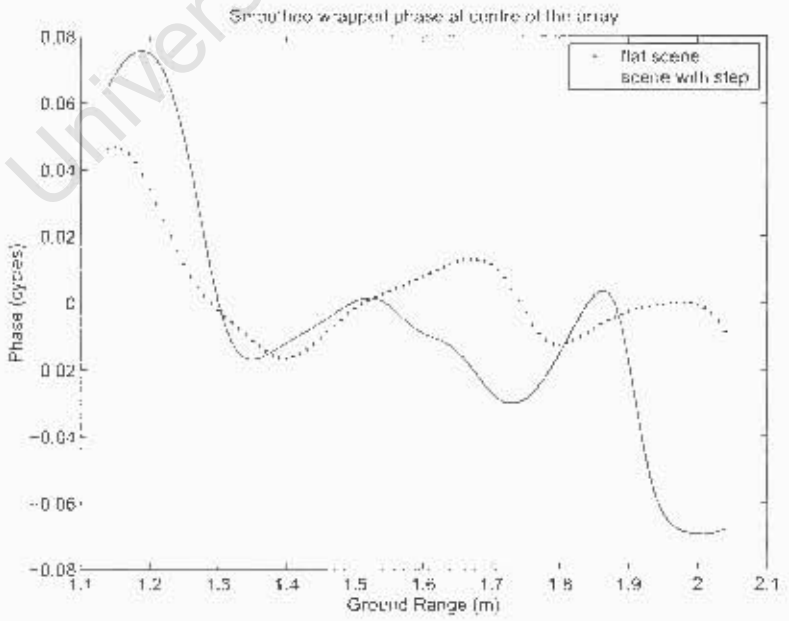

Figure 5.41: Comparison of flattened phases for smoothed interferometric phases obtained along boresight for interferograms taken during two measurements using (RX1 and RX2 with 16 mm baseline): the first before the step was added, and the second after the step was added

In order to verify the phase obtained along boresight as a result of introducing the 72 mm step to the scene, approximations of the expected phases of two points P1 (on the flat part of the stone scene) and P2 (on the edge of the 72 mm step) were calculated. This was done by calculating the expected phase between RX1 and RX2 (with 16 mm baseline) as seen in the side view geometry depiction of the 72 mm step scene shown in Figure 5.42 for the cases of P1 and P2. Using Equation 2.20 for single-pass, the expected phases for P1 and P2 as seen by transducers RX1 and RX2 were calculated as:

Expected phase for P1$=\frac{-2\pi(r_1 - r_2)}{\lambda} =$ 1.84 radians

Expected phase for P2$=\frac{-2\pi(r_3 - r_4)}{\lambda} =$ -2.22 radians

Therefore, the expected phase difference was -1.84-(-2.22)=0.38 radians. This difference of 0.38 radians represents 0.06 cycles that the phase of the flat scene is expected to drop by with the introduction of the step. This implies that the approximately 0.06 cycles phase drop that is found in the region from 1.9 m to 2.1 m as was seen in Figure 5.41 was to be expected.

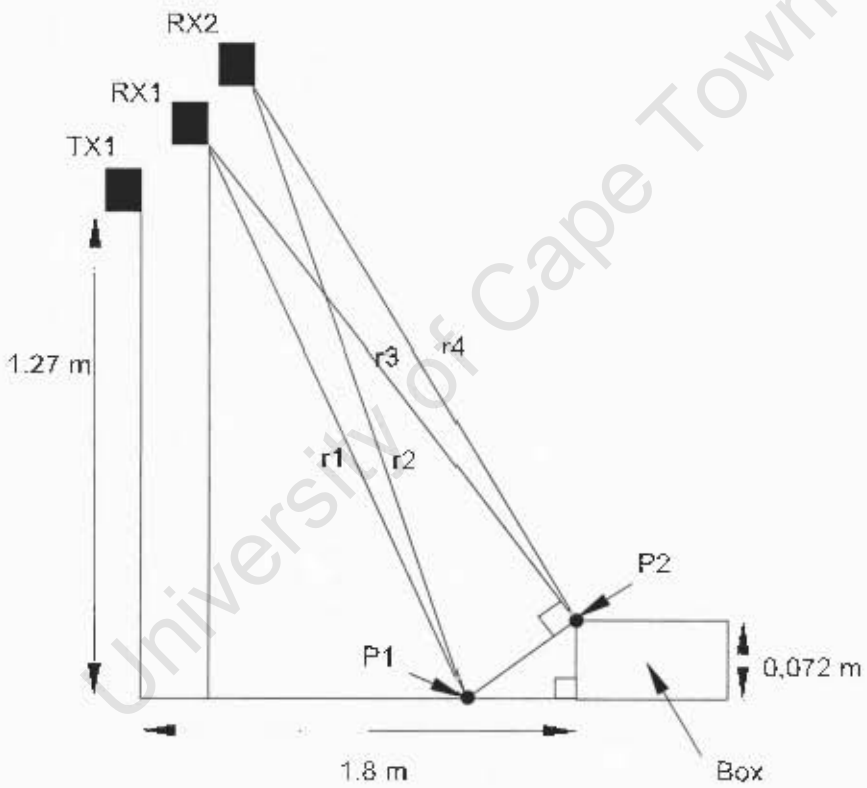

Figure 5.42: Side view geometry used for calculation of expected phase difference between P1 and P2 as seen by RX1 and RX2

5.3 Analysis of Results

The first matter that is obvious in the synthetic aperture measurements is the matter of the phase from interferograms differing from the simulated phase values as is seen in Figure 5.25. It seems that the difference in phase is a problem that persists, since the dif-

ference between simulated and measured interferometric phase remained approximately constant after taking a second reading of the flat distributed scatterer stone scene.

The shift in the area where the step was introduced is clearly seen in the interferograms that are produced. Clearly the sonar interferometry is sensitive to changes in height in the scene.

Chapter 6

Conclusions and Future Work

The investigation into the possibility of emulating SAR interferometry using a laboratory-scale sonar transducer system revealed that emulation was indeed feasible.

Focussed sonar interferograms were produced and satisfactory resolutions were obtained using this system.

Inverse filtering was shown to produce a signal that displayed small variation over the main lobe of the Hanning windowed range-compressed signal. The characteristic of phase varying by less than 1/8 of a cycle is desirable for registration of images in sonar interferometry in the laboratory-scale environment.

Increasing the baseline between imaging transducers produced a decrease in coherence as was predicted.

The process of chirp signal production was also described at various stages of the imaging processes. The ease with which the sonar system allows for parameters such as chirp reshaping and delaying that result in phase difference measurements to be recorded demonstrates its usefulness as a teaching tool.

The built sonar measurement system is multi-functional since transducers can be placed in many different positions. The only limitations are the physical lengths of the cables connected to the transducers and the number of transducers that can be used for input to the 16 channel simultaneous sampling card.

Future work could include applying reconstruction algorithms to interferograms and investigating similarities and differences between sonar and radar interferometry geometries. Further investigations into deviations of measurements from predicted phase values can be pursued.

Bibliography

[1] *The Speed of Sound*. http://hyperphysics.phy-astr.gsu.edu/hbase/sound/souspe.html.

[2] *PCI 703 Series Analogue Board User's Manual*, 2001.

[3] *EDR Enhanced API, Software Development Kit*, 2002.

[4] A.J. Wilkinson. *Techniques for 3-D Surface Reconstruction using Synthetic Aperture Radar Interferometry*. PhD Thesis, University of London, 1997.

[5] A.J. Wilkinson. *Notes on Radar Signal Processing: Fundamentals (Version 0.61 - 3 June 2002)*. 2002.

[6] A.J. Wilkinson. *SAR - Summary*. Undated.

[7] A.J. Wilkinson,P.K. Mukhopadhyay, Neil Lewitton and M.R. Inggs. *Inverse Synthetic Aperture Imaging using a 40 kHz Ultrasonic Laboratory Sonar*. Proceedings of the 15th Annual Symposium of the PRASA, Cape Town, SA, 2004.

[8] A. Ashok. Implementation and analysis of a bayesian approach to topographic reconstruction with multiple antenna synthetic aperture radar interferometry. Master's thesis, University of Cape Town, 2001.

[9] Brennan, T. *Beamforming Direction Finding of Acoustic Signals using 5-element circular array*. Undergraduate Thesis, University of Cape Town, 2003.

[10] C. Oliver and S. Quegan. *Understanding Synthetic Aperture Radar Images*. Artech House, Inc Norwood, MA, 1998.

[11] C. Prati and F. Rocca. *Range resolution enhancement with multiple SAR surveys combination*. Geoscience and Remote Sensing Symposium, IGARSS '92, Vol. 2, 1576-1578, 1992.

[12] A. Cracknell and L. Hayes. *Introduction to Remote Sensing*. Taylor & Francis Ltd, New York, 1993.

[13] J. C. Curlander and R. N. McDonough. *Synthetic Aperture Radar Systems and Signal Processing*. John Wiley and Sons, New York, Chichester, Brisbane, Toronto, Singapore, 1991.

[14] E. Rodriguez and J.M. Martin. *Theory and design of interferometric synthetic aperture radars*. IEE PROCEEDINGS-F, Vol. 139, No 2, APRIL 1992.

[15] H.A. Zebker and J. Villasenor. *Decorrelation in interferometric radar echoes*. IEEE Transactions on Geoscience and Remote Sensing, 30, 950-959, 1992.

[16] P. Horowitz and W. Hill. *The Art of Electronics*. Cambridge University Press, second edition (low price edition) edition, 1995.

[17] K. Chang. *RF and Microwave Wireless Systems*. John Wiley & Sons, Inc., 2000.

[18] N. Lewitton. *Inverse Synthetic Aperture Imaging*. Undergraduate Thesis. University of Cape Town, 2003.

[19] L.S.Wray. Synthetic aperture radar image simulator for interferometry. Master's thesis, University of Cape Town, 2000.

[20] M. Trninic. *Design and Construction of an Ultrasonic Radar Emulator*. Undergraduate Thesis, University of Cape Town, 2002.

[21] P. Menting. *The Programmed Software*. Project report, University of Cape Town, 2003.

[22] J. B. R. Touzi, A. Lopez and P. Vachon. *Coherence Estimation for SAR Imagery*. IEEE Transactions on Geoscience and Remote Sensing, Vol. 37, No. 1, 1999.

[23] R.O. Nielsen. *Sonar signal processing*. Artech House, Inc. Norwood, MA, 1991.

[24] S. Korda. *Design and Construction of an Ultrasonic Radar Emulator*. Undergraduate Thesis, University of Cape Town, 2002.